2009-07-13

A Method for Making In Situ Emittance Measurements of Coal Ash Deposits

Travis J. Moore
Brigham Young University - Provo

A METHOD FOR MAKING IN SITU EMITTANCE MEASUREMENTS OF COAL ASH DEPOSITS

by

Travis J. Moore

A thesis submitted to the faculty of

Brigham Young University

in partial fulfillment of the requirements for the degree of

Master of Science

Department of Mechanical Engineering

Brigham Young University

August 2009

BRIGHAM YOUNG UNIVERSITY

GRADUATE COMMITTEE APPROVAL

of a thesis submitted by

Travis J. Moore

This thesis has been read by each member of the following graduate committee and by majority vote has been found to be satisfactory.

Date	Matthew R. Jones, Chair
Date	Dale R. Tree
Date	R. Daniel Maynes

BRIGHAM YOUNG UNIVERSITY

As chair of the candidate's graduate committee, I have read the thesis of Travis J. Moore in its final form and have found that (1) its format, citations, and bibliographical style are consistent and acceptable and fulfill university and department style requirements; (2) its illustrative materials including figures, tables, and charts are in place; and (3) the final manuscript is satisfactory to the graduate committee and is ready for submission to the university library.

Date

Matthew R. Jones
Chair, Graduate Committee

Accepted for the Department

Larry L. Howell
Graduate Coordinator

Accepted for the College

Alan R. Parkinson
Dean, Ira A. Fulton College of Engineering and Technology

ABSTRACT

A METHOD FOR MAKING IN SITU EMITTANCE MEASUREMENTS OF COAL ASH DEPOSITS

Travis J. Moore

Department of Mechanical Engineering

Master of Science

A major problem associated with any power generation process in which coal is burned is the formation of ash and slag from the inorganic constituents of the coal. Ash deposition on heat transfer surfaces in coal-fired reactors is unavoidable and can have a significant effect on the performance and maintenance of boilers and gasifiers. A greater understanding of the thermal properties of coal ash deposits is important in reducing their negative impact. This work presents the development of an experimental method for making *in situ* measurements of the spectral emittance of coal ash deposits. It also provides measured emittances for two coals under oxidizing and reducing conditions.

The experimental procedure consisted of burning coal in a down-fired entrained-flow reactor and collecting ash deposits on a circular probe under controlled conditions.

Spectra collected from a Fourier transform infrared (FTIR) spectrometer were combined with an instrument response function to measure the spectral emissive power from the surface of the ash deposit. The spectral emissive power was used to infer the deposit surface temperature. These two measurements were used to calculate the spectral emittance of the deposit. This experimental method was validated by measuring the known temperature and spectral emittance of a blackbody radiator.

The experimental method was used to find the spectral emittance of bituminous and subbituminous coals under both oxidizing and reducing conditions. The bituminous coal analyzed was Illinois #6 coal from the Crown III mine and the subbituminous coal analyzed was Wyoming coal from the Corederro mine. The spectral emittance of the subbituminous coal was lower than that of the bituminous coal under both oxidizing and reducing conditions. The emittances of both coals under reducing conditions were greater than those found under oxidizing conditions. A total band emittance was defined and calculated for each coal. The total band emittance as well as theoretical upper and lower total emittance limits were calculated as functions of temperature. There was little temperature dependence in the total emittance estimates.

ACKNOWLEDGMENTS

The author wishes to thank GE Global Research for their generous funding of this research. This work would not have been possible without the important guidance and contributions from Professors Matthew Jones, Dale Tree, Daniel Maynes, and Larry Baxter. Their instruction is greatly appreciated. The author would also like to thank the following people for their contributions: Darron Cundick, Ryan Blanchard, Todd Reeder, Adam McMurtrey, and Tim Shurtz.

TABLE OF CONTENTS

LIST OF TABLES

LIST OF FIGURES

NOMENCLATURE

Symbols

A	surface area
a	wavenumber dependent term in the instrument response function
b	surroundings dependent term in the instrument response function
c_p	specific heat of the pyroelectric material
C	optical path constant
C_2	second radiation constant
$\dot{E}$	energy rate
E	emissive power
F	fraction of total emission from blackbody
f	mirror focal length
G	irradiation
g	geometry dependent constant
I	intensity
J	radiosity
k	thermal conductivity
M	FTIR spectrometer signal
m_d	mass of the detector
t	time
T	temperature
U	overall heat transfer coefficient

Greek Symbols

α	absorptance
α_1	first radiation constant
α_2	second radiation constant
Δ	error
ε	emittance
γ	proportionality constant
λ	wavelength
$\bar{\nu}$	wavenumber
ρ	reflectance
σ	Stefan-Boltzmann constant
ω	solid-angle

Subscripts

AVG	average
B	band emittance
b	blackbody
d	detector
e	emitted
i	irradiated subsurface of detector
P	painted probe
r	reflected
S	source
st	stored
sur	surroundings
λ	spectrally dependent
$\bar{v}$	spectrally dependent

1 Introduction

A major problem associated with any power generation process in which coal is burned is the formation of ash and slag from the inorganic constituents of the coal. Ash deposition on heat transfer surfaces in coal-fired reactors is unavoidable. These deposits can have a significant effect on the performance and maintenance of the boiler. Boiler manufacturers and operators need to be able to predict the thickness and morphology of the ash deposits based on the type of coal used and the reactor operating conditions. Thermal transport properties are key inputs for determining both deposit morphology and boiler performance. This work presents an experimental method designed to make *in situ* measurements of the spectral emittance of coal ash deposits. Results are presented for bituminous and subbituminous coals under both oxidizing and reducing conditions.

1.1 Background

Coal is an important source of energy because of its potential for power generation and its abundance in the earth. With estimated coal reserves sufficient to last for the next 250 years, the United States has more high quality coal than any other country in the world [1]. Presently, coal is used to power 57% of U.S. electrical generation [2] and it is projected that by the year 2030, coal will be used to produce 48% of the world's electric power [3]. In traditional coal-fired boilers, pulverized coal is

burned in an overall oxidizing environment, although there are regions of the boilers that are locally under reducing conditions. The heat from the flame is transferred through tubes that line the combustion space, producing steam for the generation of electricity [4].

Despite its abundance and power generation potential, coal is a controversial fuel source because of the pollution caused by conventional coal-burning power plants. Among the gases emitted by these plants is carbon dioxide. Many believe carbon dioxide to be a primary cause of global warming. On April 17, 2009, the Environmental Protection Agency officially announced that carbon dioxide, among other greenhouse gases, contributes to air pollution and may endanger public health or welfare [5]. This classification of carbon dioxide as a pollutant will allow the EPA to impose regulations on carbon dioxide emissions. In addition to carbon dioxide, other pollutants emitted by coal burning power plants include sulfur dioxide, which causes acid rain; NO_x; and mercury, which contaminates rivers and lakes [3]. Because of the pollution caused by traditional coal-burning power plants, alternative coal power generation technologies are being investigated.

Among the most promising of the alternative power generation processes is coal gasification. In contrast to conventional coal combustion processes wherein the chemical energy of the coal is converted to heat, coal gasification is a process by which the chemical energy in the coal is converted to chemical energy in gases such as carbon monoxide, hydrogen, and hydrocarbons [6]. This synthetic gas, or syngas, can be processed to remove impurities before it is burned. Some argue that clean-up process is more efficient and has a lower cost than post combustion clean-up processes used in traditional coal burning power plants [1]. As opposed to conventional coal-fired power

plants which operate under oxidizing conditions, coal gasification occurs in a fuel-rich (reducing) environment. The gasification process can be integrated with a combined cycle resulting in the integrated gasification combined cycle (IGCC). In this process, the syngas is burned in a gas turbine (Brayton Cycle). The exhaust gases of the turbine enter a boiler, creating superheated steam which is then used to drive a steam turbine (Rankine Cycle) [7]. The thermal efficiency of the IGCC can theoretically be significantly higher than that of traditional coal power plants [8]. Studies have shown that pollutants (such as SO_2, CO, and NO_x) and particulate emissions from an IGCC plant are less than one tenth of the levels permitted by the New Source Performance Standards [9]. Additionally, IGCC plants use 30 to 50 percent less water to produce electric power than other coal-based power generation technologies [10].

1.2 Coal Ash Deposits

When coal is burned in a traditional boiler the majority of the inorganic material contained in the coal remains in the solid phase. Coal ash consists of material that remains in the condensed phase after complete combustion. Ash deposits inevitably form on the heat transfer surfaces of boilers and on the walls of coal gasifiers. These ash deposits can affect the thermal transport in the boiler or gasifier and, therefore, the overall performance of the plant. Knowledge of the thermal transport properties of the ash deposits is important in determining the effects of the deposits on the performance of boilers and gasifiers and in plant design and operation.

1.3 Motivation

Ash deposits can adversely affect the thermal transport through heat transfer surfaces [11]. Accordingly, the effects of ash deposits can have a significant impact on the operation and design of boilers and gasifiers [12-14]. The effects of ash deposits on thermal transport are directly related to the properties of the deposits. Experimental measurements can provide an understanding of the radiative properties of ash deposits and, in turn, provide important information about reactor design and operation. Because the deposit properties are sensitive to the environment in which they are formed [13, 15, 16], *in situ* emittance measurements under both oxidizing and reducing conditions are important for the optimization of boilers and gasifiers.

1.4 Research Objectives and Contributions

The objectives of this work include: 1) the development of an experimental procedure to make *in situ* emittance measurements of coal ash deposits and 2) obtaining *in situ* measurements of ash deposits of different coals under both oxidizing and reducing conditions. The experimental procedure includes a method for simulating the accumulation of ash deposits under oxidizing and reducing conditions as well as a method for measuring the emittance of these deposits. *In situ* emittance data is acquired for a bituminous coal and a subbituminous coal under oxidizing and reducing conditions.

1.5 Delimitations

The ash deposits analyzed were formed from firing pulverized coal only. Only two coals were used as fuel sources: a bituminous coal and a subbituminous coal. The ash deposits analyzed were only rigid, particulate layers. No slag layers were examined. The effects of the physical morphology of the ash deposit on the deposit emittance were not investigated. The ash deposits were collected exclusively on a cylindrical probe.

1.6 Overview

This thesis presents the experimental procedures used to measure the emittance of coal ash deposits as well as the results of these experiments. Relevant prior work and research in making emittance measurements of ash deposits are reviewed in Chapter 2. Chapter 3 discusses the experimental equipment and procedures used to collect ash deposits. Analytical methods used to calculate the emittance of ash deposits are developed in Chapter 4. Chapter 5 presents the results of experiments conducted with a blackbody radiator used to verify the techniques developed in Chapter 4. Chapter 6 discusses the experimental procedures used to measure the emittance of ash deposits. Chapter 7 presents the emittance measurements for two different types of coals under both oxidizing and reducing conditions. Finally, Chapter 8 discusses results, summarizes the work, and presents conclusions.

2 Prior Work

A review of applicable literature reveals the difficulty in making total, hemispherical emittance and spectral emittance measurements of any material. Most methods used to measure spectral emittance involve placing a sample of the material under carefully controlled conditions, emphasizing the need for the development of a method of making *in situ* spectral emittance measurements. This literature review focuses on different methods for measuring emittance and on their application to making *in situ* measurements of the spectral emittance of ash deposits.

2.1 Spectral Emittance Measurements

The emittance of an object is highly dependent on the condition of the object surface, which can change from day to day [17]. Precise knowledge of the surface temperature of the object must be known [18]. Other considerations include accounting for the reflections from the surroundings [19]. There are a number of methods used to measure the total, hemispherical emittance of an object. Surface emittance of an object can be measured by heating the bottom surface and exposing the top surface to quiescent air [20]. Heat-flux based methods can be used to measure the surface emittance of variable emissivity surfaces [21]. Measuring the total hemispherical emittance is much easier than measuring the spectral, hemispherical emittance. There are two main

methods used to measure the spectral emittance of an object [18]: 1. measuring the radiation emitted from a surface at a known temperature and 2. measuring the radiation reflected from and transmitted through the object. Many methods used to measure the spectral emittance of an object require the use of a blackbody source as a reference. Markham et al. developed a bench top Fourier transform infrared based instrument for measuring both surface temperature and spectral emittance that combines both techniques mentioned above. This method eliminates extraneous reflected radiation and uses the measured directional-hemispherical reflectance and directional-hemispherical transmittance to find the spectral emittance and the surface temperature [18]. Woskov et al. developed a radiometric method for finding emittance and surface temperature in which the thermal radiation from the source was split by a beamsplitter between a radiometer and a mirror [22]. The ratio of the signal with and without the returned reflection provided an emittance measurement.

Other techniques for measuring the spectral emittance of an object do not require a blackbody. These techniques often require making measurements at multiple colors (wavelengths) and ratioing the signals, allowing for the determination of the surface temperature by cancelling out the emittance [23]. This method assumes the emittance to be the same at both wavelengths and is often unreliable because it requires short wavelengths [22]. Watson measured the spectral emittance of rocks and dry soils by taking the ratio of signals from the same source at two different temperatures at two different times [24]. This method assumes that the source is temporally invariant. Svet has proposed using two temperature measurements and coupling those measurements with directional reflectance measurements to find the spectral emittance [25].

The different techniques used to make spectral emittance measurements are primarily limited to very specific applications and, therefore, cannot be used to find the spectral emittance of an arbitrary surface under varying conditions. Accordingly, there is a need to develop a method of measuring the spectral emittance of coal ash deposits that form in different environments.

2.2 Spectral Emittance of Coal Ash Deposits

The emittance of coal ash deposits is highly dependent on the deposit composition, morphology, and on the conditions under which the deposit is formed. Spectral emittance measurements for various deposits under a variety of conditions are highly desirable. The difficulty in measuring the spectral emittance of an object is made even more difficult if *in situ* measurements are required. Most of the methods discussed above require that a sample material be placed in a controlled environment. Thermal properties of ash deposits have been measured in laboratories [26]. However, making *in situ* measurements is advantageous because the properties of the deposit may change when removed from the environment in which they are formed. Additionally, by making *in situ* measurements the history of the deposit growth can be observed.

Shaw and Smouse developed an instrument used to make *in situ* measurements of ash deposit spectral emittance and temperature [19]. The instrument accounted for the reflection from the surroundings as well as the emission from any particles surrounding the deposit. This instrument was limited to making measurements at only a few fixed wavelengths and relied on curve-fitting for the rest of the spectrum. More recently, Baxter et al. [27] developed a method of making *in situ* measurements of thermal

properties of ash deposits using Fourier transform infrared (FTIR) emission spectroscopy. This technique was used to measure the spectral emittance of ash deposits for various fuels under oxidizing conditions. This experimental method is used as a foundation for the methods presented in this work.

3 Deposition Experiment

In order to make *in situ* measurements on ash deposits, an experimental method was developed in which ash deposits form under conditions similar to conditions inside a boiler or a gasifier. The setup allows for optical access to the ash deposit for measurement purposes. The measurements can be made *in situ* during the ash deposition process without disturbing the ash deposit.

3.1 Experimental Setup

An experimental setup was designed by Baxter et al [27] for the purpose of analyzing coal ash deposits. A similar setup was used to perform the experiments described in this work. The equipment and procedures used in these experiments are briefly described below. Detailed information about the construction, setup, and operation of the experimental equipment are provided by Cundick [28].

3.1.1 Multi-Fuel Reactor

A multi-fuel reactor (MFR) was constructed at the facilities at Brigham Young University. The MFR is a down-fired entrained-flow reactor. As the name suggests, it was designed to be able to burn a number of different fuels. The MFR consists of seven identical vertically stacked sections. Figure 3-1 shows the inside of a single section.

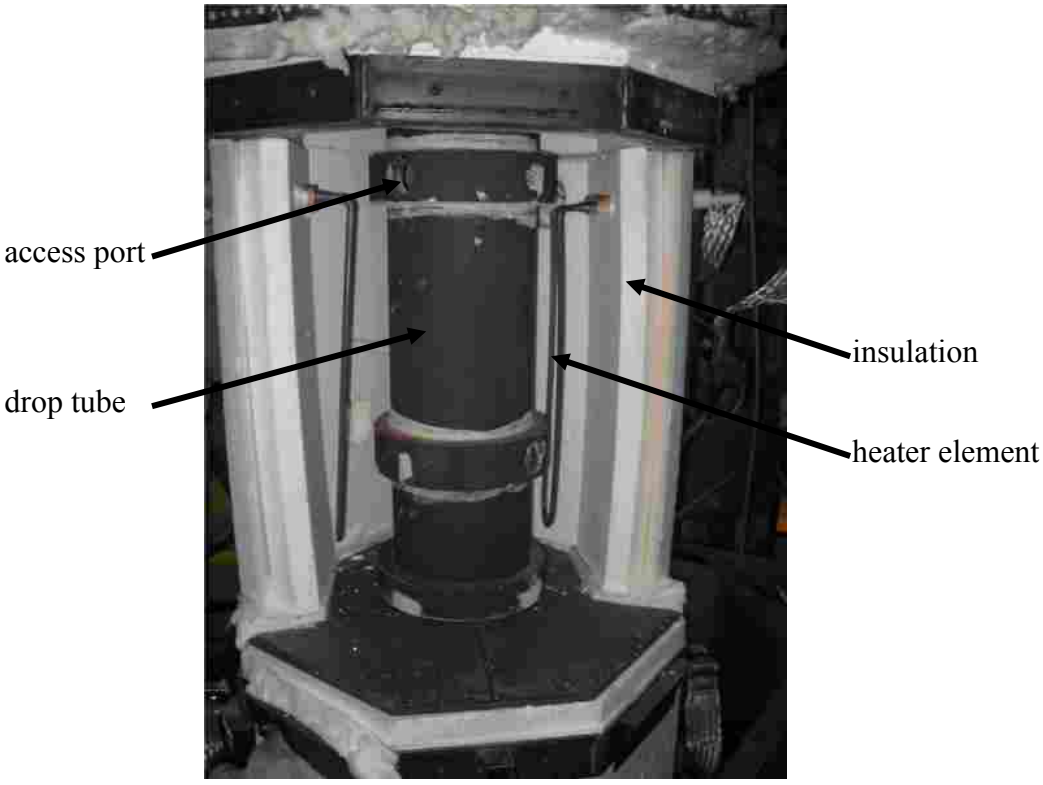

Figure 3-1. View of the inside of a single section of the multi-fuel reactor.

At the center of each section is the six-inch inner diameter silicon carbide ceramic drop tube. Each tube section is twenty-four inches long and contains four access ports into the reactor that can be used for analysis or to feed fuel. In the space between the reactor tube and the stiff insulation that surrounds the tube are four equally spaced electrical heating elements used to control the drop-tube temperature. The total height of the drop-tube furnace is fourteen feet. The top section is connected to a preheat burner system and the bottom is open to the atmosphere. Twelve inches below the reactor outlet is the intake of an exhaust fan. A schematic of the reactor is shown in Figure 3-2.

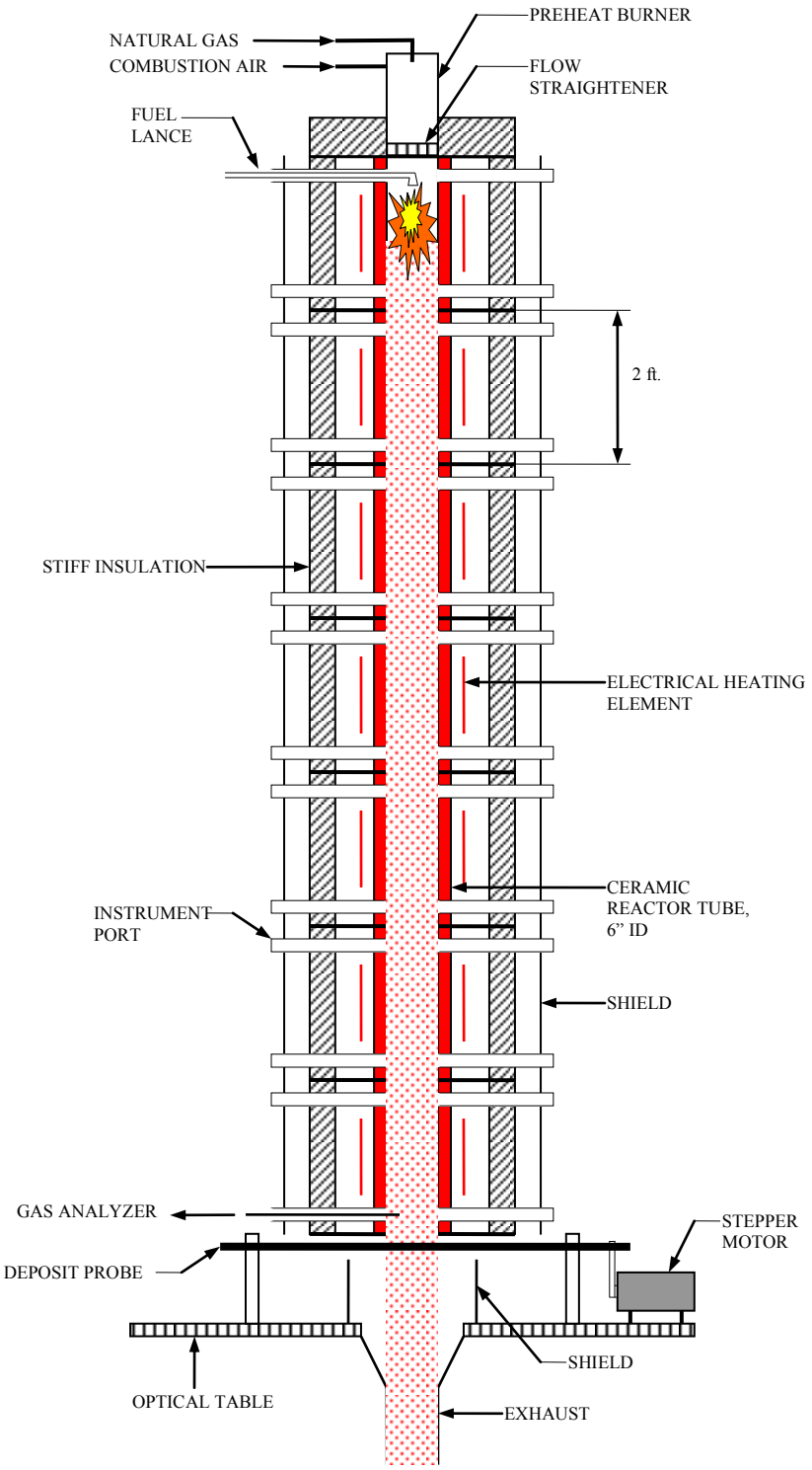

Figure 3-2. Schematic of the multi-fuel reactor used in the deposition experiments.

3.1.2 Preheat Burner

A preheat burner system is attached to the top section of the reactor. This system consists of a line of natural gas that is premixed with air. There is also a source of secondary air and a flow straightener. The preheat burner is pictured in Figure 3-3.

Figure 3-3. View of the top of the reactor, which includes the preheat burner system.

3.1.3 Fuel Feed System

A fuel feed system was used to control the rate at which pulverized coal was injected into the MFR. The pulverized coal is placed in a pressure controlled hopper. A motor-driven auger feeds the coal from the hopper at a specified mass flow rate into a stream of compressed air. The pulverized coal entrained by the air stream is carried through a lance inserted into one of the access ports in the reactor and injected downward into the reactor. The fuel feed system is pictured in Figure 3-4.

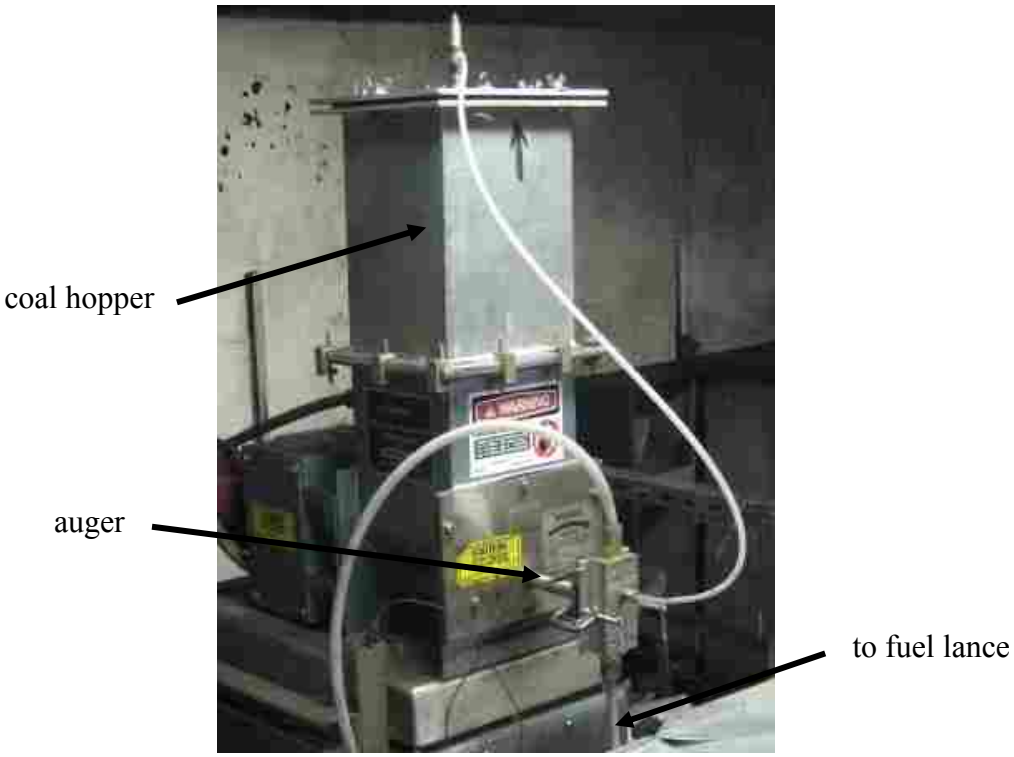

Figure 3-4. View of fuel feed system.

3.1.4 Deposition Probe

A circular steel ash collection probe is placed at the outlet of the reactor. Ash from the reactor collects on this probe and the deposits formed on the probe can be analyzed. The probe is a smooth, drawn tube of high carbon steel with an outer diameter of 0.75 inches. The probe is rotated using a stepper motor to ensure even accumulation of ash deposit over the entire probe surface. The probe is instrumented with high temperature thermocouples on the outer surface. Compressed air is blown through the probe to keep the probe surface temperature at nominally 400º C. The deposition probe is pictured in Figure 3-5.

Figure 3-5. View of the fully-assembled deposition probe.

3.2 Experimental Procedure

The experimental method developed to collect ash deposits on the deposition probe included heating the reactor, burning the pulverized coal under the desired conditions, and cooling the reactor. Cundick [28] provides a detailed description of the warm-up and cool-down procedures. Each section of the reactor is heated to 1100 °C. Air is supplied to the fuel lance and the preheat burner. The feed system is turned on and the injected coal burns out in the reactor. Typical fuel feed rates were between 1.5 and 3.5 pounds per hour. The experiments discussed in this work were performed simultaneously with research done by Cundick [28] to measure the thermal conductivity of ash deposits. The deposition probe is placed about one inch below the reactor outlet. A cylindrical aluminum sheet is placed between the exhaust intake and the deposition probe in order to prevent the exhaust gases from leaking into the lab. The deposition probe is rotated about its axis at 0.25 rpm. Cooling air is blown through the probe throughout the experiment to

maintain the probe surface nominally at a constant temperature of 400º C. The coal is typically burned for five or six hours in order for a sufficiently large deposit to accumulate. Figure 3-6 shows an example of a typical ash deposit on the probe after running the experiment.

Figure 3-6. Typical ash deposit on the probe after a deposition experiment.

3.3 Summary

In order to emulate the deposition of coal ash on heat transfer surfaces in boilers and gasifiers, an experimental method in which pulverized coal is burned in a laboratory scale entrained-flow, multi-fuel reactor was developed. The coal is burned out in the reactor and the ash accumulates on a circular probe located at the reactor outlet. The properties of these ash deposits can then be measured.

4 Measuring Emittance

This chapter discusses the development of a technique used to measure the hemispherical, spectral emittance of an object. The application of this technique to make *in situ* measurements of the ash deposits collected in the deposition experiment described in Chapter 3 will be discussed in Chapter 6.

4.1 Calculation of the Spectral, Hemispherical Emittance

The spectral, hemispherical emittance of an object is defined as the ratio of the spectral, hemispherical emissive power of the object to the blackbody spectral emissive power at the object temperature, as shown in Eq. (4-1) [20]. The spectral, hemispherical emissive power of an object is the rate at which radiation of wavenumber $\bar{\nu}$ is emitted in all directions from a surface per unit wavenumber about $\bar{\nu}$ and per unit surface area [20].

$$\varepsilon_{\bar{\nu}}(T) = \frac{E_{\bar{\nu}}(T)}{E_{b,\bar{\nu}}(T)} \qquad \textbf{(4-1)}$$

The blackbody spectral emissive power can be calculated for any temperature and wavenumber using the Planck function [17], shown in Eq. (4-2). This represents the energy rate per unit wavenumber, not at a given wavenumber as is commonly thought.

$$E_{b,\bar{\nu}}(T) = \frac{\pi \alpha_1 \bar{\nu}^3}{\exp(\alpha_2 \bar{\nu} / T) - 1} \qquad \textbf{(4-2)}$$

By combining Eqs. (4-1) and (4-2), the spectral, hemispherical emittance of an object can be expressed as

$$\varepsilon_{\bar{\nu}}(T_S) = \frac{E_{\bar{\nu}}(T_S)(\exp(\alpha_2 \bar{\nu} / T_S) - 1)}{\pi \alpha_1 \bar{\nu}^3} \qquad \textbf{(4-3)}$$

Eq. (4-3) shows that the spectral emittance can be calculated if the spectral emissive power and the surface temperature of the object can be measured.

4.2 Measurement of the Spectral, Emissive Power of an Ash Deposit

The following simple analysis demonstrates the measurement system that is used to find the spectral emissive power required in Eq. (4-3). As illustrated in Figure 4-1, radiation is emitted and reflected from an ash deposit. Irradiation $G_{\bar{\nu}}$ enters an optical train where it is spectrally altered by some constant $C_{\bar{\nu}}$ after which it irradiates a detector. The detector outputs a signal $M_{\bar{\nu}}$. The objective is to find some relationship between this output signal and the spectral emissive power of the ash deposit according to the following equation.

$$E_{\bar{\nu}}(T_S) = f(M_{\bar{\nu}}) \qquad \textbf{(4-4)}$$

This relationship will be known as the instrument response function (IRF). The instrument response function can be found by developing (1) a relationship between $E_{\bar{\nu}}(T_S)$ and $G_{\bar{\nu}}$ and (2) a relationship between $C_{\bar{\nu}} G_{\bar{\nu}}$ and $M_{\bar{\nu}}$.

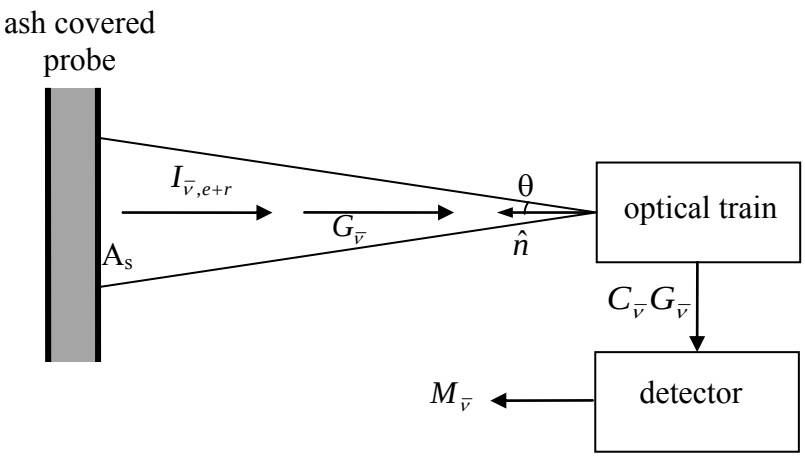

Figure 4-1. Schematic of detector and radiation source.

If the entrance to the optical system is modeled as a point, the spectral irradiation that enters the optical path can be defined as

$$G_{\bar{\nu}} = \int_{2\pi} I_{\bar{\nu},i} \cos\theta \, d\omega \tag{4-5}$$

where $I_{\bar{\nu},i}$ is the incident spectral intensity. This intensity can be modeled as follows

$$I_{\bar{\nu},i} = \begin{cases} 0 \;\; if \;\; \omega \neq \Delta\omega_{o\to s} << 1 \\ I_{\bar{\nu},e+r} \;\; if \;\; \omega = \Delta\omega_{o\to s} \end{cases} \tag{4-6}$$

This assumption means that all sources of radiation except the ash-covered probe are neglected. The emission, absorption, and scattering by the intervening gases are neglected. Accordingly, if the solid angle defined by the acceptance cone of the optical system $\Delta\omega_{o\to s}$ is much less than 1, then the integral in Eq. (4-5) can be approximated as the product

$$G_{\bar{\nu}} \approx I_{\bar{\nu},e+r} \cos\theta \Delta\omega_{o\to s} \tag{4-7}$$

If the angle θ is small, then Eq. (4-7) reduces to

$$G_{\bar{\nu}} \approx (I_{\bar{\nu},e} + I_{\bar{\nu},r})\Delta\omega_{o\to s} \quad \textbf{(4-8)}$$

The reflected intensity from the ash is neglected. The validity of this assumption is further investigated in section 6.2.1. If the source is a diffuse emitter, the directional emittance is constant and independent of direction. All sources described in this document are assumed to be diffuse and, therefore, the spectral, directional emittance will be referred to simply as the spectral emittance. For dielectrics such as ash deposits, the directional emittance is approximately constant for θ < 70º, where θ is the angle measured in the clockwise direction from the surface normal. Therefore, the directional emittance at angles smaller than 70º is nominally the same as the normal emittance, corresponding to θ = 0º [20]. For a diffuse surface, the emitted intensity is

$$I_{\bar{\nu},e} = \frac{E_{\bar{\nu}}(T_S)}{\pi} \quad \textbf{(4-9)}$$

and the spectral irradiation reduces to

$$G_{\bar{\nu}} \approx \frac{E_{\bar{\nu}}(T_S)}{\pi}\Delta\omega_{o\to s} \quad \textbf{(4-10)}$$

The detector is now considered in greater detail. The detector used in all experiments described in this document is a DTGS pyroelectric detector. This detector consists of a thin piece of pyroelectric material (deuterated triglycine sulfate) placed between two electrodes. The electric polarization of the pyroelectric material changes as a function of temperature. When exposed to IR radiation, the temperature and polarization of the pyroelectric material change. The change is detected as a current in the circuit connecting

the electrodes. The signal voltage from the spectrometer, $M_{\bar{\nu}}$, is proportional to the change in the detector temperature, T_d, with time, according to Eq. (4-11).

$$\gamma_{\bar{\nu}} M_{\bar{\nu}} = \frac{dT_d}{dt} \tag{4-11}$$

In Eq. (4-11), $\gamma_{\bar{\nu}}$ is a spectral proportionality constant. An energy balance can be performed on the pyroelectric material. Figure 4-2 shows a simple schematic of the detector and the terms included in the energy balance.

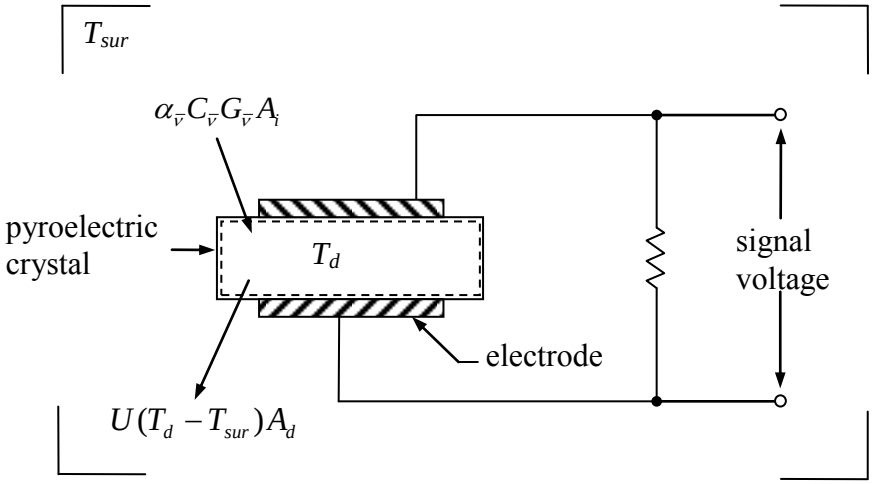

Figure 4-2. Energy balance on the DTGS detector

The energy balance yields the following equation.

$$\dot{E}_{in} - \dot{E}_{out} = \dot{E}_{st} \tag{4-12}$$

The rate of energy into the detector is

$$\dot{E}_{in} = \alpha_{\bar{\nu}} C_{\bar{\nu}} G_{\bar{\nu}} A_i \tag{4-13}$$

The energy rate out of the detector includes all radiative and convective losses and is represented as

$$\dot{E}_{out} = U(T_d - T_{sur})A_d \tag{4-14}$$

The energy storage term is

$$\dot{E}_{st} = m_d c_p \frac{dT_d}{dt} \tag{4-15}$$

Equations (4-13), (4-14) , and (4-15) are substituted into Eq. (4-12), yielding the following equation.

$$\alpha_{\bar{\nu}} C_{\bar{\nu}} G_{\bar{\nu}} A_i - U(T_d - T_{sur})A_d = m_d c_d \frac{dT_d}{dt} \tag{4-16}$$

Rearranging and substituting from Eq. (4-10) gives

$$\frac{dT_d}{dt} = \frac{\alpha_{\bar{\nu}} C_{\bar{\nu}} A_i}{m_d c_d}\left(\frac{E_{\bar{\nu}}(T_S)}{\pi}\Delta\omega_{o\to s}\right) - \frac{UA_d}{m_d c_d}(T_d - T_{sur}) \tag{4-17}$$

Substituting Eq. (4-11) and rearranging again we have

$$M_{\bar{\nu}} = \frac{1}{\gamma_{\bar{\nu}}}\frac{dT_d}{dt} = \frac{A_i \Delta\omega_{o\to s}}{\pi m_d c_d}\left[\frac{\alpha_{\bar{\nu}} C_{\bar{\nu}}}{\gamma_{\bar{\nu}}} E_{\bar{\nu}}(T_S) - \frac{UA_d \pi}{\gamma_{\bar{\nu}} A_i \Delta\omega_{o\to s}}(T_d - T_{sur})\right] \tag{4-18}$$

Rearranging Eq. (4-18) to get it in the form of Eq. (4-4) results in the following

$$E_{\bar{\nu}}(T_S) = \frac{\pi m_d c_d}{A_i \Delta\omega_{o\to s}}\left[\frac{\gamma_{\bar{\nu}}}{\alpha_{\bar{\nu}} C_{\bar{\nu}}} M_{\bar{\nu}} + \frac{UA_d}{\alpha_{\bar{\nu}} C_{\bar{\nu}} m_d c_d}(T_d - T_{sur})\right] \tag{4-19}$$

Eq. (4-19) can be simplified by letting

$$g = \frac{\pi\, m_d c_d}{A_i \Delta\omega_{o\to s}}$$

$$a(\bar{\nu}) = \frac{\gamma_{\bar{\nu}}}{\alpha_{\bar{\nu}} C_{\bar{\nu}}} \qquad \textbf{(4-20)}$$

$$b(\bar{\nu}, T_d, T_{sur}) = \frac{UA_d}{\alpha_{\bar{\nu}} C_{\bar{\nu}} m_d c_d}(T_d - T_{sur})$$

such that

$$E_{\bar{\nu}}(T_S) = g\left[a(\bar{\nu}) M_{\bar{\nu}} + b(\bar{\nu}, T_d, T_{sur})\right] \qquad \textbf{(4-21)}$$

The resulting equation provides the desired relationship between the spectral emissive power of the ash deposit and the signal output by the detector. This relationship is the instrument response function. The instrument which contains the detector and provides the output signal is called a Fourier-Transform Infrared (FTIR) spectrometer.

4.3 FTIR Spectrometer

A Fourier-Transform Infrared spectrometer is an instrument which collects the entire radiant energy (from all spectrometer wavenumbers) from a source [29]. A picture of all of the components inside an FTIR spectrometer is shown in Figure 4-3.

Figure 4-3. View of the internal components of an FTIR spectrometer.

Figure 4-3 also shows the path that the radiant energy follows inside the FTIR spectrometer. The energy from the radiation source enters the spectrometer through an external port and enters the interferometer. An interferometer consists of a beam splitter, a stationary mirror and a moving mirror as shown in Figure 4-4.

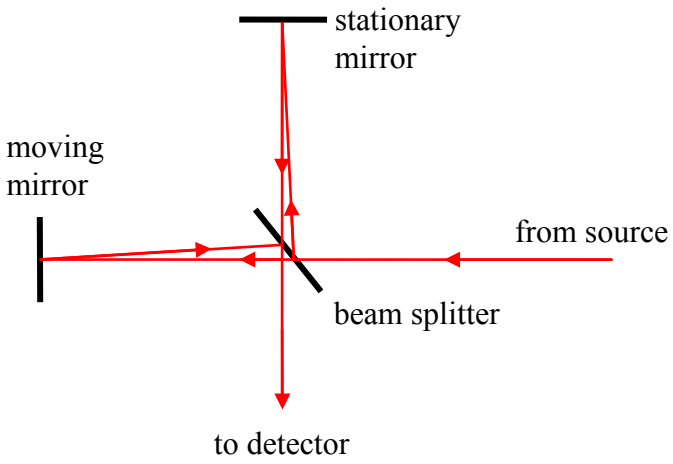

Figure 4-4. Schematic of the light path followed in an interferometer.

The incoming radiant energy is divided by the beam splitter. The intensity measured by the detector depends on the position of the moving mirror based on the constructive and destructive interference of the combined radiant energy returning from the mirrors [29]. The result is an interferogram, which represents the intensity of the recombined light as a function of the position of the moving mirror. The interferogram is the Fourier Transform of the light intensity as a function of wavenumber. The FTIR spectrometer performs the required inverse Fourier Transform calculations and provides a plot of the detector signal as a function of wavenumber.

4.4 Experimental Verification of the Instrument Response Function

An experimental procedure was performed in order to verify the instrument response function derived in section 4.2. The radiation from a blackbody radiator was directed into the external access port of the FTIR spectrometer. As shown in Figure 4-5, an off-axis parabolic mirror was used to collimate the radiation from the blackbody and direct it into the spectrometer.

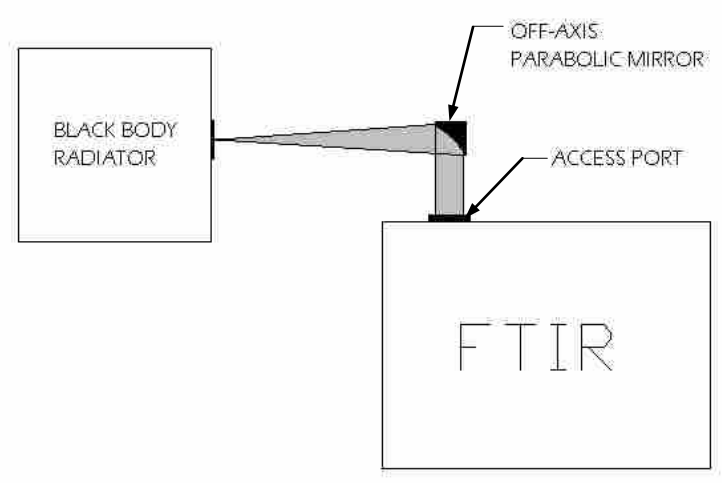

Figure 4-5. Schematic of the experimental setup used to verify the equation for the instrument response function.

A blackbody radiator was used because its temperature can be accurately controlled and its spectral emittance is known to equal unity. Spectra were collected using the spectrometer over a wide range of blackbody temperatures. An example of a high resolution (1/8 wavenumber) spectrum collected by the FTIR is shown in Figure 4-6. In order to average or smooth the influence of the gas absorption lines in the high resolution scans, low resolution spectra (32 wavenumbers) were also collected. The low resolution spectrum can also be seen in Figure 4-6 .

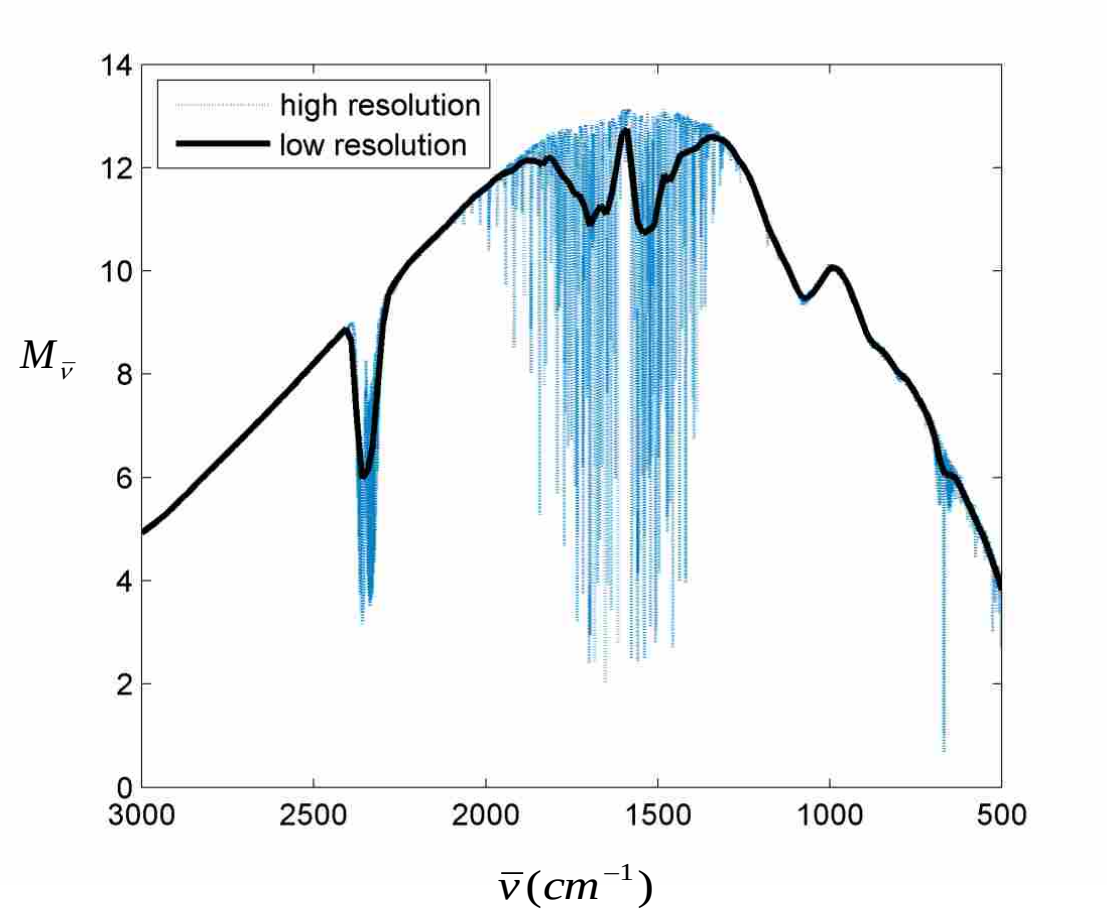

Figure 4-6. Comparison of high and low resolution spectra collected by the FTIR spectrometer.

For a given wavenumber, the FTIR signal can be plotted as a function of the spectral emissive power of the blackbody source, which can be calculated using the Planck function for the specified blackbody temperature. A line can be fit to the data. The response of the FTIR to the source can therefore be approximated as linear. Figure 4-7 shows the data and the corresponding lines for six different wavenumbers over a range of blackbody temperatures.

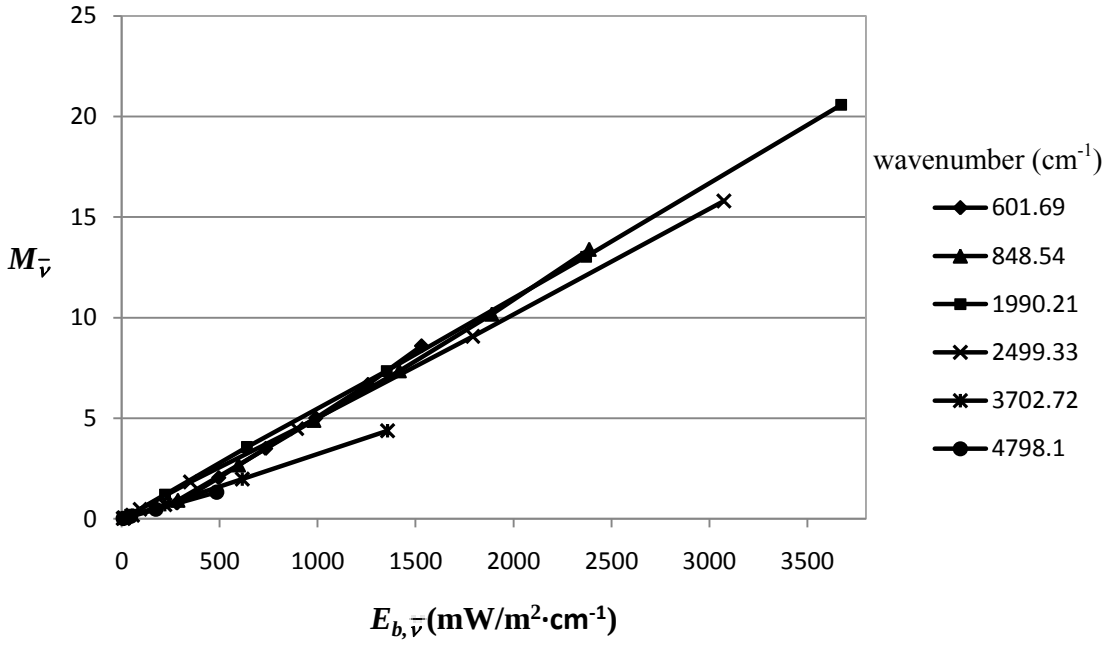

Figure 4-7. FTIR signals for various wavenumbers plotted as functions of the blackbody emissive power over a range of temperatures.

A closer look (Figure 4-8) reveals that the lines do not pass exactly through the origin. This offset in the spectral response is a result of the elevated temperature of the detector due to the surroundings when the detector is not being directly irradiated by a source.

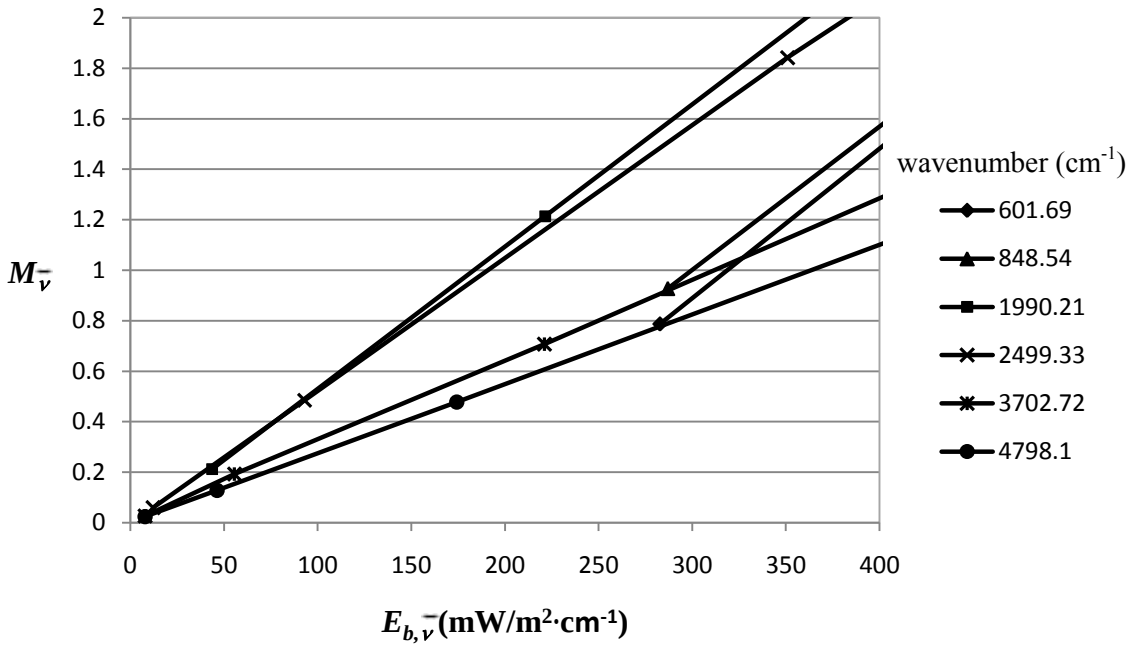

Figure 4-8. FTIR signals for various wavenumbers plotted as functions of the blackbody emissive power over a range of temperatures.

The equation for each line follows the slope-intercept form, $y = mx + b$. Eq. (4-21) can be combined with Eq. (4-1) can be put into this form as follows.

$$M_{\bar{\nu}} = \frac{1}{g a_{\bar{\nu}}} \varepsilon_{\bar{\nu}} E_{b,\bar{\nu}}(T_S) - \frac{b_{\bar{\nu},T_d,T_{sur}}}{a_{\bar{\nu}}} \qquad \textbf{(4-22)}$$

The analytically derived instrument response function in Eq. (4-21) correctly corresponds to the response of the FTIR spectrometer observed experimentally. Figure 4-9 shows the graphical representation of each term of the instrument response function.

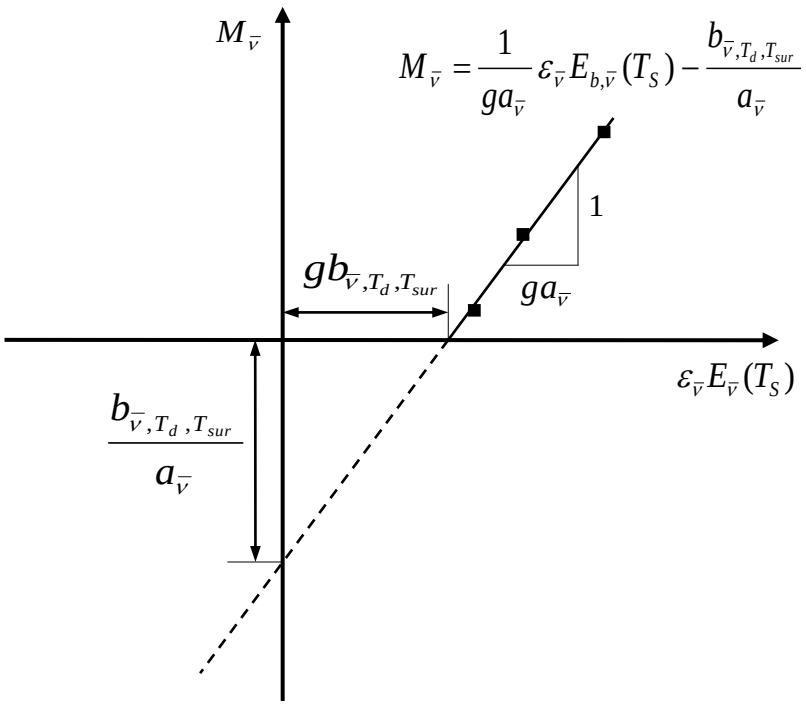

Figure 4-9. Graphical representation of each term of the instrument response function.

4.4.1 Calculation of the Instrument Response Function

In addition to being spectrally dependent, the instrument response function is highly dependent on the geometry of the radiation source and on the optical path between the source and the FTIR spectrometer. It is also dependent on the temperature of the detector and the temperature of the spectrometer. The instrument response function must therefore be determined for a specific set of conditions. In order to determine the response function under a given set of conditions, calibration of the system is required. The spectral emittance of the source as well as the source temperature must be known.

The calibration procedure consists of heating the source to a number of known temperatures. For each wavenumber, a line is fit to the data sets $[\varepsilon_{\bar{\nu}} E_{b,\bar{\nu}}(T_S),\ M_{\bar{\nu}}]$ over the

range of temperatures. The $ga(\bar{\nu})$ term of the response function is simply the inverse of the slope of the line fit to the data. The $gb(\bar{\nu}, T_d, T_{sur})$ term corresponds to the line's intercept with the $\varepsilon_{\bar{\nu}} E_{b,\bar{\nu}}(T_S)$ axis, as seen in Figure 4-9. Once these parameters are known for all wavenumbers in the desired band, the instrument response function is complete and the spectral emissive power of the radiation source can be calculated from Eq. (4-21).

4.4.2 Numerical Investigation

A numerical investigation was performed in order to assess the significance of the $gb(\bar{\nu}, T_d, T_{sur})$ (offset) term of the instrument response function. An arbitrary spectral emittance profile was created for a selected temperature (shown in Figure 4-10).

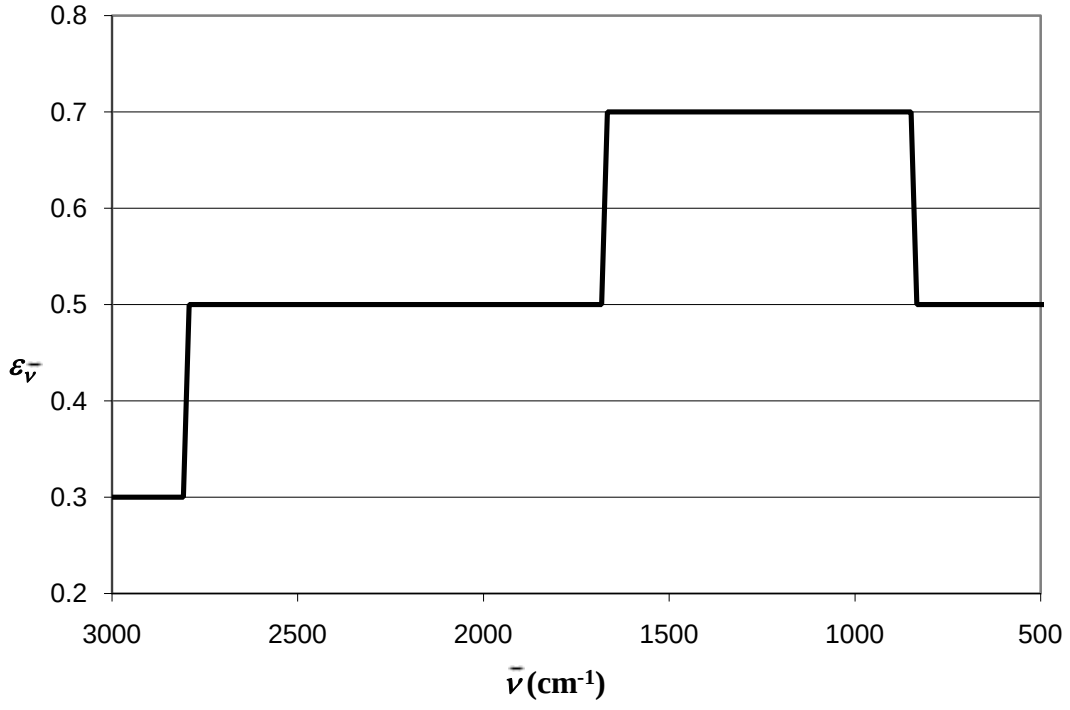

Figure 4-10. Spectral emittance used in numerical experiments designed to assess the importance of each term of the instrument response function.

Equation (4-3) was used to calculate $E_{\bar{\nu}}(\bar{\nu},T)$ for the given spectral emittance. The corresponding spectral signal, $M_{\bar{\nu}}$, was calculated using Eq. (4-21) and the terms from an instrument response function that was found experimentally. The spectral emittance was recreated using Eqs. (4-21) and (4-3) with and without the $gb(\bar{\nu},T_d,T_{sur})$ term. The results are shown in Figure 4-11. When the $gb(\bar{\nu},T_d,T_{sur})$ term was neglected, the average error from the actual spectral emittance was 8.2%. Based on this analysis, the $gb(\bar{\nu},T_d,T_{sur})$ term of the instrument response function cannot be neglected.

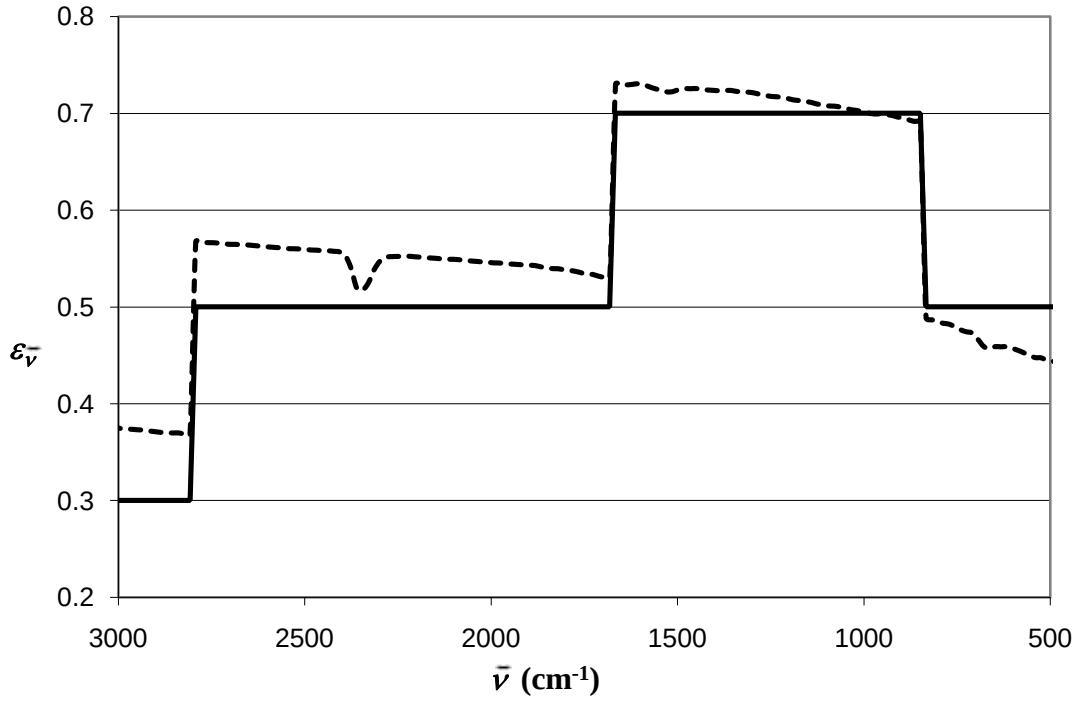

Figure 4-11. Comparison of the spectral emittance profile calculated using the instrument response function with the *gb* term (solid line) and without the *gb* term (dashed line).

4.5 Surface Temperature Measurement

In order to calculate the spectral emittance of a given object, the object surface temperature must be known. The temperature of a radiation source can be extracted from the FTIR spectrometer data. A common method of obtaining temperature information from a known spectral emissive power is the two-color technique [23]. The two-color technique is a ratio thermometry method that is used to infer the temperature of an object using the ratio of the emissive power at two wavenumbers (or colors). The blackbody spectral emissive power is given by the Planck function according to Eq. (4-2). The spectral emissive powers, E_1 and E_2, at two arbitrary wavenumbers, $\bar{\nu}_1$ and $\bar{\nu}_2$ respectively, can be written as

$$E_1(T) = \frac{\pi \varepsilon_1 \alpha_1 \bar{\nu}_1^3}{\exp(\alpha_2 \bar{\nu}_1 / T) - 1} \quad \textbf{(4-23)}$$

$$E_2(T) = \frac{\pi \varepsilon_2 \alpha_1 \bar{\nu}_2^3}{\exp(\alpha_2 \bar{\nu}_2 / T) - 1} \quad \textbf{(4-24)}$$

where ε_1 and ε_2 are the target emittances at wavenumbers $\bar{\nu}_1$ and $\bar{\nu}_2$, respectively. Using Wien's approximation [20], Eqs. (4-23) and (4-24) can be approximated as Eqs. (4-25) and (4-26), respectively.

$$E_1(T) = \frac{\pi \varepsilon_1 \alpha_1 \bar{\nu}_1^3}{\exp(\alpha_2 \bar{\nu}_1 / T)} \quad \textbf{(4-25)}$$

$$E_2(T) = \frac{\pi \varepsilon_2 \alpha_1 \bar{\nu}_2^3}{\exp(\alpha_2 \bar{\nu}_2 / T)} \quad \textbf{(4-26)}$$

Wien's approximation is valid if the $\exp(\alpha_2 \bar{\nu} / T)$ term is much greater than 1.

The temperature is found by taking the ratio of the two spectral emittances.

$$\frac{E_2}{E_1} = \frac{\varepsilon_2 \alpha_1 \bar{\nu}_2^3 / \exp(\alpha_2 \bar{\nu}_2 / T)}{\varepsilon_1 \alpha_1 \bar{\nu}_1^3 / \exp(\alpha_2 \bar{\nu}_1 / T)} \tag{4-27}$$

Taking the natural logarithm of both sides of Eq. (4-27) yields

$$\ln\left(\frac{E_2}{E_1}\right) = \ln\left(\frac{\varepsilon_2}{\varepsilon_1}\right) + 3\ln\left(\frac{\bar{\nu}_2}{\bar{\nu}_1}\right) + \frac{\alpha_2 \bar{\nu}_1}{T} - \frac{\alpha_2 \bar{\nu}_2}{T} \tag{4-28}$$

Equation (4-28) can be solved for the surface temperature *T*.

$$\frac{1}{T} = \frac{1}{\alpha_2(\bar{\nu}_1 - \bar{\nu}_2)}\left[\ln(E_2/E_1) - \ln(\varepsilon_2/\varepsilon_1) - 3\ln(\bar{\nu}_2/\bar{\nu}_1)\right] \tag{4-29}$$

If the emittances at both wavenumbers are the same, then the $\ln(\varepsilon_2/\varepsilon_1)$ term is zero and Eq. (4-29) reduces to

$$\frac{1}{T} = \frac{1}{\alpha_2(\bar{\nu}_1 - \bar{\nu}_2)}\left[\ln(E_2/E_1) - 3\ln(\bar{\nu}_2/\bar{\nu}_1)\right] \tag{4-30}$$

The accuracy of the two-color ratio method described above can be improved by using multiple wavenumbers instead of only two. It is necessary to use such a band of wavenumbers in the experiments described in this work because the gas interference in the spectra needs to be averaged out.

As stated above, the primary assumption of the two-color technique is that the emittance of the object is the same at both wavenumbers. This assumption allows the emittances to drop out. Similarly, a band of wavenumbers can be approximated as gray. Again, this approximation eliminates the emittance from the ratio of the spectral emissive powers at different wavenumbers and leaves the temperature of the source as the only unknown. The spectral emissive power of a source is found from the instrument response function. Assuming that there is a band comprised of *n* wavenumbers that can be

approximated as gray. The ratio of the emissive power at each of the *n* wavenumbers to the emissive power at any given reference wavenumber can be taken. The ratios of each of the blackbody emissive powers at the same wavenumbers can be found using the Planck function as follows.

$$\begin{aligned}
\frac{E_{b,1}}{E_{b,1}} &= \frac{\varepsilon_1 \alpha_1 \bar{\nu}_1^3 / (\exp(\alpha_2 \bar{\nu}_1 / T) - 1)}{\varepsilon_1 \alpha_1 \bar{\nu}_1^3 / (\exp(\alpha_2 \bar{\nu}_1 / T) - 1)} \\
\frac{E_{b,2}}{E_{b,1}} &= \frac{\varepsilon_2 \alpha_1 \bar{\nu}_2^3 / (\exp(\alpha_2 \bar{\nu}_2 / T) - 1)}{\varepsilon_1 \alpha_1 \bar{\nu}_1^3 / (\exp(\alpha_2 \bar{\nu}_1 / T) - 1)} \\
&\vdots \\
\frac{E_{b,n}}{E_{b,1}} &= \frac{\varepsilon_n \alpha_1 \bar{\nu}_n^3 / (\exp(\alpha_2 \bar{\nu}_n / T) - 1)}{\varepsilon_1 \alpha_1 \bar{\nu}_1^3 / (\exp(\alpha_2 \bar{\nu}_1 / T) - 1)}
\end{aligned} \qquad \textbf{(4-31)}$$

If the spectral region of interest ($\bar{\nu}_1, \bar{\nu}_2, \ldots, \bar{\nu}_n$) is gray, then the unknown spectral emittances in the ratios in Eq. (4-31) can be cancelled out. The source temperature, *T*, is now the only unknown on the right side of the equations. The temperature in the Planck function is adjusted such that the error between the ratios of the spectral emissive powers is minimized. This technique provides an approximation of the source surface temperature. A spectral band from 2453 cm^{-1} to 2947 cm^{-1} is assumed to be gray for all temperature measurements in this document. The accuracy of this approximation is addressed in section 8.1.

4.6 Total Emittance

Once the spectral emittance is known, the total emittance can be calculated from Eq. (4-32) [20]. Note that the following equations are presented in wavelength instead of wavenumber.

The fractional function defined in Eq. (4-32) is most commonly available in terms of wavelength.

$$\varepsilon \equiv \frac{E(T)}{E_b(T)} = \frac{\int_0^\infty \varepsilon_\lambda(T) E_{\lambda,b}(T) d\lambda}{E_b(T)} \tag{4-32}$$

Equation (4-32) can be approximated as the sum

$$\varepsilon \approx \sum_{i=1}^{\infty} \varepsilon_{AVG(i,i-1)} \left[F(\lambda_i T) - F(\lambda_{i-1} T) \right] \tag{4-33}$$

where F is the fraction of the total emission from a blackbody that is in a certain spectral band. The fractional function F is defined as [20]

$$F(\lambda T) \equiv \frac{\int_0^\lambda E_{\lambda,b} d\lambda}{E_b} \tag{4-34}$$

Wiebelt provides the following approximation of the fractional function [30].

$$\begin{aligned} F(\lambda T) &\approx \frac{15}{\pi^4} \sum_{m=1,2,\ldots} \frac{e^{-mx}}{m^4} \left\{ \left[(mx+3)mx + 6 \right] mx + 6 \right\}, \\ x &= \frac{C_2}{\lambda T} > 2 \\ F(\lambda T) &\approx \frac{15}{\pi^4} x^3 \left(\frac{1}{3} - \frac{x}{8} + \frac{x^2}{60} - \frac{x^4}{5040} + \frac{x^6}{272{,}160} - \frac{x^8}{13{,}305{,}600} \right), \\ x &= \frac{C_2}{\lambda T} < 2 \end{aligned} \tag{4-35}$$

In Eq. (4-35), C_2 = 14388 μm·K is the second radiation constant.

4.7 Summary

In order to calculate the spectral emittance of an ash deposit, the ash layer spectral emissive power and the deposit surface temperature are required. An FTIR spectrometer collects the radiant energy from the ash deposit. An instrument response function relates

the FTIR signal to the spectral emissive power of the ash deposit. The deposit surface temperature is found by fitting gray bands of the spectral emissive power of the ash layer to the blackbody spectral emissive power (the Planck function).

5 Verification of the Method of Measuring the Spectral, Hemispherical Emittance with a Blackbody Radiator

The methods developed in Chapter 4 to find the instrument response function and the source temperature were verified using the experimental setup shown in Figure 4-5. A blackbody radiator was used as the source of radiation because both its temperature and emittance are known, allowing for the quantification of the error in the developed methods.

5.1 Instrument Response Function from Blackbody Radiator

Spectra were collected at ten different blackbody radiator temperatures over the range of 100ºC to 1000ºC. The emittance was assumed to be unity at all wavenumbers. Figure 5-1 and Figure 5-2 show the corresponding $ga(\bar{v})$ and $gb(\bar{v},T_d,T_{sur})$ terms of the response function, respectively. Because of the large CO_2 absorption band around 2400 cm^{-1}, a small spectral band is removed from these and all of the following figures.

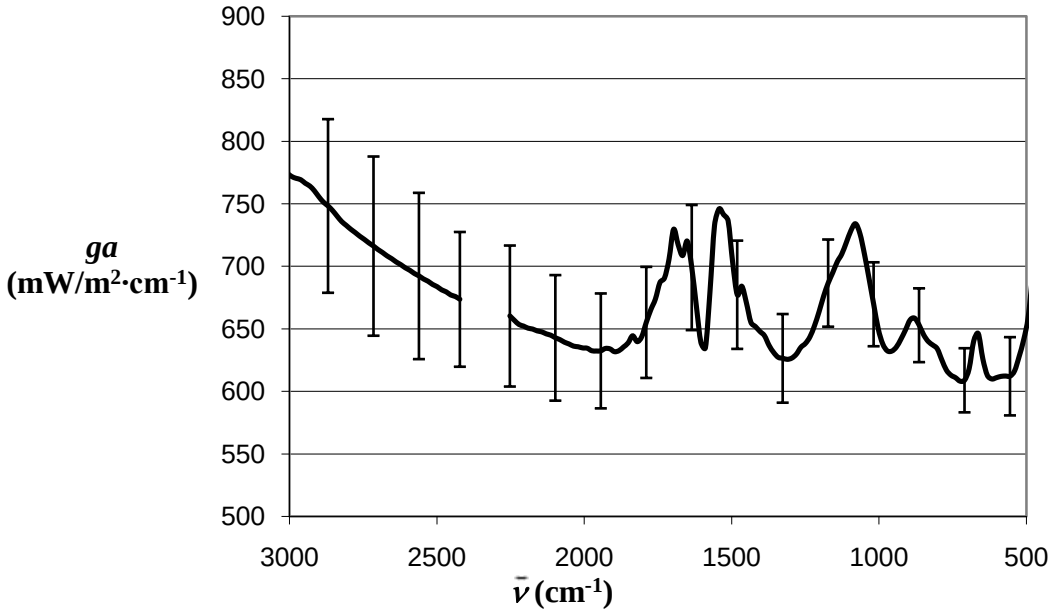

Figure 5-1. First term of the instrument response function found for a blackbody radiator.

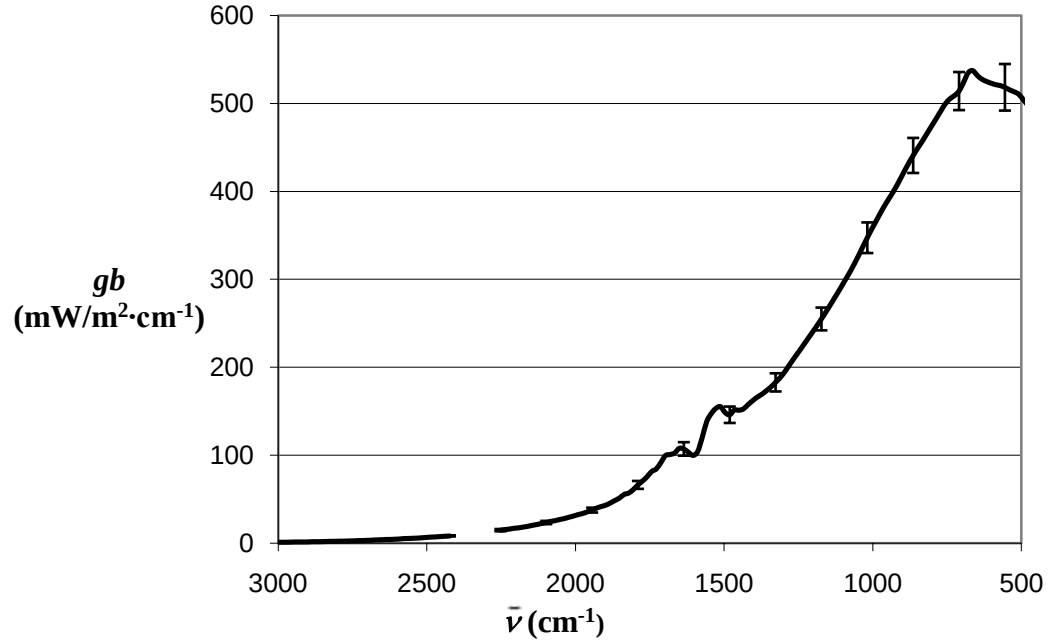

Figure 5-2. Second term of the instrument response function found for a blackbody radiator.

5.2 Temperature of Blackbody Radiator

In order to verify the method of estimating the source temperature described in section 4.5, a spectrum was collected at a number of randomly chosen temperatures of the blackbody source of between 100 º C and 1000 º C. These temperatures were not used in the procedure to find the instrument response function. The spectral band used to find the temperatures consisted of wavenumbers from 2453 cm^{-1} to 2947 cm^{-1}. As an example, the temperature measurement technique resulted in a temperature of 165º C when the blackbody radiator temperature was set at 167.5 C. The average difference between the temperature displayed by the blackbody radiator and that calculated was 1.2%.

5.3 Spectral Emittance of Blackbody Radiator

Figure 5-3 compares the spectral emissive power of the blackbody radiator at a random temperature calculated from the instrument response function to the spectral emissive power calculated using the Planck function at the given temperature. The spectral band used to find the temperature is also shown.

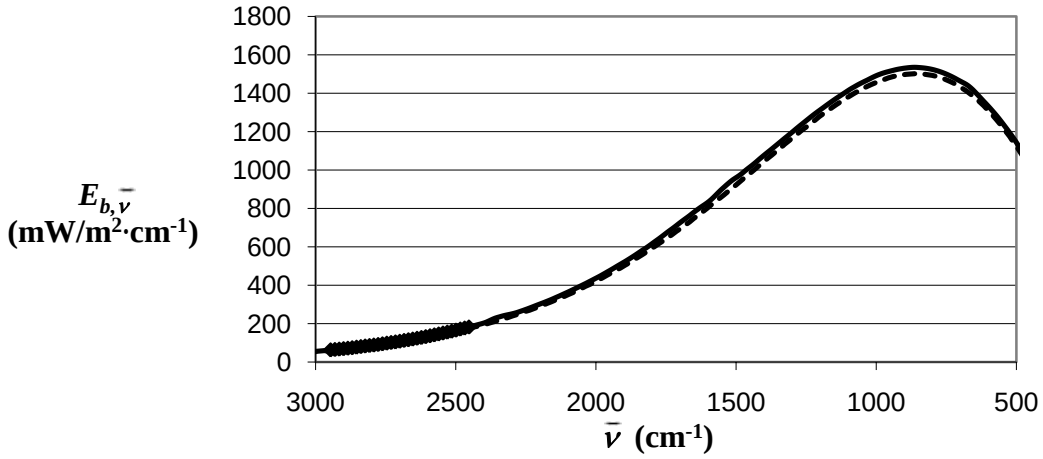

Figure 5-3. Comparison of the spectral emissive power of a blackbody radiator calculated from the Planck function (dashed line) and from the instrument response function (solid line). The gray band used to infer the temperature is also shown (thick line).

The spectral emittance of the blackbody radiator was calculated using Eq. (4-1) and is shown in Figure 5-4.

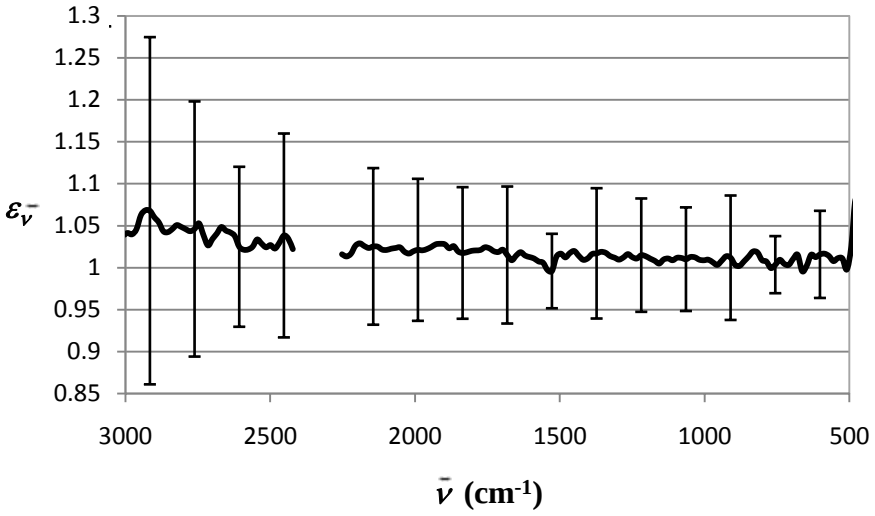

Figure 5-4. Spectral emittance of the blackbody radiator calculated using the instrument response function.

If the actual spectral emittance of the blackbody radiator is assumed to be unity, then the average error in the measured spectral emittance is 2.1%. There are a number of possible explanations to why the measured spectral emittance is slightly higher than the actual spectral emittance. The small error in the inferred temperature calculated in section 5.3 had a relatively large effect on the measured spectral emittance of the blackbody radiator. If there were no error in the temperature measurement technique, the error in the measured spectral emittance would be 0.84%. This error is due to the fact that the temperatures used to verify the technique were selected randomly and were not used in creating the instrument response function. Another possible source of error is the emission from the mirror. Radiation from the blackbody may have heated up the mirror enough such that the emission from the mirror was not negligible.

5.4 Total Emittance of Blackbody Radiator

The equations presented in section 4.6 were used to calculate the total emittance of the blackbody radiator. The measured spectral emittance is not known beyond the spectral limits of the FTIR detector. According to Eq. (4-32), the spectral emittance over the entire spectrum is required to calculate the total emittance. The emittances at all wavenumbers below the lower limit of the detector are assumed to be the value at the lowest known wavenumber. Similarly, the emittance value at the highest known wavenumber is used for all wavenumbers above the upper limit. Figure 5-5 shows spectral emittance with the Planck function. The spectral emittance approximation below the lower limit of the detector has a significant effect on the total emittance while that above the upper limit has a negligible effect. The average total emittance found from all of the randomly selected temperatures was determined to be 1.02 and the error was 2.0%.

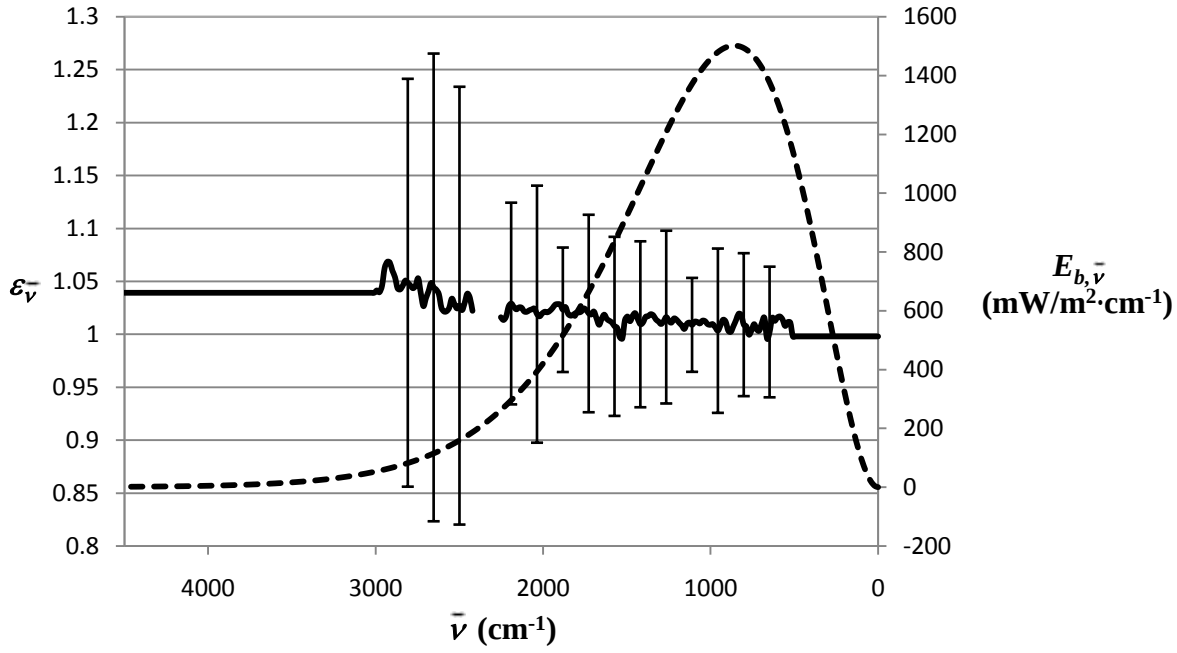

Figure 5-5. Spectral emittance of the blackbody radiator (solid line) with the assumed emittance beyond the spectral limits of the detector. Also shown is the Planck function (dashed line) at the blackbody temperature.

5.5 Analysis of the Instrument Response Function

The importance of each term in the instrument response function is now presented. To illustrate the importance of the $gb(\bar{\nu},T_d,T_{sur})$ term, the spectral emittances calculated from the instrument response function with and without this term are shown in Figure 5-6.

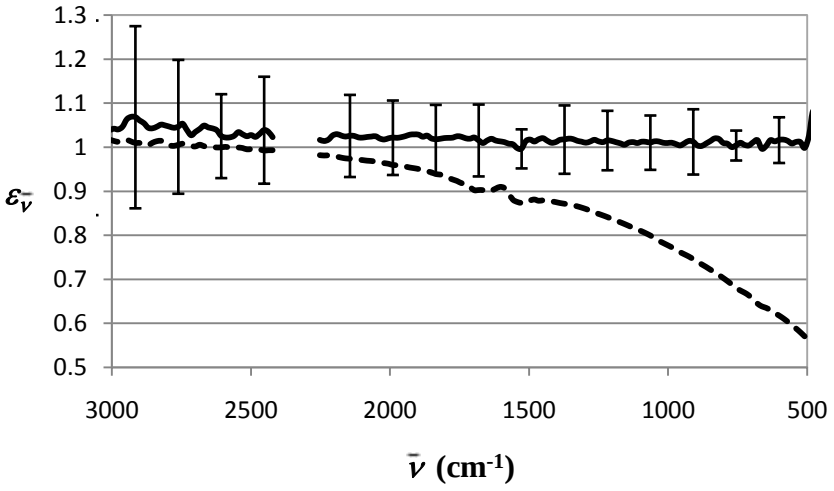

Figure 5-6. Comparison of the spectral emittance of the blackbody radiator calculated from the instrument response function with (solid line) and without (dashed line) the *gb* term.

The $gb(\bar{\nu},T_d,T_{sur})$ term compensates for the signal output by the FTIR when there is no source. This signal results from the temperature of the detector. It is clear from Figure 5-6 that this term is an essential component of the instrument response function. In order to minimize the offset resulting in the temperature of the detector, the FTIR spectrometer was purged with nitrogen throughout all experiments discussed in this document. Figure 5-7 shows the results of an experiment conducted to see the effects of the nitrogen purge on the response function. The response function was found twice under the exact same conditions, except the FTIR was purged with nitrogen during one experiment and not

purged during the other. The changes in the instrument response function caused by purging the FTIR with nitrogen were within the variation of the response function measurements. Therefore, the nitrogen purge had little to no effect on the experiments.

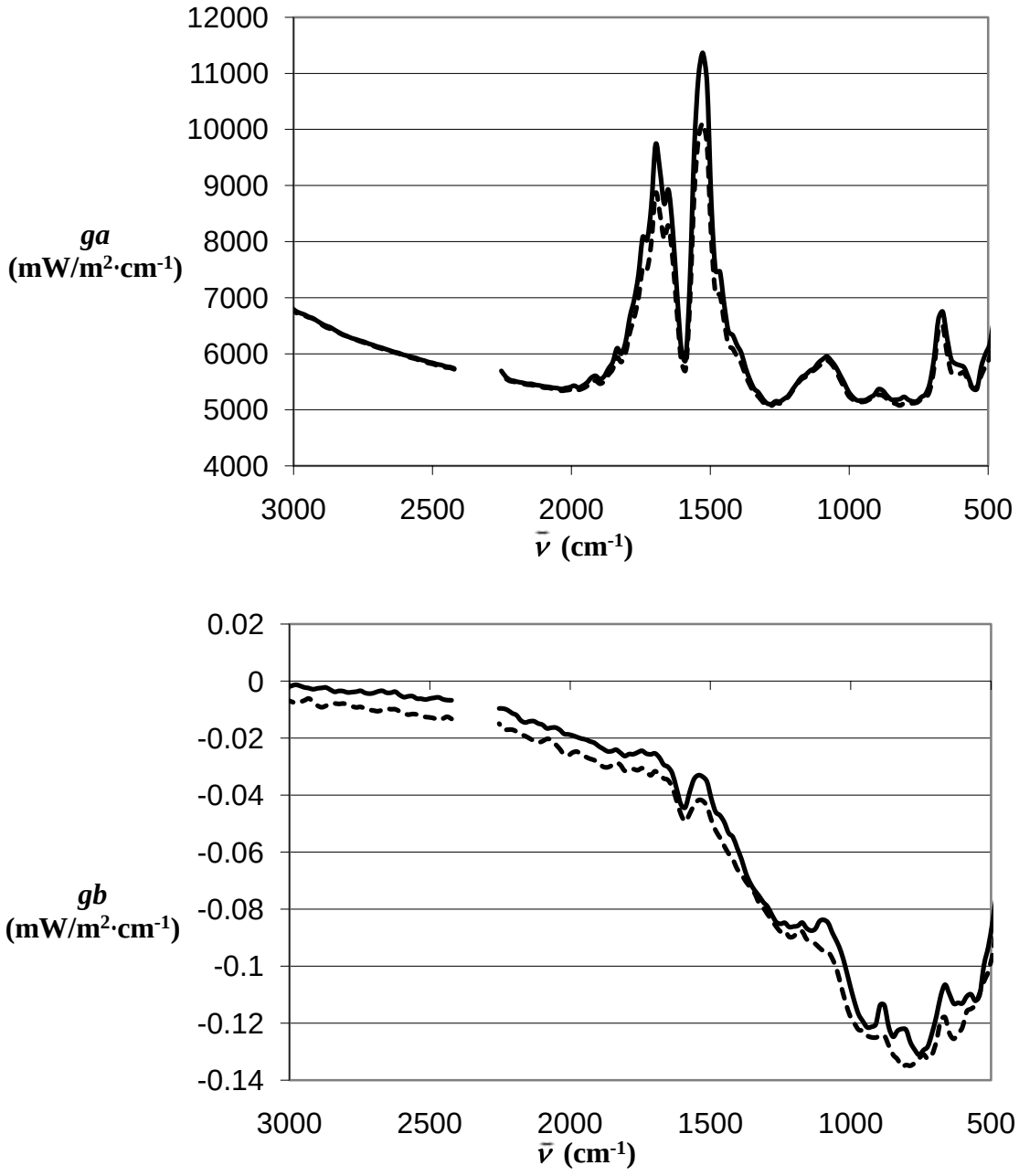

Figure 5-7. Comparison of the first (top) and second (bottom) terms of the instrument response function with (solid line) and without (dashed line) the FTIR nitrogen purge.

The instrument response function depends on the conditions of the surroundings. These conditions can change from day to day. Figure 5-8 illustrates the importance of finding the response function on the day that the experiments are conducted. This figure shows the $gb(\bar{\nu}, T_d, T_{sur})$ term of the instrument response function found on two different days. The experimental setup and procedure were identical on both days, but the response functions show modest differences.

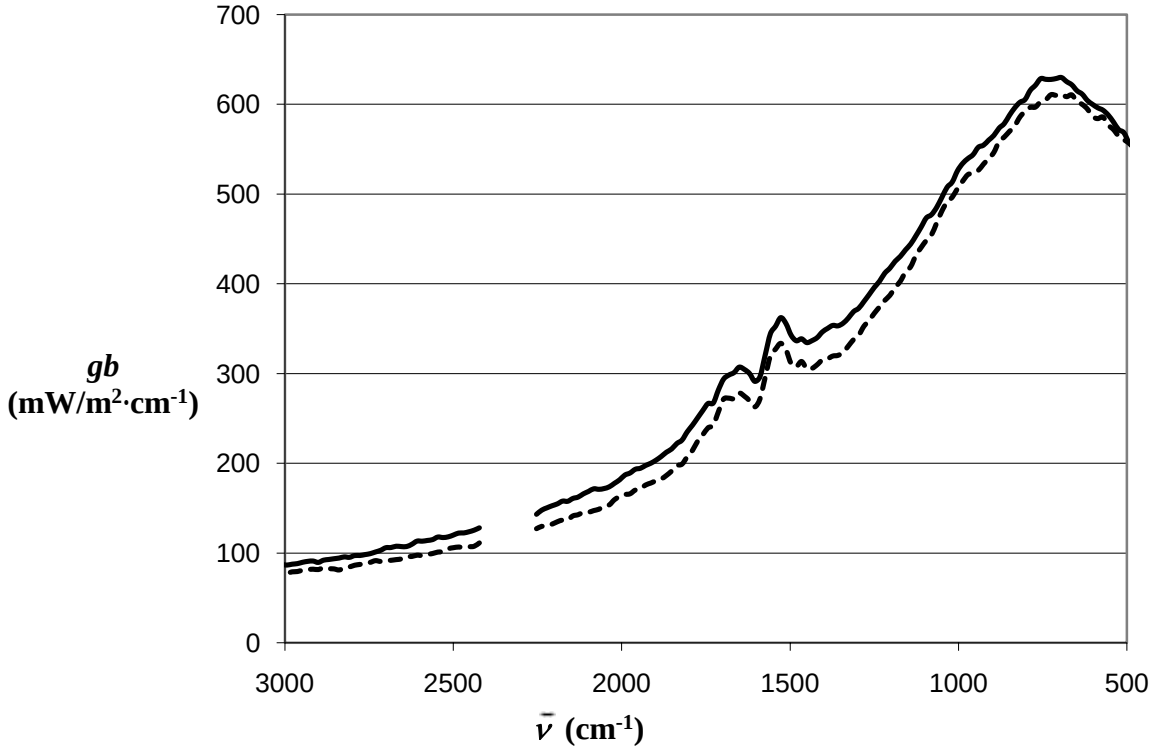

Figure 5-8. Comparison of the *gb* term of the instrument response function calculated on two different days: day 1 is the dashed line and day 2 is the solid line.

Unlike the $gb(\bar{\nu}, T_d, T_{sur})$ term of the response function, the $ga(\bar{\nu})$ term is independent of detector and surrounding temperatures and is only a function of wavenumber and optical path geometry. The $ga(\bar{\nu})$ terms of the instrument response function corresponding to the

$gb(\bar{\nu}, T_d, T_{sur})$ terms found on different days are shown in Figure 5-9. They demonstrate that surrounding conditions have no impact on the $ga(\bar{\nu})$ part of the response function.

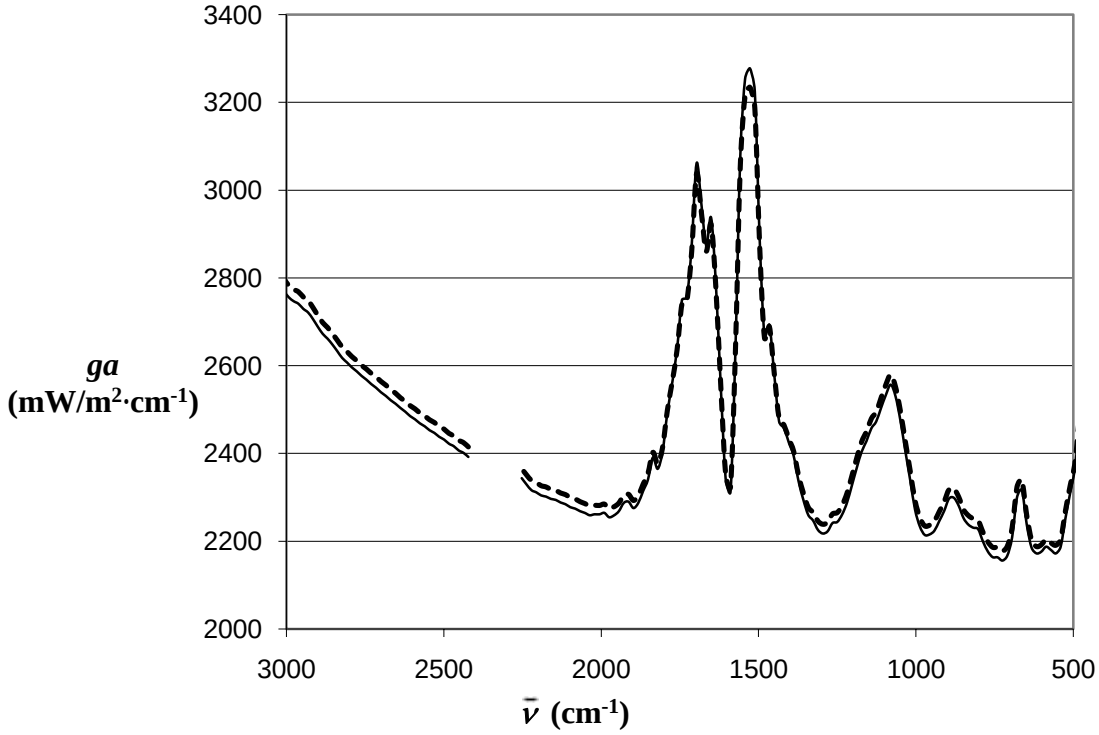

Figure 5-9. Comparison of the *ga* term of the instrument response function calculated on two different days: day 1 is the dashed line and day 2 is the solid line.

The presence of the geometric parameter, *g*, shows that the instrument response function is highly dependent on the geometry of the radiation source and the optical path between the source and the FTIR spectrometer. The experiment described in section 5.1 was performed under various geometric configurations. For example, mirrors of different focal lengths were used. The results were consistent with those presented. Figure 5-10 shows the change in the $ga(\bar{\nu})$ term resulting from changing the optical path (by changing the aperture size).

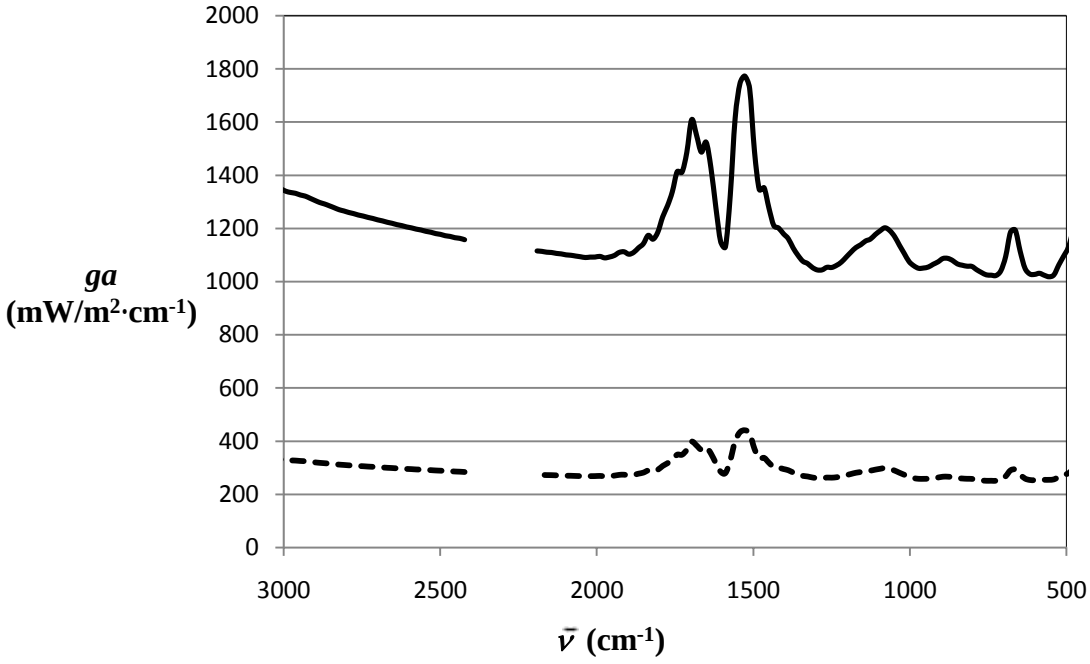

Figure 5-10. Comparison of the *ga* term of the instrument response function calculated from two different optical path geometries: a 3mm aperture corresponds to the solid line and a 7mm aperture to the dashed line.

5.6 Summary

A blackbody radiator was used as the radiation source in order to verify the methods developed to measure the spectral emissive power and source temperature. An instrument response function was created by collecting spectra at eight known blackbody temperatures. Spectra were collected at six randomly selected temperatures not used in the calibration. These six spectra were used to quantify the error in using the techniques developed to measure the temperature and spectral emissive power of the source. The average difference between the inferred temperature and that displayed on the blackbody radiator was 1.2% and the average error in the spectral emissive power was 3.29%. The error in the total emittance was 1.81%. The importance of each term of the instrument

response function was also assessed. It was concluded that due to the dependence of the instrument response function on surrounding conditions and on optical path geometry, the system would require calibration before each deposition experiment.

6 Spectral Emittance of Ash Deposits

This chapter discusses the use of the techniques established in Chapter 3 to make *in situ* emittance measurements of ash deposits.

6.1 Oxidizing Conditions - Experimental Setup

In addition to the experimental setup described in the Chapter 3, other instruments were required to make the desired *in situ* measurements of the ash deposits. A schematic of the experimental setup is shown in Figure 6-1.

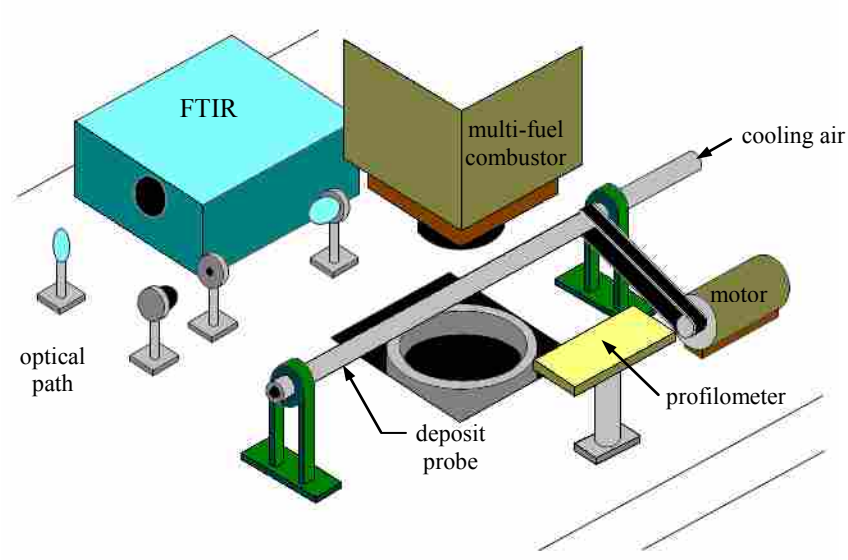

Figure 6-1. Schematic of the experimental setup used to make emittance measurements of ash deposits.

The thickness of the ash layer on the probe is measured with a profilometer. Cundick provides detailed information on the use of the profilometer to measure the thickness of the ash deposit as a function of deposition time [28]. The radiosity from the ash deposit is directed through an optical path into the FTIR spectrometer. A Nicolet 8700 FTIR spectrometer was used in all experiments discussed in this work.

The optical path consists of two off-axis parabolic mirrors, an aperture, and a turning mirror. A schematic of the optical path is shown in Figure 6-2. A 90º off-axis parabolic mirror is placed two focal lengths away from the probe surface. The radiation from the source is turned 90º, focused, and passed through a 3*mm* diameter aperture. The aperture acts as a spatial filter, eliminating any stray radiation that may enter the optical path. Another 90º off-axis parabolic mirror is placed one focal length from the aperture. This mirror turns the light 90º and collimates it. Lack of space on the optical table required the use of a turning mirror to direct the collimated light into the spectrometer.

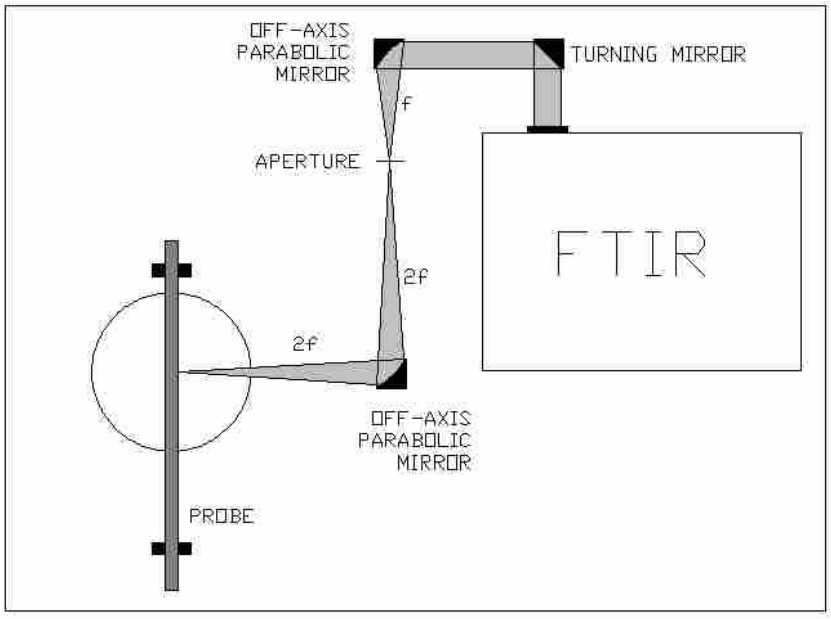

Figure 6-2. Schematic of the optical path directing the radiant energy from the deposit probe into the FTIR spectrometer (top view).

6.1.1 Optical Path Alignment

An alignment procedure was developed in order to ensure that the optical path was correctly set up and that the spectrometer was correctly collecting radiation from a point on the surface of the test probe. A 3*mm* diameter aperture is placed in the reactor outlet. This aperture corresponds with the point at which radiation will be collected from the deposit probe during the deposition experiments. On the left side of the aperture, an optical path consisting of two off-axis parabolic mirrors is set up which focuses the light from a source down to a point at the aperture center. The light emerging from the aperture follows the same path as the radiation coming from a point on the probe. The optical path on the right side of the aperture is set up as explained in section 6.1. As illustrated in Figure 6-3, a high-intensity light source is directed through the optical path and adjustments are made to the optical components. This is a coarse alignment and allows for visual verification of the optical path.

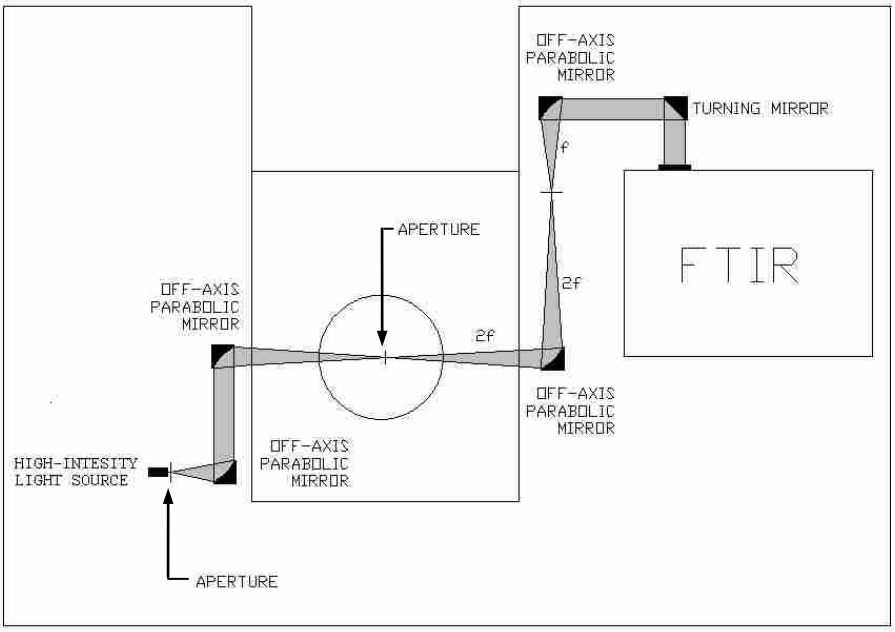

Figure 6-3. Schematic of the optical path used for the coarse alignment of the FTIR to the interrogation point in the reactor outlet.

The light source is replaced with a blackbody source, as shown in Figure 6-4. The optical components are fine-tuned such that the interferogram in the spectrometer is maximized. This procedure ensures the spectrometer is aimed directly at the aperture in the reactor outlet. The aperture location becomes the interrogation point where the probe surface must be located during the experiments. Two lasers are aimed at the interrogation point (see Figure 6-4). The center aperture and the left optical components are removed. The point in space where the two lasers intersect is the point of interrogation.

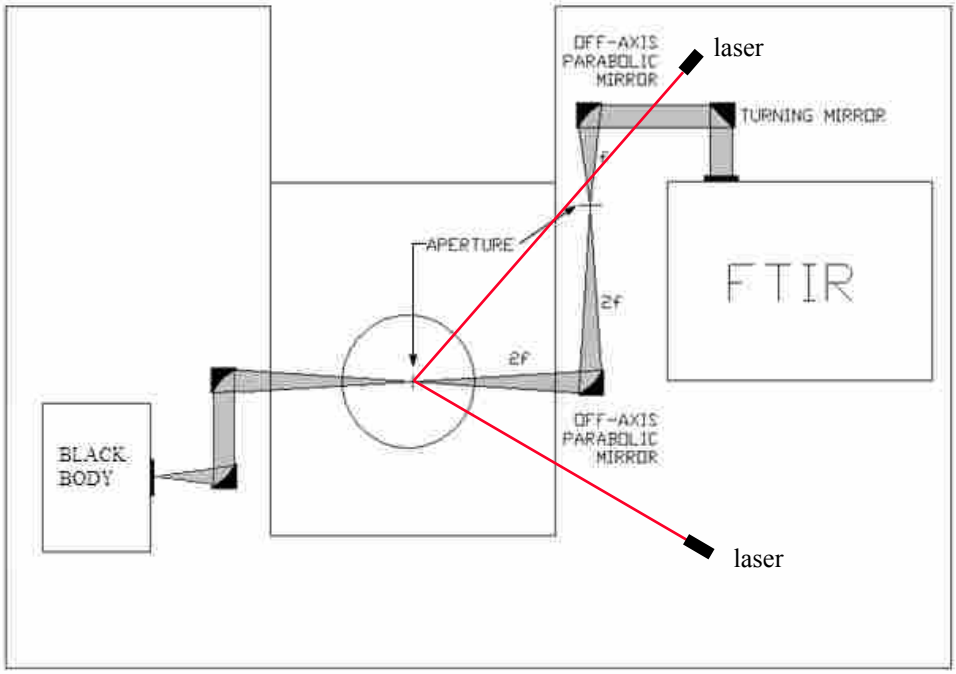

Figure 6-4. Schematic of the optical path used for the fine alignment of the FTIR to the interrogation point in the reactor outlet.

6.2 Instrument Response Function of the Deposition Probe

It was determined that the instrument response function is highly dependent on the geometry of the source. Therefore, in order to determine the spectral emittance of the ash deposit on the test probe, the response function must be found using the test probe as the source. The probe cannot change position between the calibration and experimental procedures. In order to find the response function the source temperature and spectral emittance of the source must be known. The probe is instrumented with thermocouples and is positioned in the reactor outlet such that the point of interrogation corresponds to a point adjacent to one of the external thermocouples on the probe. The probe is painted with a high-temperature, flat, black paint. The spectral emittance of the painted probe is determined in an independent experiment explained in section 6.2.2 below.

Because the response function depends on the geometry of the probe and on the daily conditions of the surroundings, a response function must be found every day that the experiments are conducted. When the reactor has reached the desired temperature for the experiment (1100 ºC), the painted probe is secured in the reactor outlet. After each experiment, the probe is cleaned of all ash and repainted. The probe is aligned such that a thermocouple is next to the point of interrogation. Cooling air is used to control the temperature of the probe. Spectra are collected from the probe at a number of temperatures and the instrument response function is created according to the procedure described in section 4.4.1.

6.2.1 Probe Reflections

Equation (4-21) is only applicable if the reflection from the probe is negligible. In order to ensure that this is the case, the probe is positioned such that the point of interrogation is on the shaded side. Figure 6-5 shows a picture of the deposition probe with the alignment lasers marking the interrogation point on the shaded side of the probe.

Figure 6-5. Point of interrogation on the shaded side of the probe marked by the intersection of the two alignment lasers.

An experiment was conducted to determine if collecting spectra from the shaded side of the probe was sufficient to neglect the reflection from the probe. All significant irradiation on the probe comes from the reactor. Spectra collected under normal conditions were compared to those collected when the outlet of the reactor was covered. Typical results are shown in Figure 6-6. The average difference between the spectra collected with reflection and those collected without reflection was 6.4%.

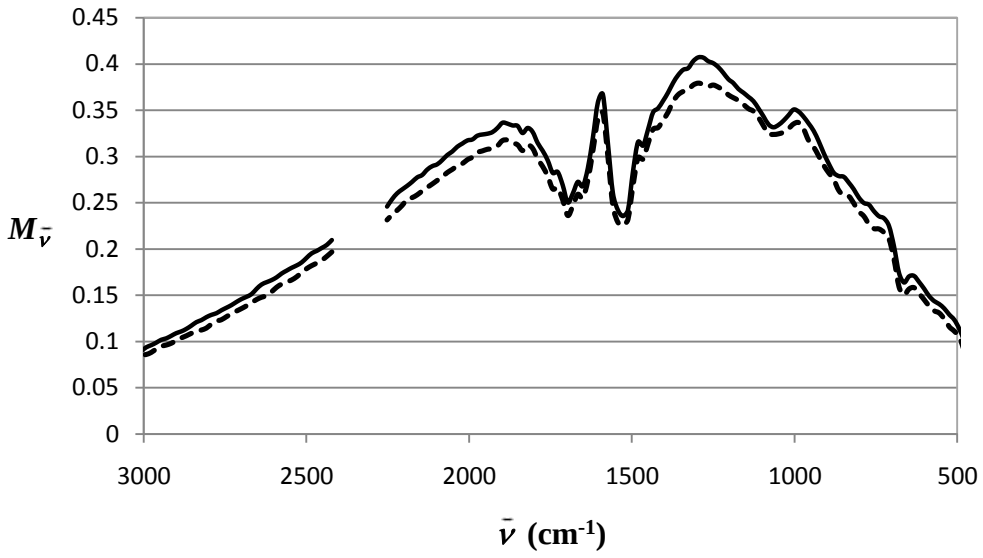

Figure 6-6. Comparison of the signal from the FTIR spectrometer with (solid line) and without (dashed line) reflection from the reactor tube.

6.2.2 Spectral Emittance of the Painted Probe

The spectral emittance of the cleaned, painted probe is required to find the instrument response function. The spectral emittance of an object is defined by Eq. (4-1). Figure 4-5 shows the optical path used to find the spectral emittance of the painted probe. The optical path alignment procedure is similar to that of the method used to align the optical path during the ash deposition experiments. An aperture is placed at the focal point of the off-axis parabolic mirror. A high-intensity fiber-optics light source is placed behind the aperture in order to emulate a point source. The aperture and mirror are adjusted such that the light from the mirror into the FTIR is collimated. The light source is replaced by the blackbody radiator. Fine adjustments are made to the mirror such that the interferogram signal is maximized. This ensures that the point of interrogation is at the aperture. Two lasers are aimed at the aperture from different angles such that their

point of intersection marks the point of interrogation. The aperture is removed and the probe surface is placed at the interrogation point. The probe is positioned such that one of the thermocouples embedded in its surface is close to the interrogation point. This thermocouple is used to monitor the surface temperature of the probe at the interrogation point. Heat guns are used to heat the probe to a specified temperature and a spectrum is collected. Figure 6-7 shows a picture of the experimental setup.

Figure 6-7. Experimental setup used to measure the spectral emittance of the clean, painted deposit probe.

The probe is replaced by the blackbody radiator. Spectra are collected at a number of blackbody temperatures and an instrument response function is created. The response function is used to find the spectral emittance of the painted probe according to Eq. (4-3). This experiment was performed at a number of different probe temperatures. The experiment was repeated periodically over the course of two months to ensure that the spectral emittance of the painted probe did not change significantly after cleaning and repainting the probe for each ash deposition experiment. Figure 6-8 shows the average

spectral emittance of the painted probe with representative error bars that indicate a 95% confidence interval. The error at a given wavenumber was found by multiplying the standard deviation at that wavenumber by the *t*-statistic value corresponding to the number of degrees of freedom (i.e. the number of experiments run minus one) for a 95% confidence interval. This spectral emittance was used in calculating the instrument response function at the beginning of each experiment.

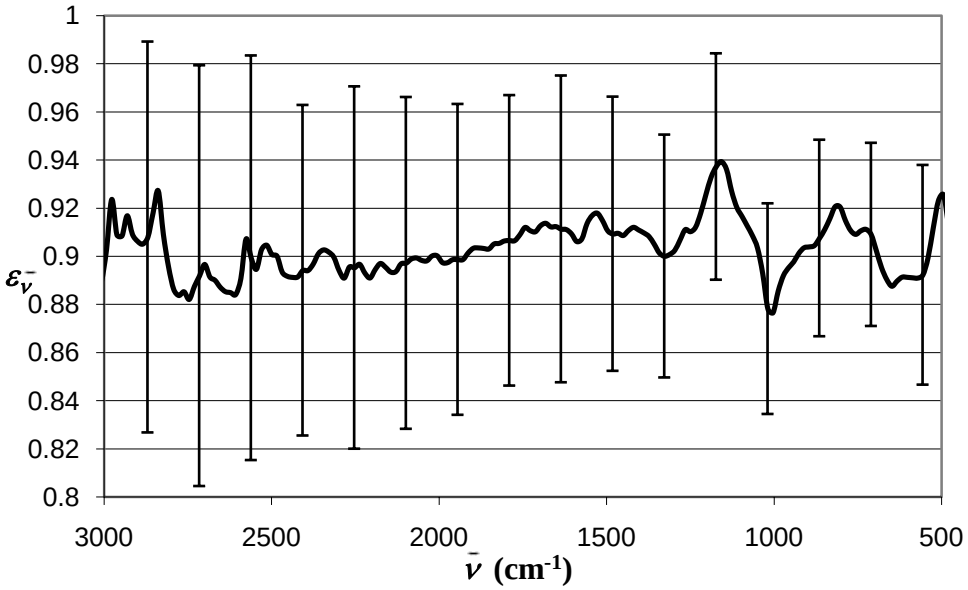

Figure 6-8. Spectral emittance of the clean, painted deposit probe.

6.3 Experimental Procedure

After the instrument response function is found, the deposition experiment is started. Pulverized coal (with a nominal size of 75 μm) is injected into the reactor at a feed rate of 3.5 pounds per hour. The probe is rotated at a rate of ¼ rpm. The probe rotation ensures that the ash is uniformly deposited on the probe. The thickness of the ash layer on the probe is measured using a laser range finder (profilometer). The probe is air

cooled such that the outer surface is maintained at a nominal temperature of 400ºC. Approximately every thirty minutes the coal is turned off and the probe rotation is stopped. When the probe temperatures reach steady state, a spectrum is collected.

6.3.1 Particle Cloud Interference

The coal must be stopped because the particle cloud surrounding the probe interferes with the signal from the ash layer. Figure 6-9 shows a comparison of the deposit probe with and without the particle cloud, while Figure 6-10 shows compared the high-resolution signals output by the FTIR with and without the particle cloud.

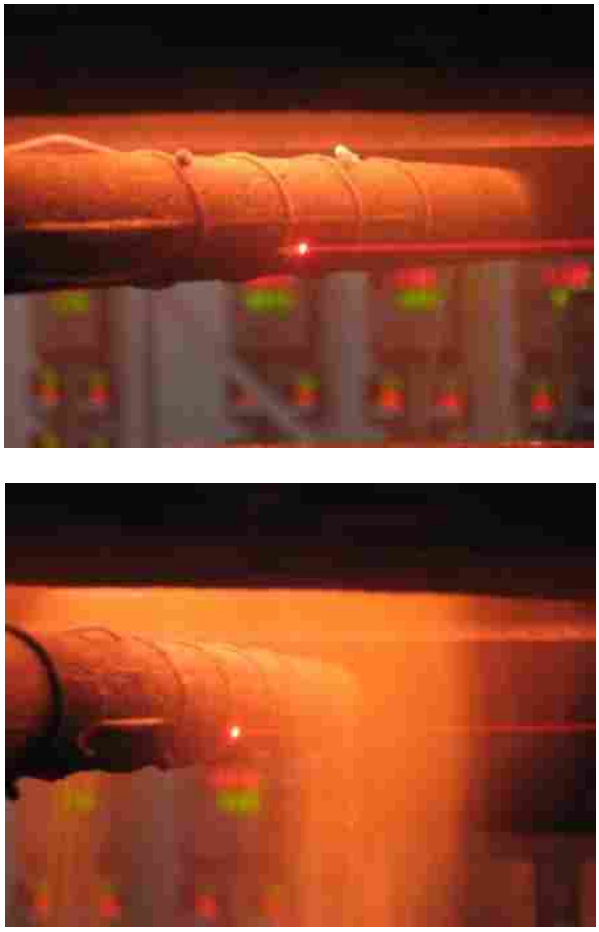

Figure 6-9. Comparison of the deposit probe without (top) and with (bottom) the particle cloud present when coal is being burned.

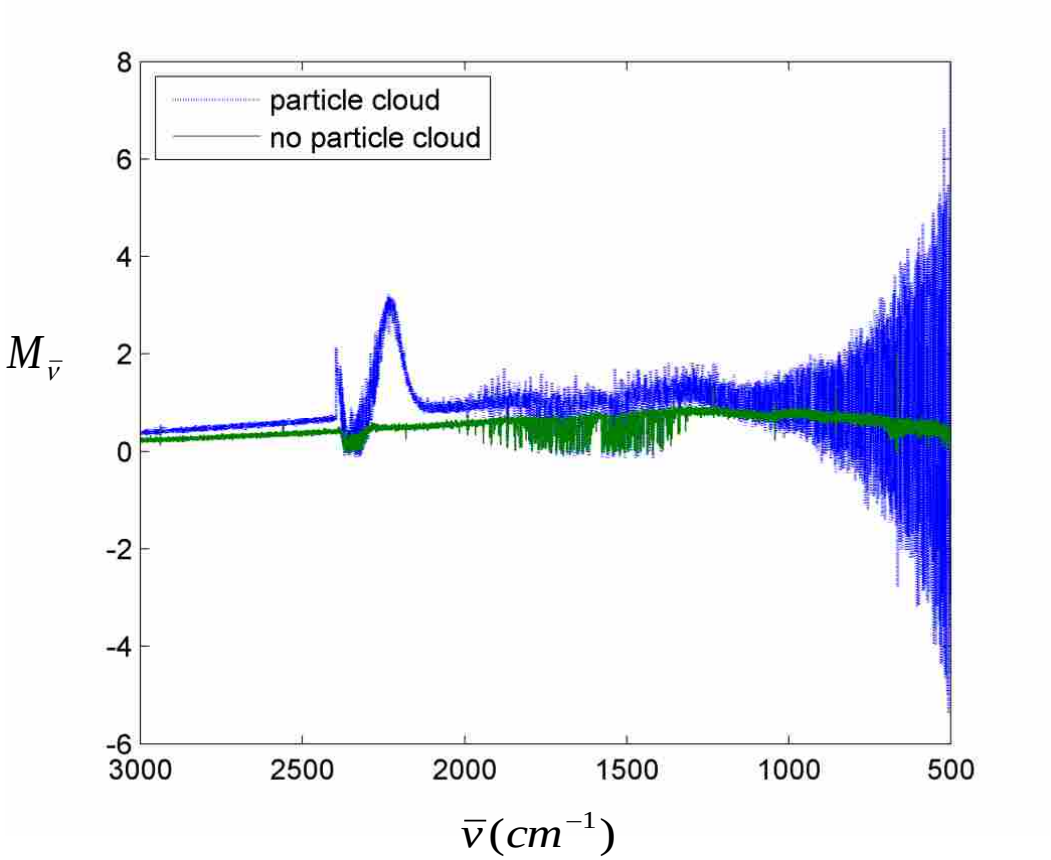

Figure 6-10. Comparison of the high-resolution signal from the FTIR with and without the particle cloud surrounding the deposit probe.

It is clear that the particle cloud interferes with the signal. The noise level is significantly higher, especially at lower wavenumbers. This interference significantly decreases the accuracy of the temperature inference technique described in section 4.5.

6.3.2 Probe Rotation

The probe rotation is stopped such that the probe is in the exact position as it was during the creation of the instrument response function. This minimizes the error caused by the probe being out of round. When the instrument response function is created, the probe is positioned such that the alignment lasers converge on the probe at the desired

point of interrogation. As the probe rotates, the laser points diverge and then converge again as the probe approaches the starting position. This divergence results from the probe being out of round. It is necessary, therefore, to stop the probe while spectra are being collected. An experiment was conducted in which the spectral emittance of the cleaned, painted probe was measured. Emittance measurements were made both when the probe was rotating and when the probe was stationary. No ash was on the probe during this experiment. Figure 6-11 compares the calculated spectral emittance of the probe for a rotating and non-rotating probe with the spectral emittance of the probe found in section 6.2.2.

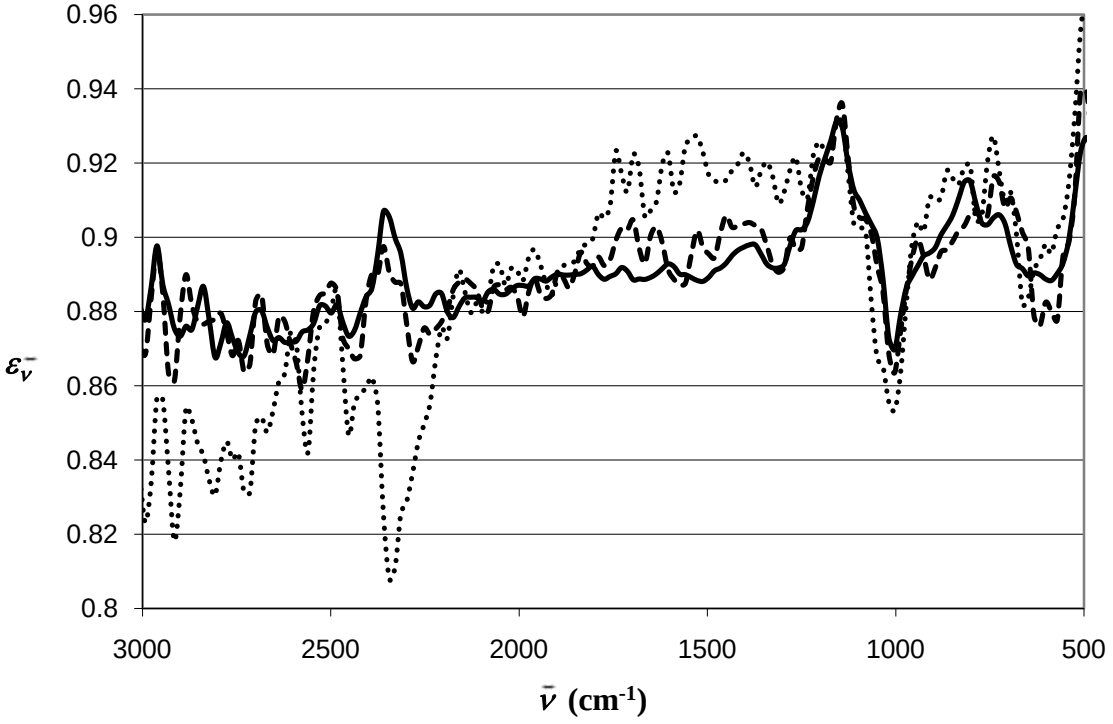

Figure 6-11. Comparison of the actual spectral emittance of the painted probe (solid line) to the spectral emittance calculated with (dotted line) and without (dashed line) the probe rotating.

The average error between the actual probe emittance and the calculated probe emittance when the probe was stationary was 0.66%. The error with the probe rotating was 2.3%. This error would increase significantly with the formation of an ash deposit. The growth of the ash deposit would cause a greater divergence from the original probe position. The surface temperature measurement was also affected by the probe rotation. Theoretically, the probe rotation would be slow enough such that at any given point, the probe surface temperature would remain at a steady state. In practice, however the probe rotation causes a temperature gradient within the point of interrogation.

6.4 Reducing Conditions - Experimental Setup

For the experiments performed under reducing conditions, the ash-deposition experimental setup and procedures were the same as those described in Chapter 3. A secondary methane lance was inserted into an access port in one of the bottom two sections of the multi-fuel reactor, as shown in Figure 6-12.

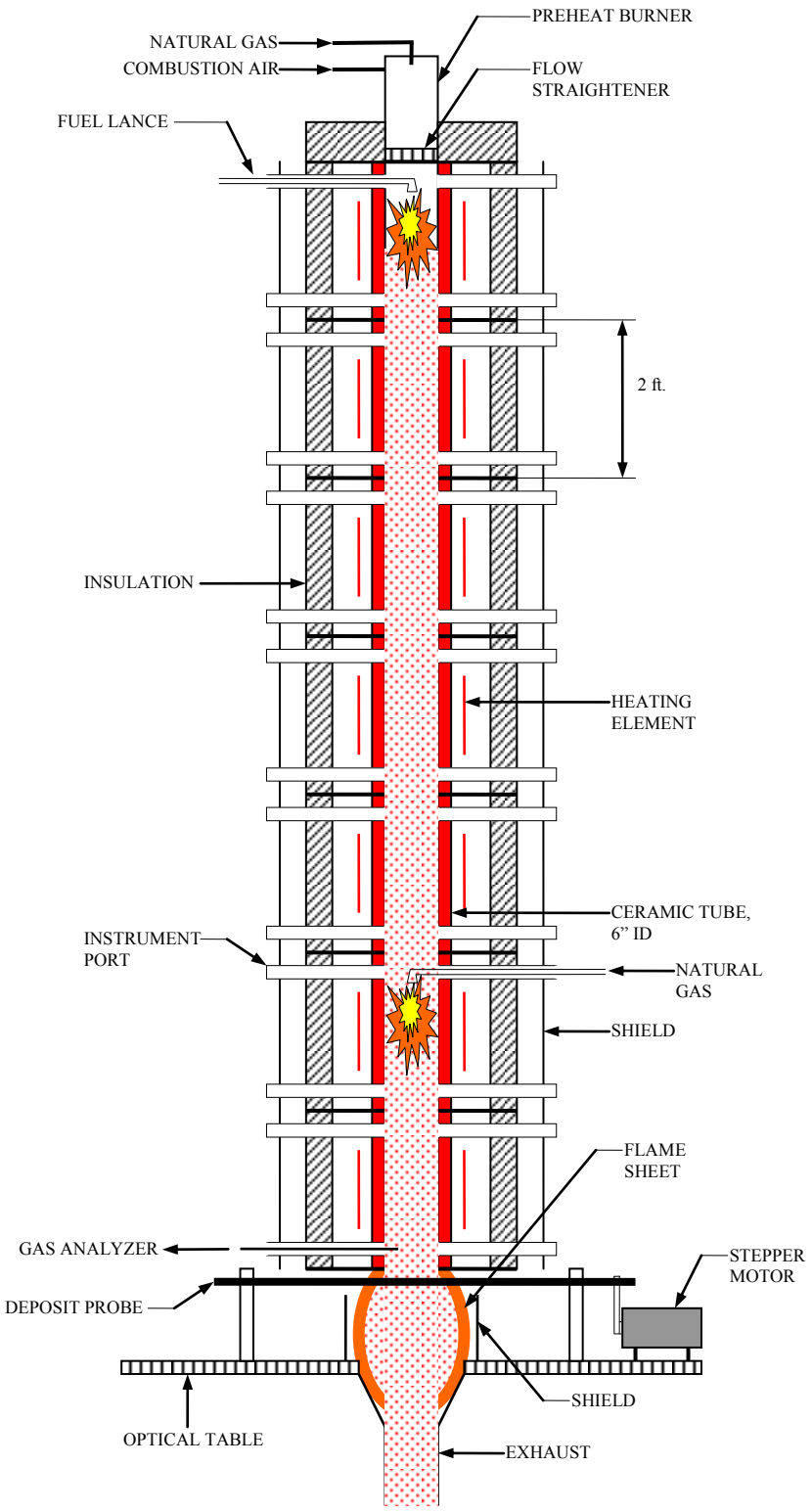

Figure 6-12. Schematic of multi-fuel reactor used in deposition experiments under reducing conditions.

With the addition of the secondary methane injection, an overall rich stoichiometry is created at the bottom of the MFR. Under these conditions, a flame "sheet" forms at the reactor outlet, where the room air mixes with the exhaust gases. The ash deposit forms on the deposition probe within this flame sheet under fuel-rich conditions. Sooting can be eliminated by premixing the secondary methane with air.

The flame sheet formed when burning coal under reducing conditions interferes with the optical path between the FTIR spectrometer and the ash deposit. Figure 6-13 compares the probe at the reactor outlet with and without the flame sheet.

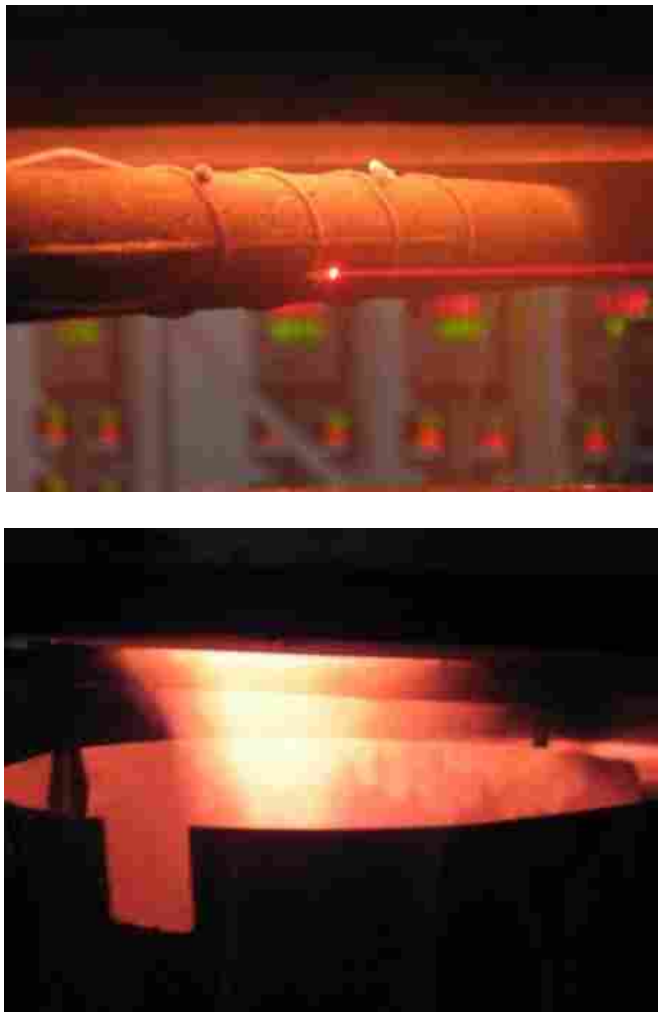

Figure 6-13. Comparison of the deposit probe without (top) and with (bottom) the particle cloud and flame sheet present when coal is burned under reducing conditions.

The emission from the flame sheet significantly affects the FTIR signal. In order to gain optical access through the flame sheet to the deposition probe, a snorkel was designed and manufactured. The snorkel consists of a thin steel tube which is placed through the flame sheet between the deposit probe and the first off-axis parabolic mirror in the optical path, as seen in Figure 6-14.

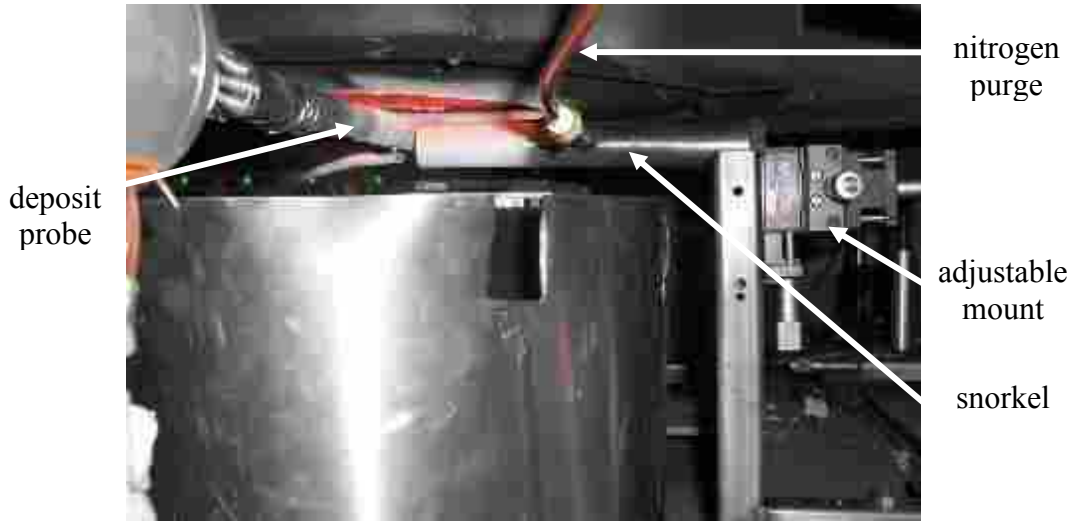

Figure 6-14. Experimental setup for measuring emittance of ash deposits that form in a reducing environment.

The snorkel is purged with nitrogen to ensure that the exhaust gases do not enter the tube and interfere with the FTIR signal. The inner diameter of the snorkel is greater than the diameter of the off-axis parabolic mirrors. In order to ensure that the snorkel does not physically interfere with the optical path, the snorkel is positioned such that the interferogram intensity is the same with and without the snorkel. An experiment was performed to ensure that the snorkel had no effect on the signal. The cleaned, painted probe was placed in the reactor outlet and allowed to reach a steady state temperature. The point of interrogation was aligned with a thermocouple to monitor the probe surface temperature. Spectra were collected with and without the snorkel. No coal was burned

during the experiment. Figure 6-15 shows the output signals from the FTIR with and without the snorkel and Figure 6-16 compares the corresponding spectral emittances. The use of the snorkel resulted in a slight increase in the surface temperature of the deposition probe because it affected the exhaust flow around the probe. This increase in temperature is reflected in the FTIR signal. This is the only apparent effect of the snorkel on the FTIR signal. The difference in spectral emittance is within the uncertainty of the spectral emittance of the painted probe.

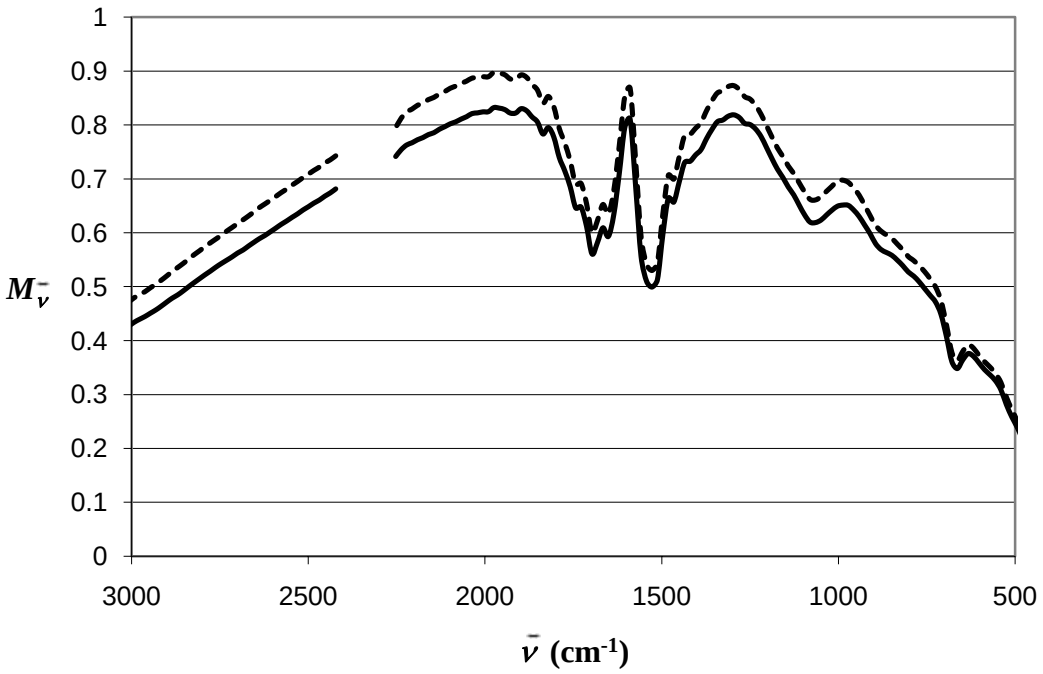

Figure 6-15. Comparison of signals output by the FTIR with (solid line) and without (dashed line) the snorkel.

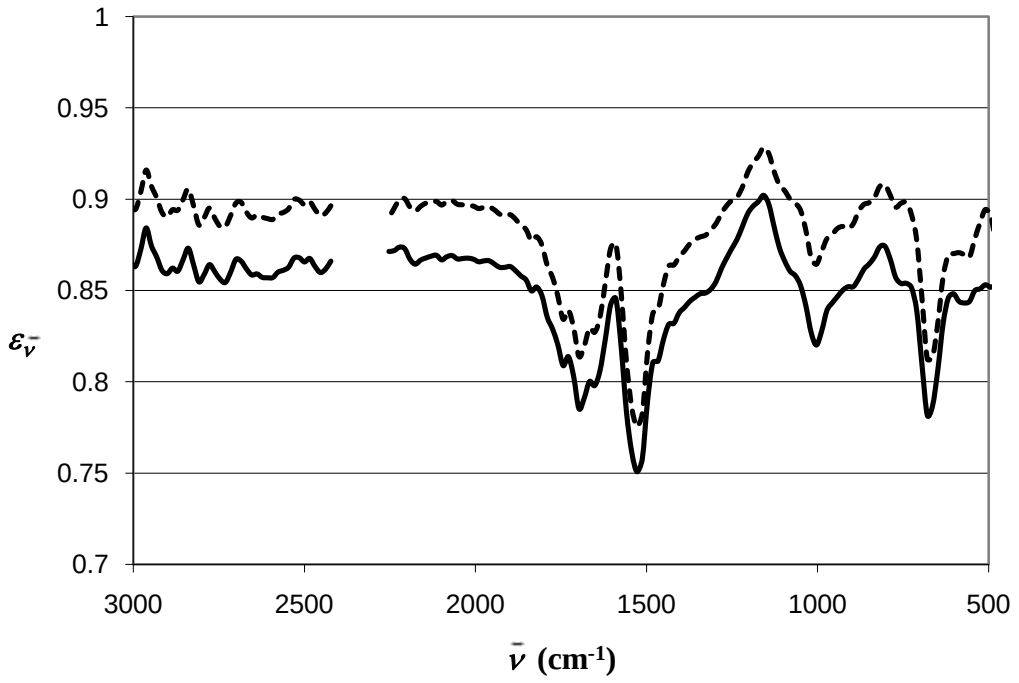

Figure 6-16. Comparison of spectral emittance calculated with (solid line) and without (dashed line) the snorkel.

The experimental procedure is similar to the procedure described in section 6.3 for oxidizing conditions. The instrument response function is found with the snorkel in place and the nitrogen purge on. The pulverized coal is injected into the reactor at a feed rate of 3.5 pounds per hour. A gas analyzer is used to monitor the oxygen level in the reactor exhaust. The flow rate of air in the preheat burner is adjusted until the oxygen level is less than 5%. The secondary methane is turned on and adjusted such that a flame sheet forms at the reactor outlet. The spectra are collected approximately every thirty minutes, as in the oxidizing experiments. The probe rotation is stopped. However, in order to maintain continuous reducing conditions, the coal injection is not stopped as in the oxidizing experiments. The nitrogen purged snorkel decreases the noise caused by the particle cloud. Figure 6-17 shows a comparison of high resolution signals from the FTIR

during a reducing experiment with and without the nitrogen purge in the snorkel. The data reduction procedure is the same as that for the oxidizing experiments.

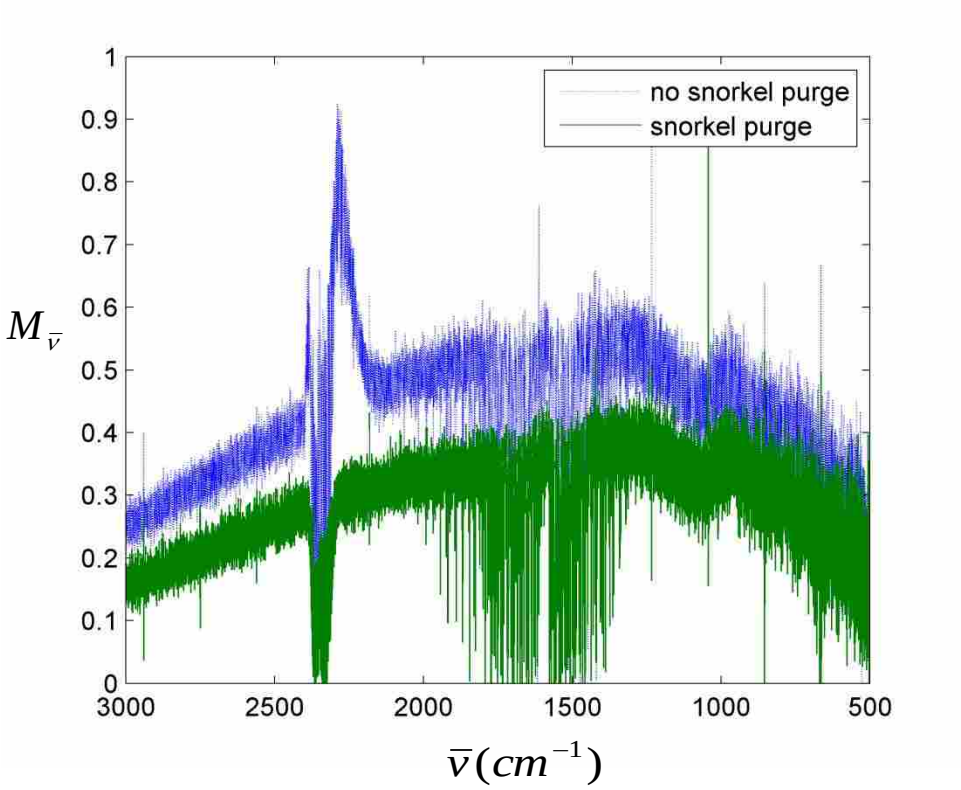

Figure 6-17. Comparison of signals from the FTIR from the probe seen through the snorkel with and without the nitrogen purge in the snorkel.

6.5 Data Reduction

A single ash deposition experiment may last from ten to sixteen hours, depending on the desired deposit thickness. This includes the time required to heat up and cool down the reactor. Typically, coal is burned for three to six hours. Once the experiment is complete, the data gathered is reduced and the spectral emittance of the ash layer is found. The Omnic software package is used to monitor the interferogram and to collect the spectra. The Omnic files are exported as comma delimited text files. The low

resolution files are imported into Microsoft Excel. For each spectra collected, the ash surface temperature is found using the technique described in section 4.5. The solver function in Excel is used to minimize the difference between the ratios of the spectral emissive powers found using the response function and those found using the Planck function. The spectral band used to infer the surface temperature consists of the wavenumbers between 2453 cm^{-1} and 2947 cm^{-1}. The spectral emittance at each time that a spectrum was collected is found using Eq. (4-3) and the instrument response function found at the beginning of the experiment. Finally, the total emittance is found from the methods developed in section 4.6.

6.6 Summary

The experimental procedure used to make *in situ* spectral emittance measurements of ash deposits was presented in this chapter. An optical path directs the radiative energy from the ash deposit into the FTIR. An alignment procedure was developed to ensure that the FTIR was correctly aimed at the desired point of interrogation on the deposit probe. The instrument response function is calculated by collecting spectra from the cleaned, painted deposit probe of known spectral emittance at a number of known temperatures. The effect of reflections from the deposit probe on the spectral emittance measurements was shown to be negligible. The importance of temporarily stopping the coal and the probe rotation while spectra are collected was investigated. For experiments performed under reducing conditions, a nitrogen-purged snorkel was employed to allow for optical access through the flame sheet present under these conditions. The effects of the snorkel on the emittance measurements were analyzed.

7 Results of Experiments

The *in situ* spectral emittances of two different coals under both oxidizing and reducing conditions are presented in this chapter. A number of total emittances are also presented along with the errors associated with these measurements.

7.1 Oxidizing Conditions: Bituminous Coal

The first coal analyzed under oxidizing conditions was Illinois #6 coal from the Crown III mine. This is a bituminous coal. Bituminous coal is the most plentiful type of coal in the United States and has a carbon content ranging from 45 to 86 percent carbon and a heat value of 10,500 to 15,500 BTUs per pound [31]. The ultimate and proximate analyses for the Illinois #6 coal are found in Table A-2. The equivalence ratio at the deposit probe for this experiment was 0.73. Figure 7-1 illustrates typical results from a single experiment.

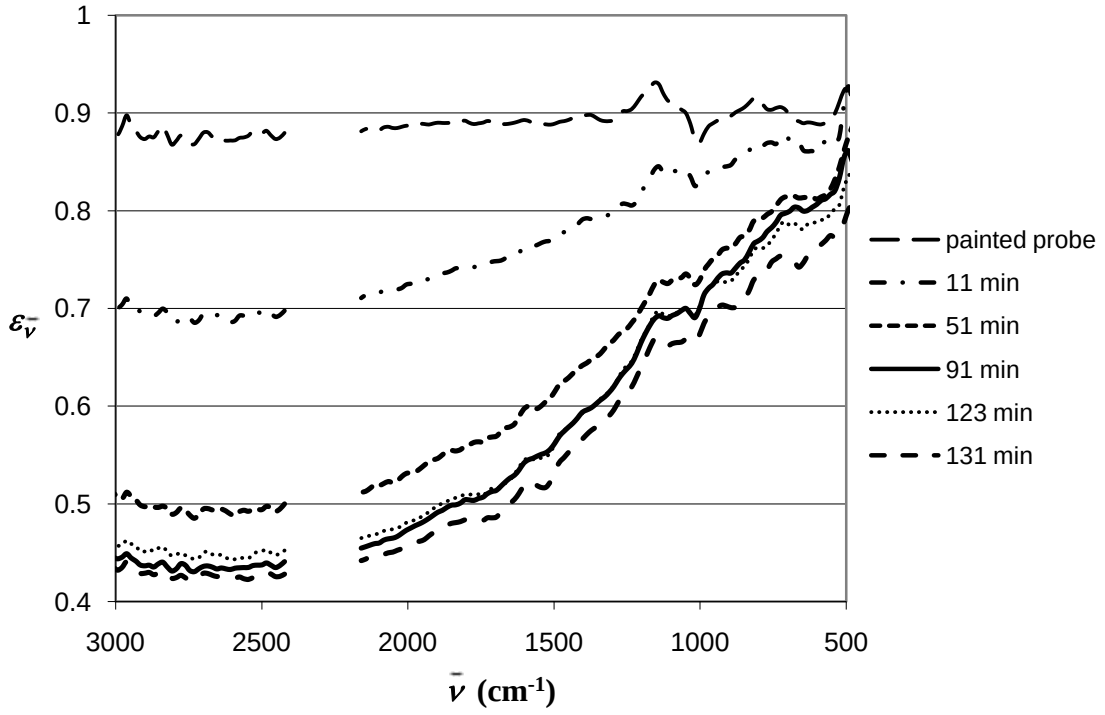

Figure 7-1. Spectral emittance of ash deposit as a function of the deposition time.

The spectral emittance before the coal is injected is simply equal to the spectral emittance of the clean, painted probe. After a short period of time, a thin layer of ash accumulates on the probe and the spectral emittance begins to change. At this point, the ash layer is not yet opaque and some emission from the probe is still detected by the FTIR spectrometer. As more coal is burned and the deposited layer gets thicker, the emission detected by the FTIR comes only from the surface of the deposited layer. Figure 7-2 shows the fluctuations in the spectral emittance of a deposit over time after it is has become opaque.

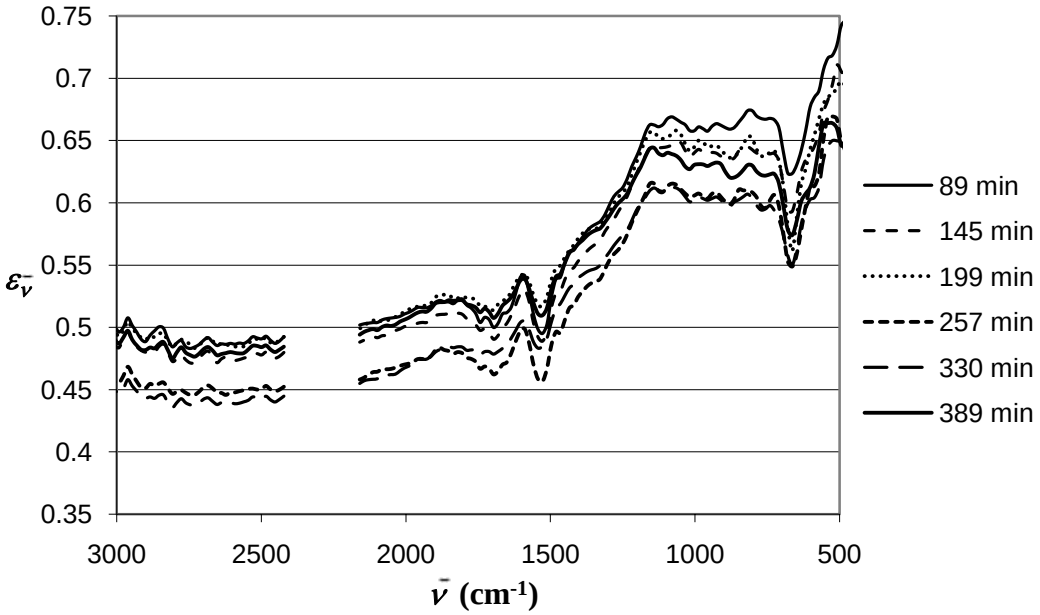

Figure 7-2. Spectral emittance of an opaque ash layer as a function of deposition time.

The emittance measurement experiment was repeated five times under the same conditions for the Illinois #6 coal. A total of 21 spectral emittance measurements were taken for opaque ash deposits. Figure 7-3 shows the average spectral emittance.

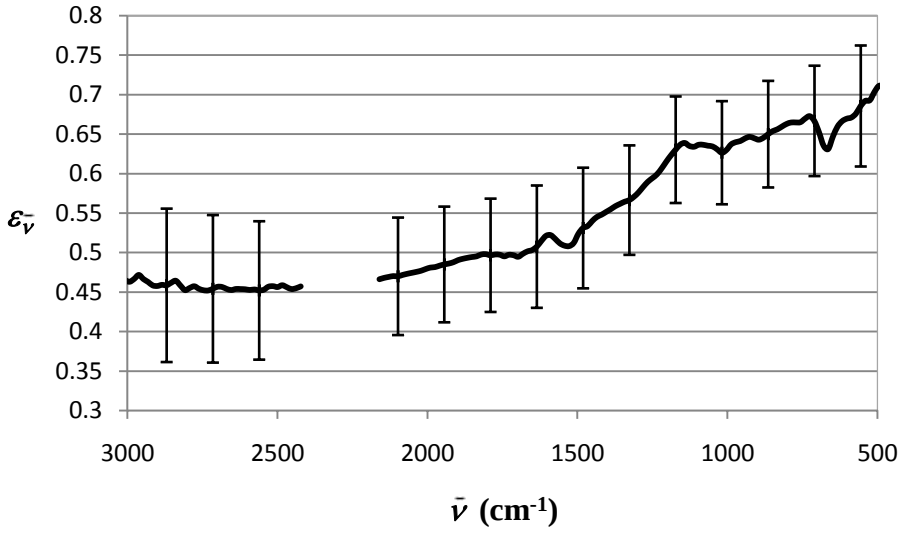

Figure 7-3. Spectral emittance of Illinois #6 (bituminous) coal under oxidizing conditions.

7.1.1 Uncertainty in the Spectral Emittance

The error bars in Figure 7-3 were obtained from an uncertainty analysis (propagation of error analysis) that is now described. The spectral emittance is found according to Eq. (4-21), which can be recast as the following equation.

$$\varepsilon_{\bar{\nu}} = \frac{ga_{\bar{\nu}} \cdot M_{\bar{\nu}} + gb_{\bar{\nu}}}{E_{b,\bar{\nu}}(T_S)} \tag{7-1}$$

The spectral emittance is a function of the two components of the instrument response function *ga* and *gb*, the FTIR signal *M*, and the deposit surface temperature T_s. The error in the spectral emittance measurement, $\Delta\varepsilon_{\bar{\nu}}$, is defined as follows.

$$\Delta\varepsilon_{\bar{\nu}} = \sqrt{\left(\frac{\partial\varepsilon_{\bar{\nu}}}{\partial ga_{\bar{\nu}}}\Delta ga_{\bar{\nu}}\right)^2 + \left(\frac{\partial\varepsilon_{\bar{\nu}}}{\partial gb_{\bar{\nu}}}\Delta gb_{\bar{\nu}}\right)^2 + \left(\frac{\partial\varepsilon_{\bar{\nu}}}{\partial M_{\bar{\nu}}}\Delta M_{\bar{\nu}}\right)^2 + \left(\frac{\partial\varepsilon_{\bar{\nu}}}{\partial T_S}\Delta T_S\right)^2} \tag{7-2}$$

It should be noted that this formula assumes that each error is independent of the other errors. This is most likely not the case. However, it provides a comparison between the magnitudes of the different error terms. The validity of this uncertainty analysis will be assessed by a comparison with the uncertainty in the measurements based on the standard deviation.

The *ga* term of the instrument response function is a function of the spectral emittance of the cleaned, painted probe shown in Figure 6-8. The error in the *ga* term is therefore defined as

$$\Delta ga_{\bar{\nu}} = \frac{\partial ga_{\bar{\nu}}}{\partial T_{P,\bar{\nu}}}\Delta T_{P,\bar{\nu}} \tag{7-3}$$

The spectral error in the painted probe temperature is also shown in Figure 6-8. The derivative in Eq. (7-3) can be approximated using a central difference scheme as follows.

$$\frac{\partial ga_{\bar{\nu}}}{\partial T_{P,\bar{\nu}}} \approx \frac{ga_{\bar{\nu}}(T_P + \Delta T_P) - ga_{\bar{\nu}}(T_P - \Delta T_P)}{2\Delta T_{P,\bar{\nu}}} \tag{7-4}$$

The error in the *ga* term can be approximated as

$$\Delta ga_{\bar{\nu}} = \frac{\partial ga_{\bar{\nu}}}{\partial T_{P,\bar{\nu}}} \Delta T_{P,\bar{\nu}} \approx \frac{ga_{\bar{\nu}}(T_P + \Delta T_P) - ga_{\bar{\nu}}(T_P - \Delta T_P)}{2} \tag{7-5}$$

The first term on the right side of Eq. (7-2) is approximated as

$$\frac{\partial \varepsilon_{\bar{\nu}}}{\partial ga_{\bar{\nu}}} \Delta ga_{\bar{\nu}} \approx \frac{M_{\bar{\nu}}}{E_{b,\bar{\nu}}(T_S)} \cdot \frac{ga_{\bar{\nu}}(T_P + \Delta T_P) - ga_{\bar{\nu}}(T_P - \Delta T_P)}{2} \tag{7-6}$$

Similarly, the second term on the right side of Eq. (7-2) can be expressed as

$$\frac{\partial \varepsilon_{\bar{\nu}}}{\partial gb_{\bar{\nu}}} \Delta gb_{\bar{\nu}} \approx \frac{1}{E_{b,\bar{\nu}}(T_S)} \cdot \frac{gb_{\bar{\nu}}(T_P + \Delta T_P) - gb_{\bar{\nu}}(T_P - \Delta T_P)}{2} \tag{7-7}$$

The third term can be differentiated analytically and is

$$\frac{\partial \varepsilon_{\bar{\nu}}}{\partial M_{\bar{\nu}}} \Delta M_{\bar{\nu}} = \frac{ga_{\bar{\nu}}}{E_{b,\bar{\nu}}(T_S)} \Delta M_{\bar{\nu}} \tag{7-8}$$

The error in the FTIR signal, $\Delta M_{\bar{\nu}}$, is found by multiplying the standard deviation in the signal at each wavenumber by the *t*-statistic corresponding to the number of degrees of freedom (the number of signals collected minus one). $\Delta M_{\bar{\nu}}$ was found for each day that the coal was burned and these were averaged to find the total $\Delta M_{\bar{\nu}}$. Finally, the surface temperature term in Eq. (7-2) was calculated by using the Planck function for the blackbody emissive power according to Eq. (4-2) and differentiating with respect to the surface temperature. The result is shown in Eq. (7-9).

$$\frac{\partial \varepsilon_{\bar{\nu}}}{\partial T_S}\Delta T_S = \frac{(ga_{\bar{\nu}} \cdot M_{\bar{\nu}} + gb_{\bar{\nu}})\alpha_2 \exp\left(\frac{\alpha_2 \bar{\nu}}{T_S}\right)}{\bar{\nu}^2 T_S^2 \pi \alpha_1}\Delta T_S \tag{7-9}$$

The error in the surface temperature measurement, ΔT_S, is a function of the FTIR signal and the instrument response function and can, therefore, be calculated as follows.

$$\Delta T_S = \sum_{i=1}^{n}\left[\sqrt{\left(\frac{\partial T_S}{\partial M_{\bar{\nu},i}}\Delta M_{\bar{\nu},i}\right)^2 + \left(\frac{\partial T_S}{\partial ga_{\bar{\nu},i}}\Delta ga_{\bar{\nu},i}\right)^2 + \left(\frac{\partial T_S}{\partial gb_{\bar{\nu},i}}\Delta gb_{\bar{\nu},i}\right)^2}\right] \tag{7-10}$$

The terms are summed over the gray spectral band used to calculate the surface temperature. The terms on the right side of Eq. (7-10) can be approximated using a central difference scheme as shown in Eqs. (7-11) through (7-13).

$$\frac{\partial T_S}{\partial M_{\bar{\nu}}}\Delta M_{\bar{\nu}} \approx \frac{T_S(M_{\bar{\nu}} + \Delta M_{\bar{\nu}}) - T_S(M_{\bar{\nu}} + \Delta M_{\bar{\nu}})}{2} \tag{7-11}$$

$$\frac{\partial T_S}{\partial M_{\bar{\nu}}}\Delta ga_{\bar{\nu}} \approx \frac{T_S(ga_{\bar{\nu}} + \Delta ga_{\bar{\nu}}) - T_S(ga_{\bar{\nu}} + \Delta ga_{\bar{\nu}})}{2} \tag{7-12}$$

$$\frac{\partial T_S}{\partial M_{\bar{\nu}}}\Delta gb_{\bar{\nu}} \approx \frac{T_S(gb_{\bar{\nu}} + \Delta gb_{\bar{\nu}}) - T_S(gb_{\bar{\nu}} + \Delta gb_{\bar{\nu}})}{2} \tag{7-13}$$

The error contributions from each measurement to the total error are shown in Figure 7-4 though Figure 7-7. Each term contributes a relatively equal amount of error except for the error in the *gb* term of the instrument response function, which contributes little error.

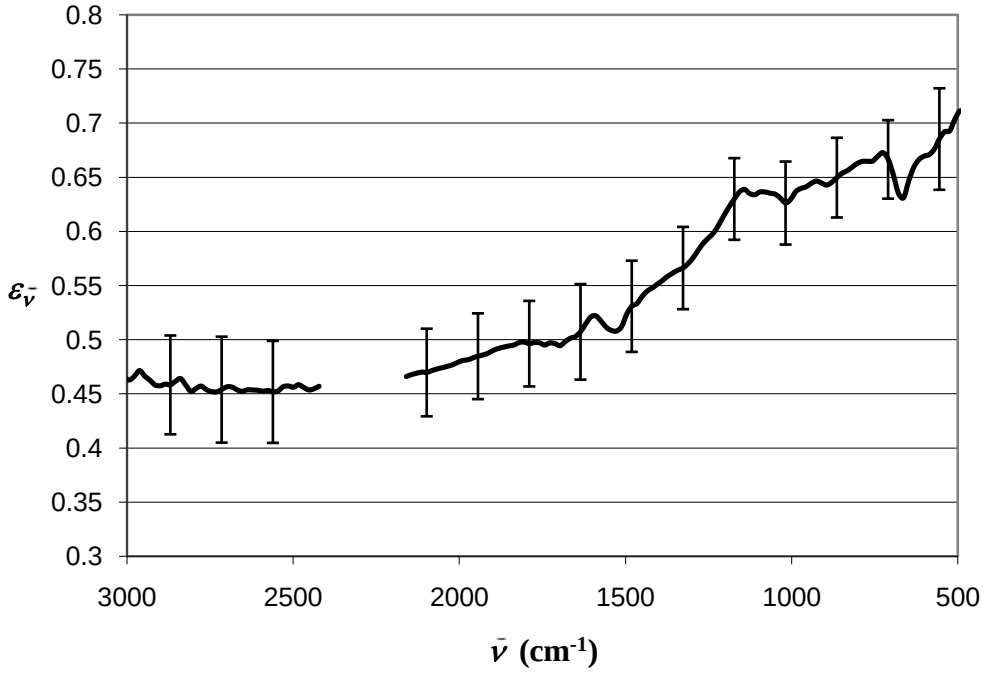

Figure 7-4. Error in spectral emittance due to the error in the *ga* term of the response function.

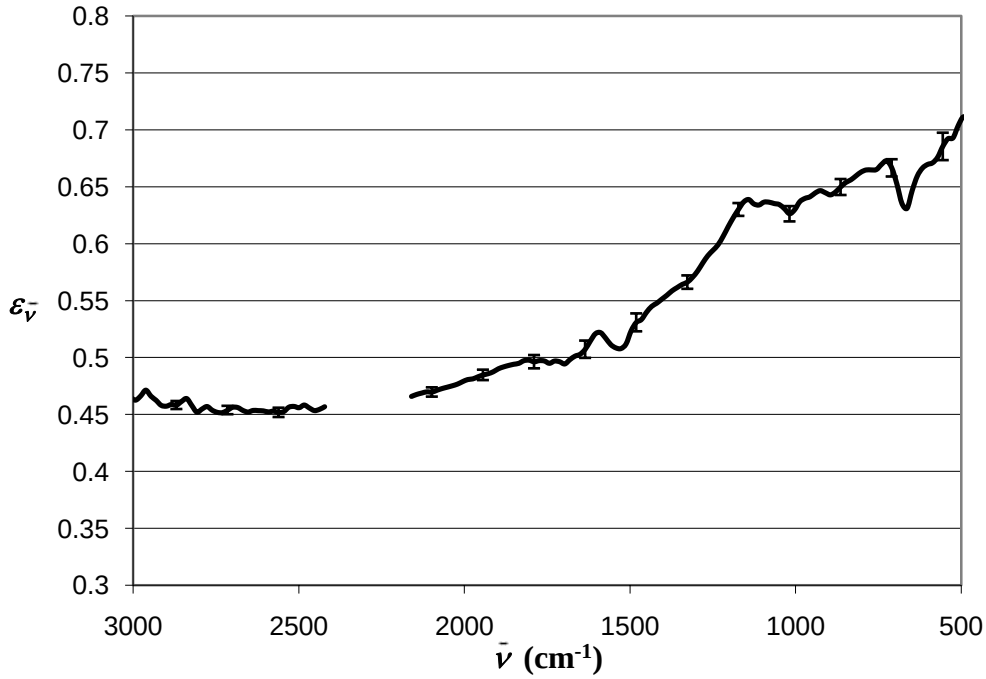

Figure 7-5. Error in spectral emittance due to the error in the *gb* term of the response function.

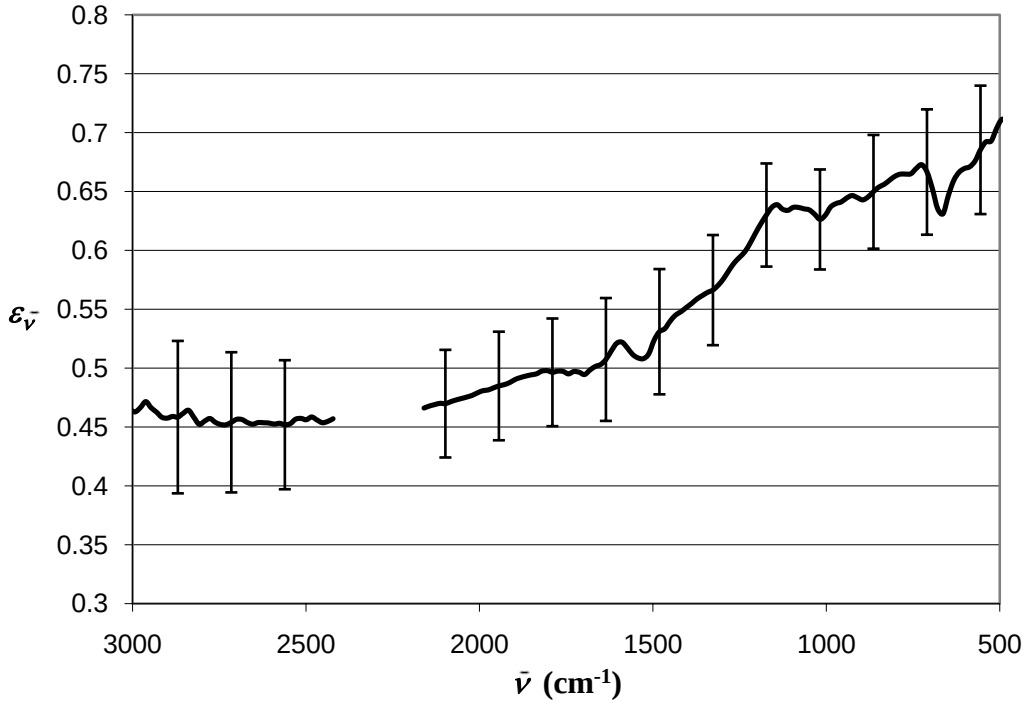

Figure 7-6. Error in spectral emittance due to the error in the FTIR signal, *M*.

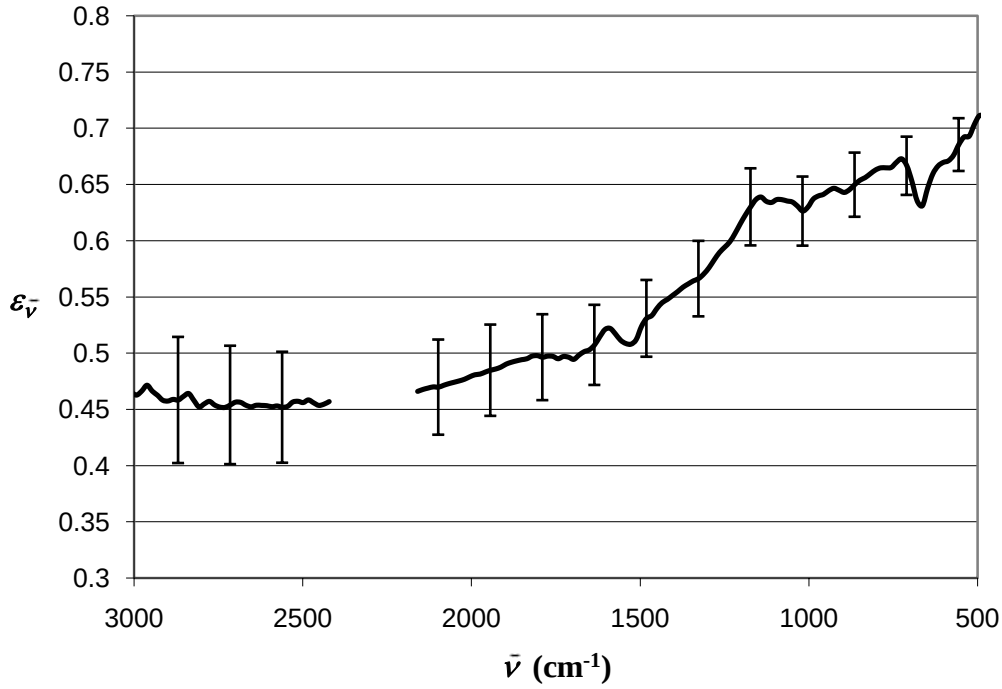

Figure 7-7. Error in spectral emittance due to the error in the surface temperature measurement.

In order to verify the preceding uncertainty analysis, the error bars obtained from this analysis are compared to the error bars found simply by looking at the spread of the spectral emittance data. Figure 7-8 shows that there is good agreement between both methods of quantifying the error in the spectral emittance calculation.

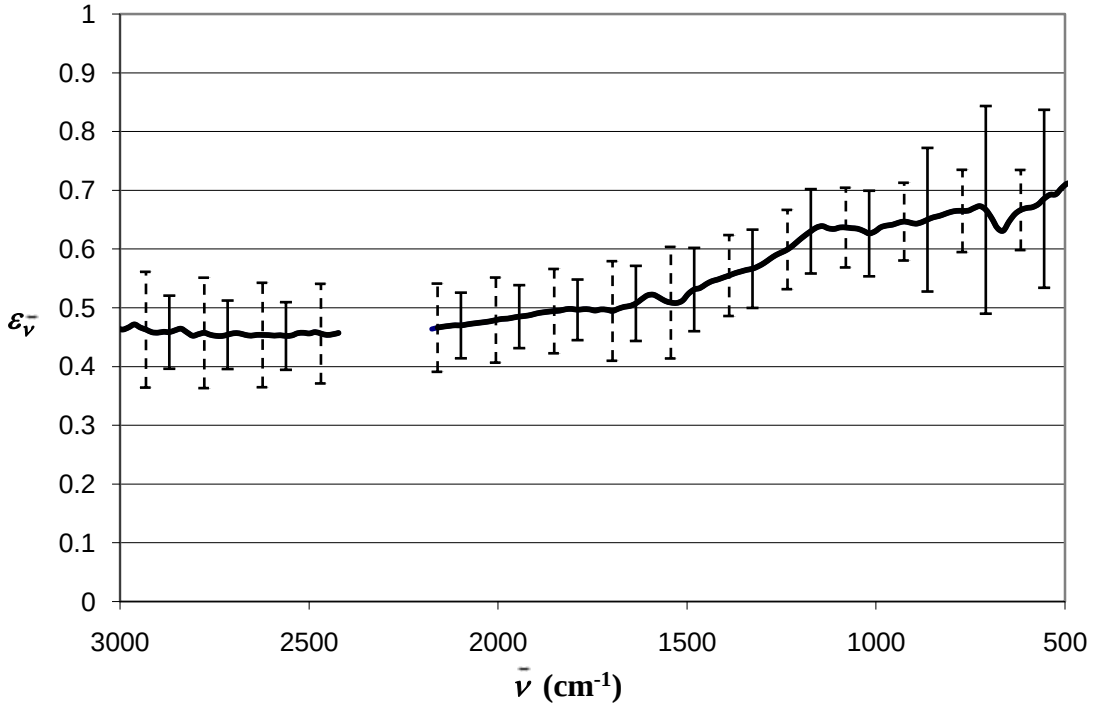

Figure 7-8. Comparison of the error calculated using a standard uncertainty analysis (dashed bars) and those calculated from the standard deviation of the data set (solid bars).

7.1.2 Total Emittance

The total emittance is defined according to Eq. (4-32). However, in order to use Eq. (4-32), the spectral emittance must be known over all wavelengths. Because of limitations of the detector in the FTIR, the spectral emittance is only known with confidence over the band from 500 to 3000 cm^{-1}, or 3.3 to 20 μm. The total emittance,

therefore, cannot be calculated precisely. Upper and lower limits on the total emittance can be calculated by assuming the spectral emittance outside of the known spectral band to be 1 and 0, respectively. Similarly, an estimate of the total emittance can be made by assuming that the values at the edges of the known spectral band remain constant in the unknown spectral regions. Figure 7-9 shows these assumed spectral emittances for the Illinois #6 coal.

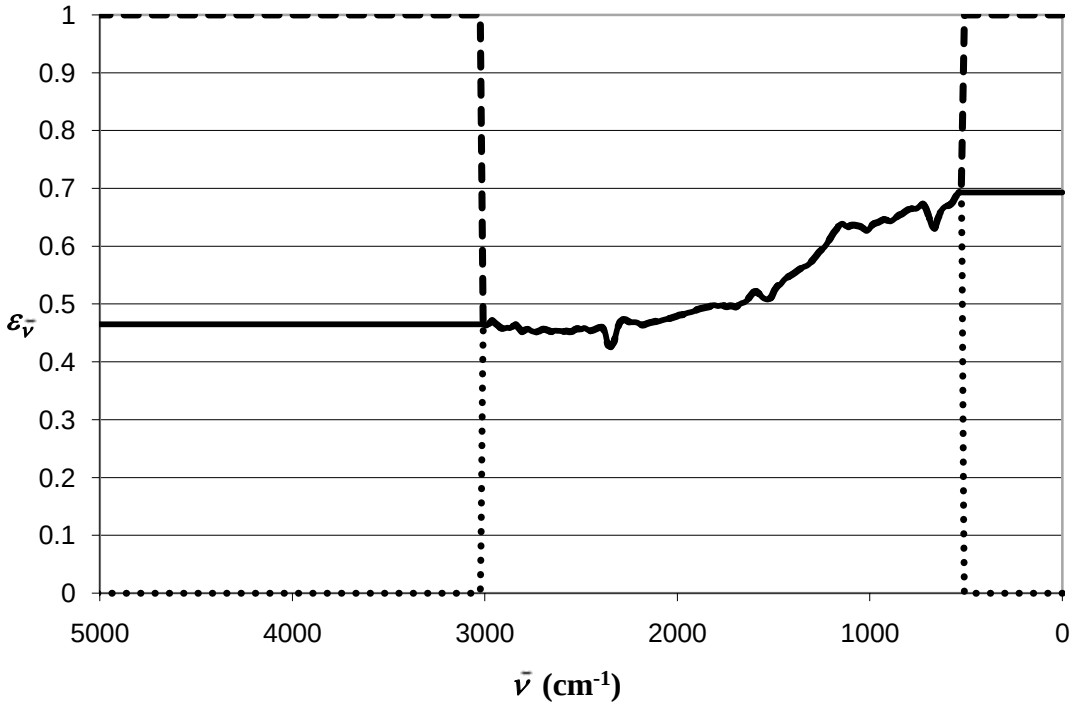

Figure 7-9. Assumed spectral emittances of the ash layer beyond the limits of the detector. The dashed line represents the upper limit, the dotted line represents the lower limit, and the solid line assumes the emittance at the edges remain constant.

If the profiles shown if Figure 7-9 are used with the equations in section 4.6, the total emittances can be calculated. Figure 7-10 shows the total emittances of the Illinois #6 coal as functions of temperature.

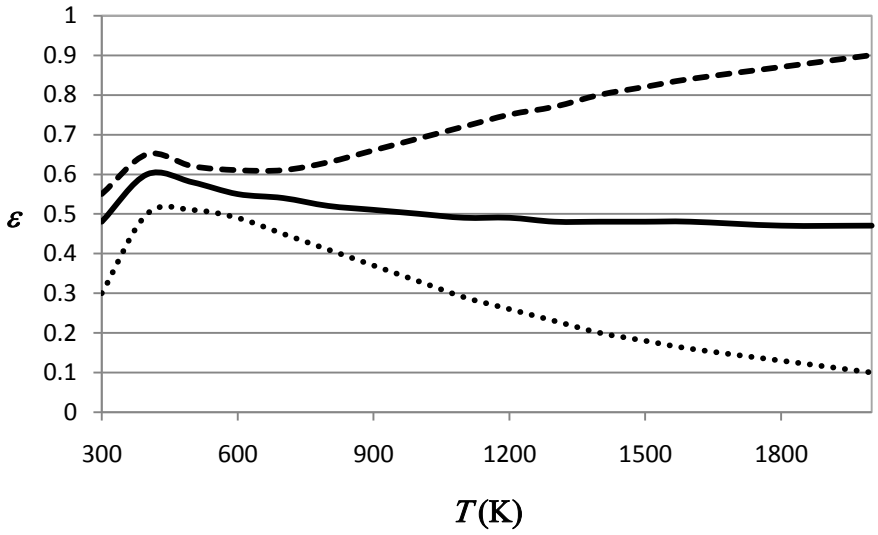

Figure 7-10. The total emittance (solid line) of the Illinois #6 coal in oxidizing conditions. The dashed line represents the upper limit while the dotted line represents the lower limit.

Another way to approximate the total emittance, based solely on the known spectral emittance, is to define a total band emittance ε_B as

$$\varepsilon_B \equiv \frac{\int_{\lambda_1}^{\lambda_2} \varepsilon_\lambda(\lambda,T) E_{\lambda,b}(\lambda,T) d\lambda}{\int_{\lambda_1}^{\lambda_2} E_{\lambda,b}(\lambda,T) d\lambda} \tag{7-14}$$

Equation (7-14) is comparable to Eq. (4-32) except it is defined over a specified band instead of over the entire spectrum. The fractional function defined in Eq. (4-34) can still be used to find the total band emittance by multiplying the top and bottom of Eq. (7-14) by E_b as follows

$$\varepsilon_B = \frac{\int_{\lambda_1}^{\lambda_2} \varepsilon_\lambda(\lambda,T) E_{\lambda,b}(\lambda,T) d\lambda}{\int_{\lambda_1}^{\lambda_2} E_{\lambda,b}(\lambda,T) d\lambda} \cdot \frac{\int_0^{\infty} E_{\lambda,b}(\lambda,T) d\lambda}{\int_0^{\infty} E_{\lambda,b}(\lambda,T) d\lambda} \tag{7-15}$$

This equation can be rearranged to get

$$\varepsilon_B = \frac{\int_{\lambda_1}^{\lambda_2} \varepsilon_\lambda(\lambda,T) E_{\lambda,b}(\lambda,T) d\lambda}{\int_0^\infty E_{\lambda,b}(\lambda,T) d\lambda} \cdot \frac{\int_0^\infty E_{\lambda,b}(\lambda,T) d\lambda}{\int_{\lambda_1}^{\lambda_2} E_{\lambda,b}(\lambda,T) d\lambda} \tag{7-16}$$

Equation (7-16) can be approximated using the fractional function as

$$\varepsilon_B \approx \frac{\sum_{i=1}^{n} \varepsilon_{AVG(i,i-1)} \left[F(\lambda_i T) - F(\lambda_{i-1} T) \right]}{F(\lambda_2 T) - F(\lambda_1 T)} \tag{7-17}$$

Using Eq. (7-17) and the equations presented in section 4.6, the total band emittance for the Illinois#6 were calculated and plotted with the measurement error. The results are shown in Figure 7-11.

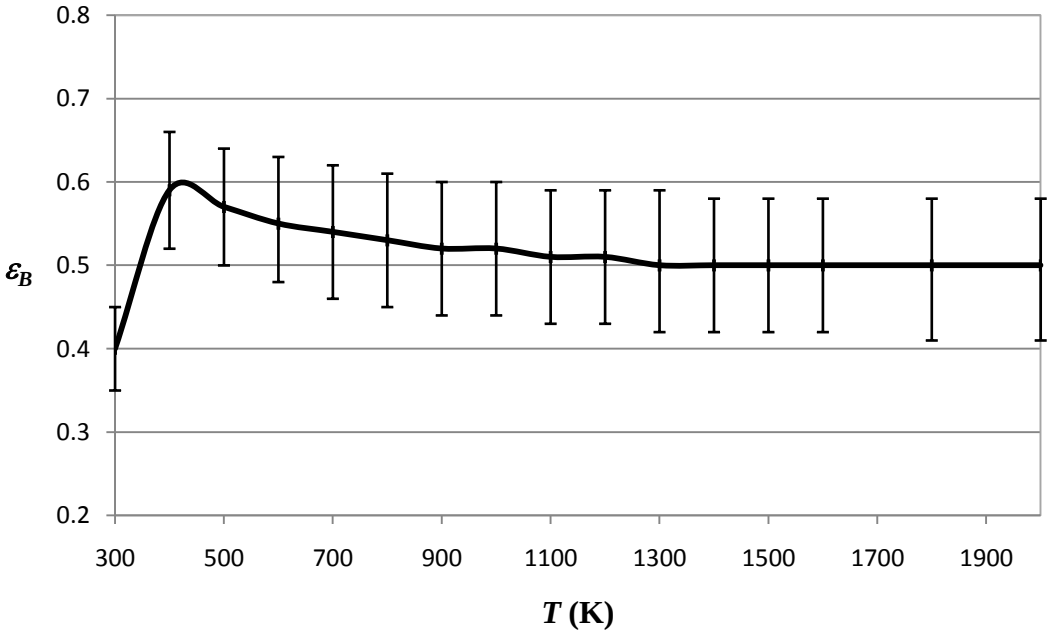

Figure 7-11. The total band emittance of the Illinois #6 coal in oxidizing conditions.

7.2 Oxidizing Conditions: Subbituminous Coal

The second coal analyzed under oxidizing conditions was Wyoming coal from the Corederro mine. This is a subbituminous coal. Subbituminous coals have a carbon content ranging from 35 to 45 percent carbon and a heat value of 8,300 to 13,000 BTUs per pound and are generally cleaner burning than bituminous coals because of their lower sulfur content. The ultimate and proximate analyses for this coal are found in Table A-1. The equivalence ratio for this experiment was 0.71. Figure 7-12 shows typical spectral emittance measurements over the course of an experiment. The results over the course of a single experiment are comparable to those of the bituminous coal found in Figure 7-1.

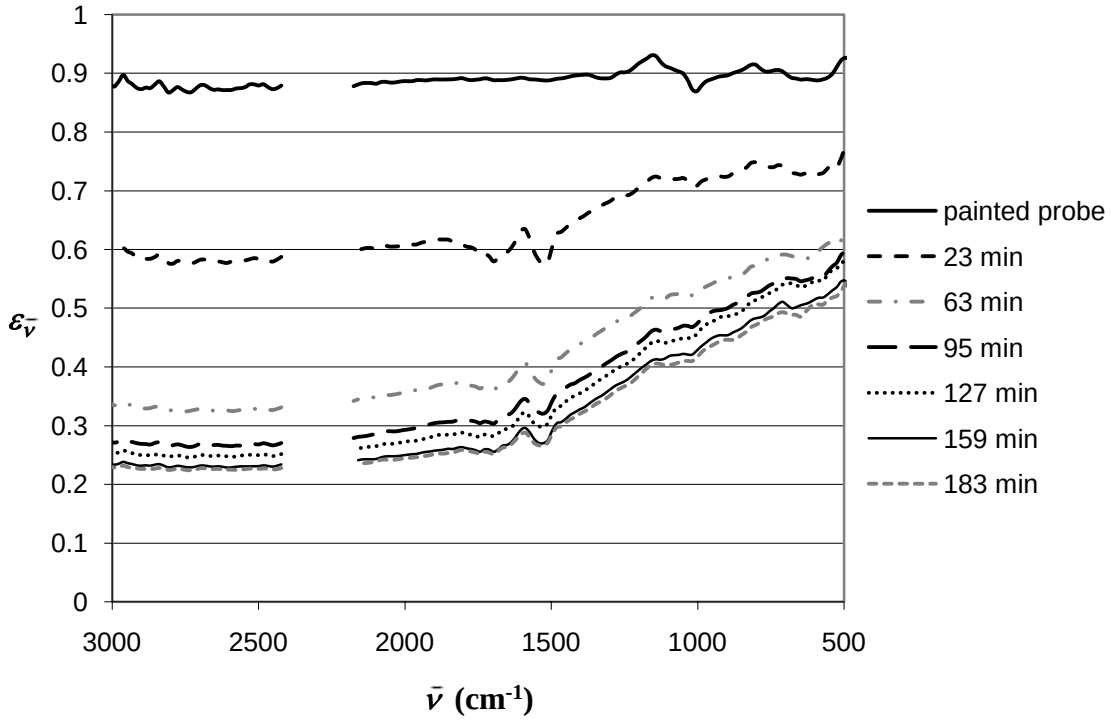

Figure 7-12. Spectral emittance of ash deposit as a function of the deposition time.

The experiment was repeated three times under the same conditions for the Wyoming coal. A total of twelve spectral emittance measurements were taken for opaque ash deposits. Figure 7-13 shows the average spectral emittance with the corresponding uncertainty. The trends of the spectral emittance of the subbituminous coal are similar to those observed in the bituminous coal, but the spectral emittance of the subbituminous coal is lower than that of the bituminous coal.

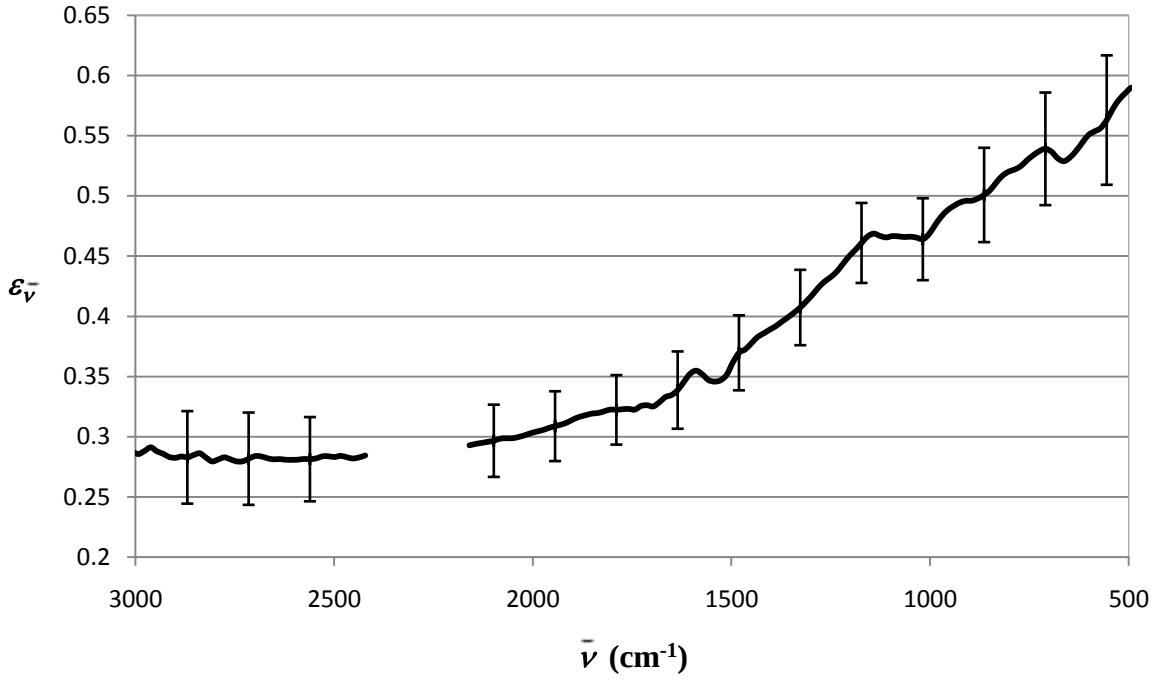

Figure 7-13. Spectral emittance of Wyoming (subbituminous) coal under oxidizing conditions.

The total emittance estimates were found using the same approximations used for the Illinois #6 coal and are shown in Figure 7-14. The total band emittance is shown in Figure 7-16.

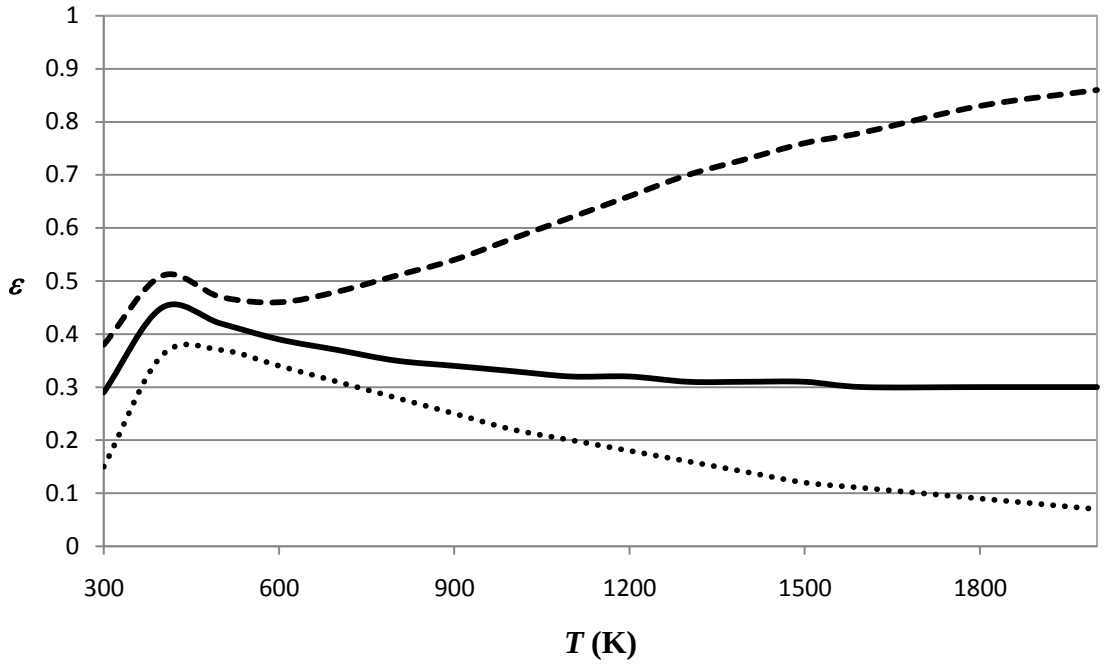

Figure 7-14. The total emittance (solid line) of the Wyoming coal in oxidizing conditions. The dashed line represents the upper limit while the dotted line represents the lower limit.

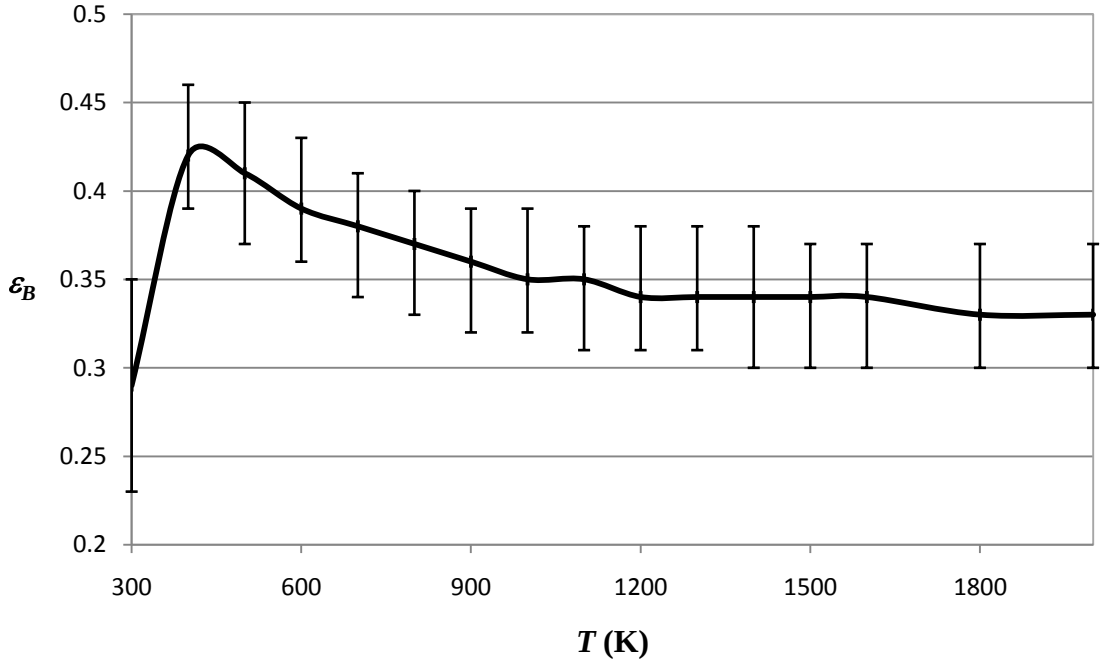

Figure 7-15. The total band emittance of the Wyoming coal in oxidizing conditions.

7.3 Summary of Oxidizing Experiments

The spectral and total emittances for bituminous and subbituminous opaque coal ash deposits formed under oxidizing conditions were calculated. Once the deposit becomes opaque, any change in spectral emittance is due to the inevitable variation in small scale structure of the particulate deposit. A standard uncertainty analysis was performed to find the uncertainty in the spectral emittance measurements. Upper and lower limits on the total emittances of the deposits were found for both types of coal. The spectral emittances of both coals showed similar trends where there was a decrease in emittance at low wavenumbers and a leveling off at higher wavenumbers. The emittance of the subbituminous coal was lower than that of the bituminous coal.

7.4 Reducing Conditions

In situ emittance measurements were also made under reducing conditions. The experimental setup and procedures used to produce oxidizing conditions were modified to maintain a fuel-rich environment. The reducing environment emulates the conditions under which ash deposits are formed in coal gasifiers. Maintaining consistent, repeatable reducing conditions was a difficult problem and resulted in a much greater uncertainty in the measurements made. Accordingly, the measurements made under reducing conditions were made with significantly less confidence than those made under oxidizing conditions.

7.4.1 Results of Reducing Experiments

The *in situ* spectral emittances of two different coals under reducing conditions are now presented. The corresponding total emittances are also presented. Figure 7-16

shows the spectral emittance of the Illinois #6 coal deposit along with the measurements error. A total of six spectral emittance measurements were taken for opaque ash deposits. The equivalence ratio for these experiments was 2.33.

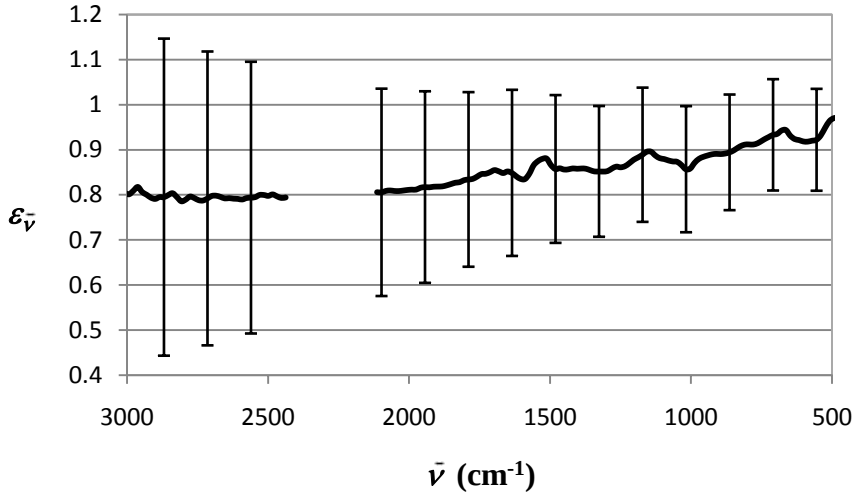

Figure 7-16. Spectral emittance of Illinois #6 (bituminous) coal under reducing conditions.

Figure 7-17 shows the total emittances as a function of temperature and Figure 7-18 shows the total band emittance.

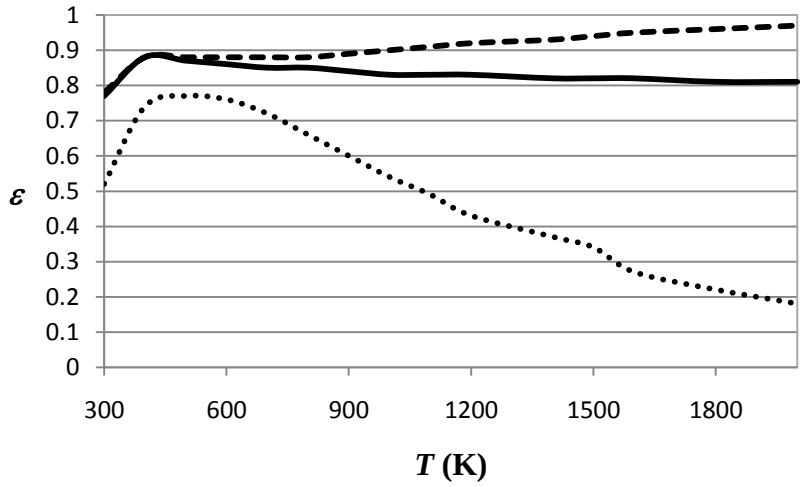

Figure 7-17. The total emittance (solid line) of the Illinois #6 coal in reducing conditions. The dashed line represents the upper limit while the dotted line represents the lower limit.

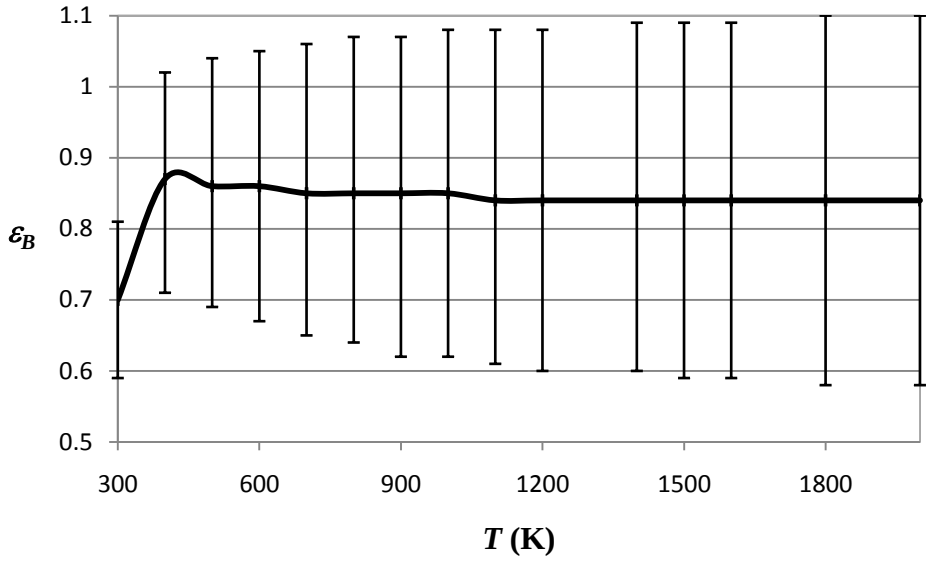

Figure 7-18. The total band emittance of the Illinois #6 coal under reducing conditions.

Figure 7-19 shows the spectral emittance of the Wyoming coal deposit and the uncertainty in the measurements. A total of 11 spectral emittance measurements were taken for opaque ash deposits. The equivalence ratio was 3.10.

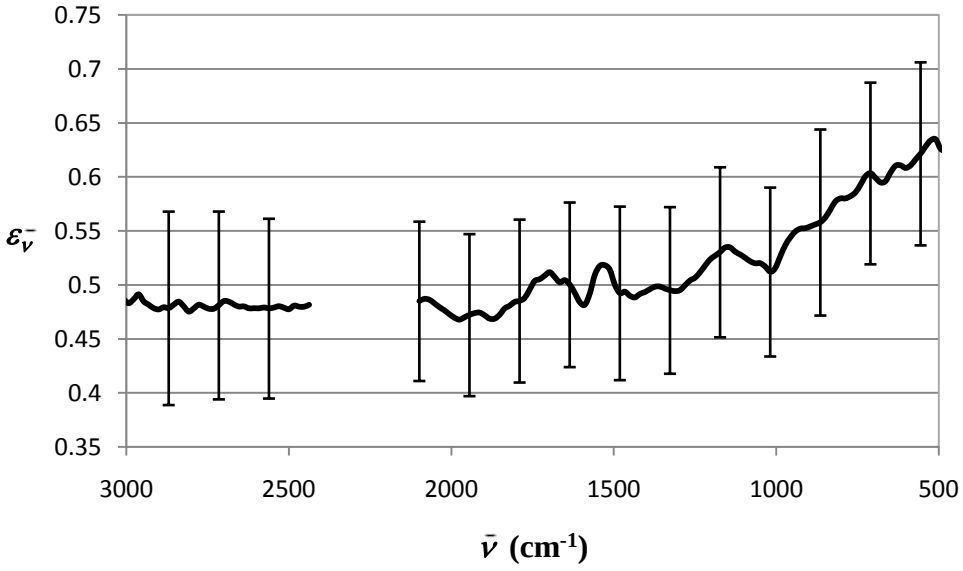

Figure 7-19. Spectral emittance of Wyoming (subbituminous) coal under reducing conditions.

Figure 7-20 shows the total emittance estimates as a function of temperature and Figure 7-21 shows the total band emittance.

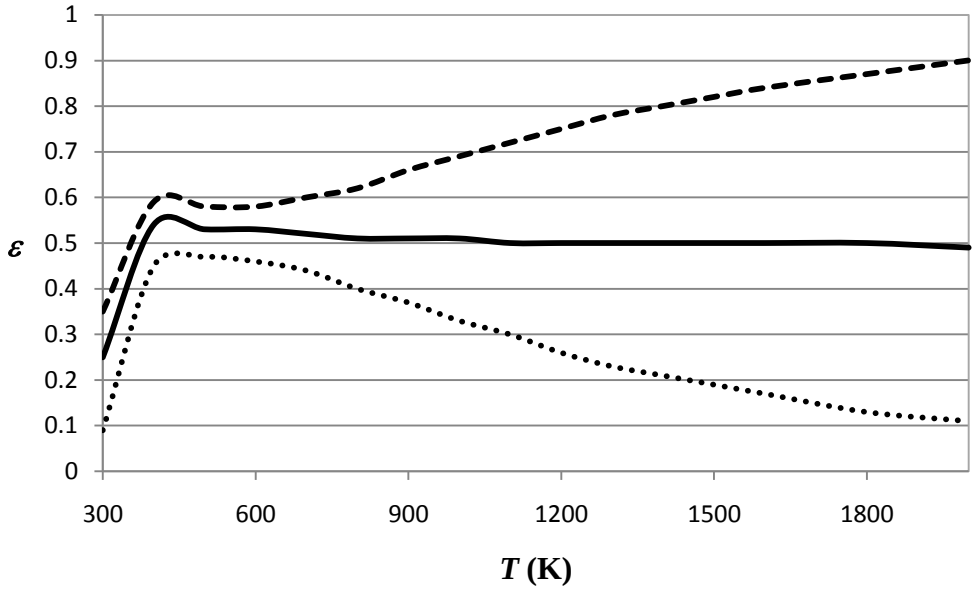

Figure 7-20. The total band emittance (solid line) of the Wyoming coal in reducing conditions. The dashed line represents the upper limit while the dotted line represents the lower limit.

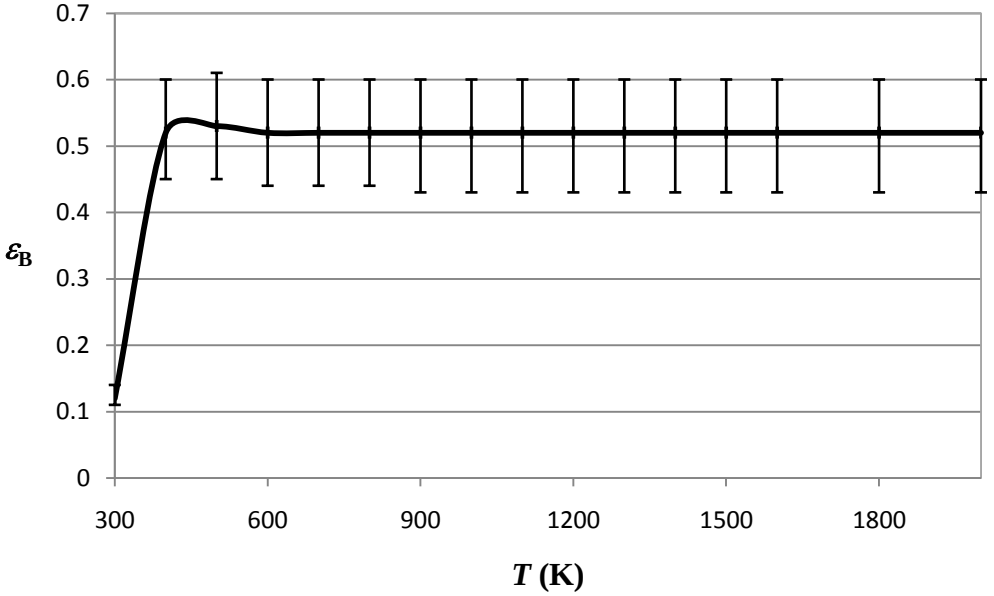

Figure 7-21. The total band emittance of the Wyoming coal under reducing conditions.

7.5 Summary of Reducing Experiments

The spectral and total emittances for bituminous and subbituminous opaque coal ash deposits formed under reducing conditions were calculated. A nitrogen-purged snorkel was employed to allow for optical access through the flame sheet present under reducing conditions. The uncertainty in the spectral emittance measurements was computed. An estimate of the total emittance was calculated in addition to upper and lower limits on the total emittance for both types of coal. A total band emittance was defined and calculated with the corresponding measurement error.

8 Discussion and Summary

8.1 Discussion of Oxidizing Experiments

The spectral emittance of both the bituminous and subbituminous coals exhibited the same trends over the course of a deposition experiment. As the deposit thickness increased, the change in the spectral emittance decreased. Radiative properties of an object generally depend only on a very thin surface layer [16]. Therefore, when the ash layer becomes opaque, the spectral emittance of the deposit reaches a more or less steady profile. Fluctuations in the spectral emittance beyond this point are most likely a result of the continuously changing small scale structure of the particulate deposit and noise in the measurements.

The spectral emittance of both types of coal is relatively flat at high wavenumbers (from 3000 to 2000 cm^{-1}). This approximately gray band verifies the assumption made in section 4.5 required to make accurate surface temperature measurements. From about 2000 to 1200 cm^{-1} there is a sharp increase in the spectral emittance of both types of coal, after which there is another relatively gray region from 1200 to 800 cm^{-1}. There follows another sharp increase in the spectral emittance through 500 cm^{-1} (the lower limit of the DTGS detector). Both types of coals exhibit these patterns in the spectral emittance, although they are more pronounced in that of the bituminous coal. This may be a result of

the thinner deposits formed from the subbituminous coal. It is possible that, in some cases, the deposits were not thick enough to reach a fully opaque state. If that is the case, the finer features of the spectral emittance would not be as apparent. This may have also been the case on a number of the bituminous coal experiments, resulting in an average spectral emittance that appeared more "smoothed" than the actual emittance profile. In all cases, the subbituminous coal had lower spectral emittance values than the bituminous coal.

The total emittance of the ash deposits could not be calculated exactly because the spectral emittance was not known over the entire spectrum. An estimate of the total emittance was made by assuming that the emittance at the edges of the known spectral band remained constant over the rest of the spectrum. Additionally, a total band emittance was defined. There was an average difference of 3.3% between the estimated total emittance and the defined band emittance over the temperature range of 400 K to 2000 K. Both total emittance approximations showed little dependence on temperature. The total band emittance of both coals under oxidizing conditions decreased by about 0.1 over a temperature range from 400 K to 2000 K.

8.2 Discussion of Reducing Experiments

The spectral emittances of deposits formed under reducing conditions displayed the same temporal behavior as those formed under oxidizing conditions. That is, the spectral emittance decreased with time until the deposit was opaque, after which all changes were due only to the changing structure of the outer layer of the deposit. The spectral emittance of the deposits formed under reducing conditions had similar spectral

trends as those formed under oxidizing conditions. Specifically, the emittance was essentially gray from 3000 to 1800 cm^{-1}, followed by an increase in emittance to 500 cm^{-1}. However, the finer scale features found in the oxidizing deposit emittances were absent in those of the reducing deposits. For both bituminous and subbituminous coals, the spectral emittances formed under reducing conditions were higher than those formed under oxidizing conditions. Under reducing conditions, there was an average difference of 2.3% between the total emittance estimate and the total band emittance over a temperature range from 400 K to 2000 K. Over this same temperature range, the approximated total emittances of both coals remained essentially constant.

8.2.1 Limitations of the Reducing Experiments

The spectral emittance calculations made under reducing conditions appear to be consistent and repeatable. However, the effect of using the nitrogen-purged snorkel and leaving the coal burning throughout the experiment raise questions about the amount of control that was maintained during the experiments. In order to assess the experimental method used under reducing conditions, the same method was used under oxidizing conditions and compared to the results previously attained. The nitrogen-purged snorkel was used when the spectra were collected. A comparison of the spectral emittance measurements found using this method and the method described in Chapter 7 is shown in Figure 8-1.

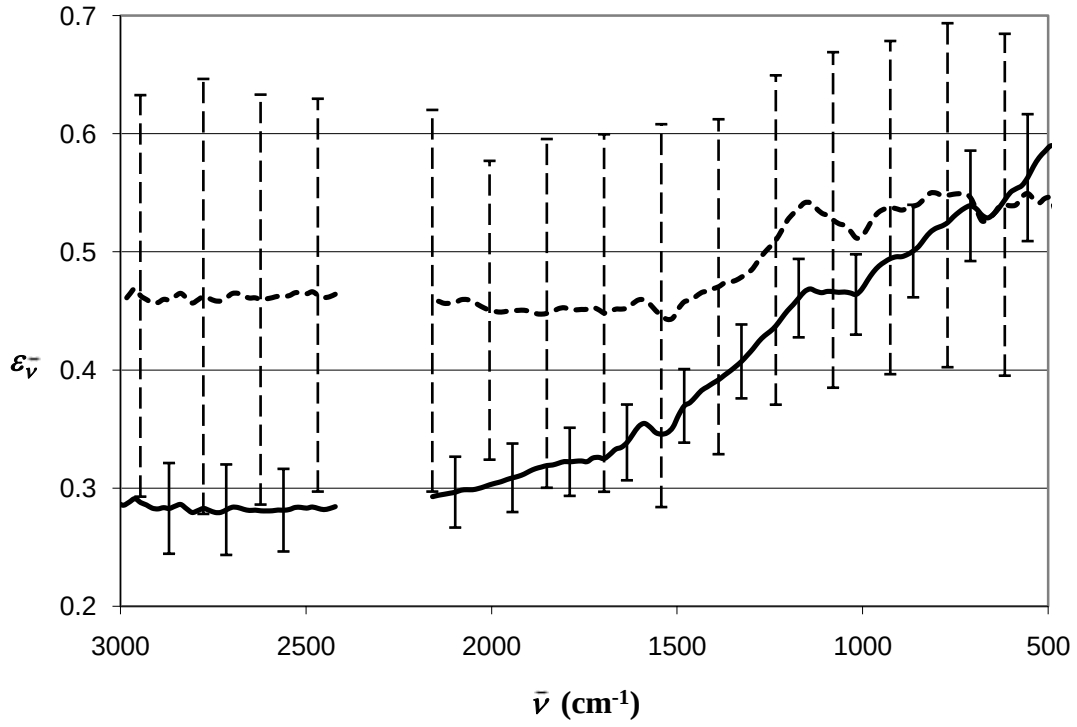

Figure 8-1. Comparison of the spectral emittance found for the same coal under oxidizing conditions with (dashed line) and without (solid line) the snorkel. The coal was off while spectra were collected in both cases.

The spectral emittance calculated with the snorkel does not match that found without the snorkel. The emittance tends to level off at higher wavenumbers with the snorkel in place. This same trend is seen in the emittances found under reducing conditions. This raises the question: are the spectral emittance measurements found under reducing conditions significantly affected by the experimental methods used? In section 6.4, the presence of the snorkel was shown to have a negligible effect on the signal when looking only at the cleaned, painted probe.

In order to assess the influence of leaving the coal on when spectra are collected, an experiment was performed in which two spectra were collected sequentially: one with the coal on and the next with the coal off. Typical results are shown in Figure 8-2.

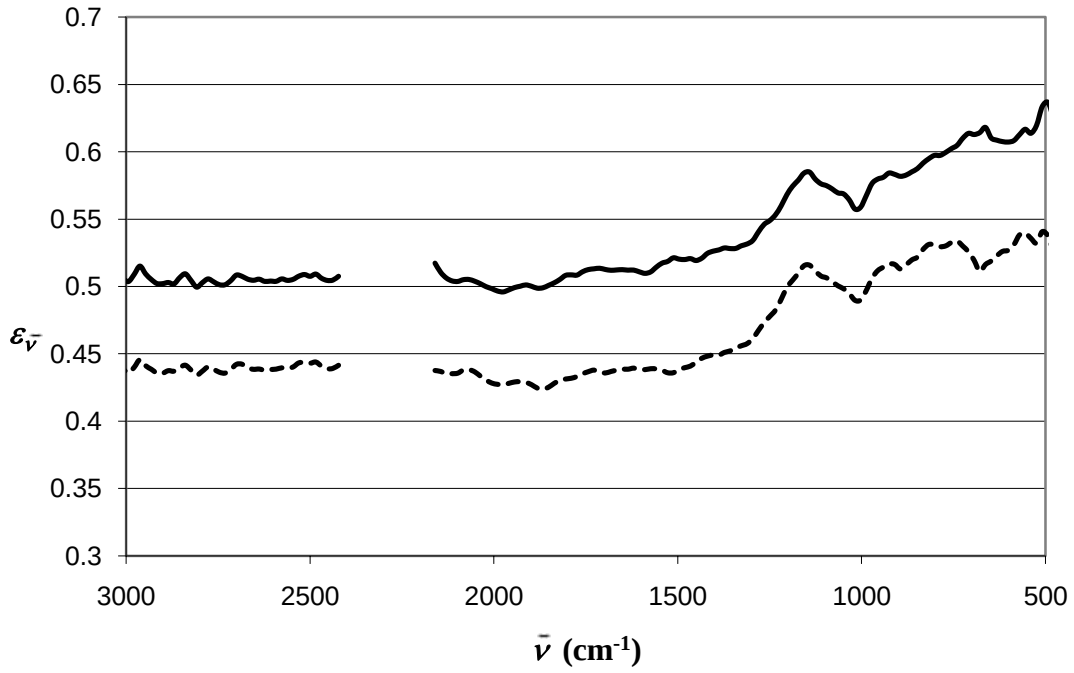

Figure 8-2. Comparison of the spectral emittance of the ash covered probe with (solid line) and without (dashed line) the coal on. The snorkel was used in both cases.

From Figure 8-2, it is clear that leaving the coal on when a spectrum is collected results in a higher emittance because, despite the use of the snorkel, there is still a small cloud of particles in front of the probe which emits radiation. The combustion gases are also present in front of the probe, resulting in large emission bands. However, the difference in spectral emittance is essentially constant. There is no spectral variation that might explain the difference between the spectral emittances shown in Figure 8-1. There is not enough information to definitively account for the difference in spectral emittance in Figure 8-1. Possible explanations for the disparity include the non-uniform flow of the combustion gases and the changing of the flow around the probe due to the presence of the snorkel and the nitrogen purge. More investigation is required to determine the accuracy of the reducing deposit measurements.

8.3 Summary

This work consisted of two primary objectives: 1. the development of an experimental procedure used to make *in situ* measurements of the spectral emittance of coal ash deposits and 2. *in situ* experimental measurements of the spectral emittance of coal ash deposits for both bituminous and subbituminous coals under oxidizing and reducing conditions. The results of this work are important in the design and operation of boilers and gasifiers.

The experimental procedure consisted of collecting ash deposits on a cylindrical probe under controlled conditions. A number of instruments were used to analyze the ash deposits formed. A Fourier transform infrared (FTIR) spectrometer was used to measure the spectral emissive power from the ash deposit. The spectral emissive power, combined with an instrument response function, was used to calculate the deposit surface temperature and the spectral emittance of the deposit. This experimental method was validated by calculating the known temperature and spectral emittance of a blackbody radiator.

The experimental method was used to find the spectral emittance of bituminous and subbituminous coals under both oxidizing and reducing conditions. The bituminous coal examined was Illinois #6 coal from the Crown III mine. The subbituminous coal analyzed was Wyoming coal from the Corederro mine. The spectral emittances of both types of coal exhibited similar trends. The emittance of the subbituminous coal was lower than that of the bituminous coal. Under reducing conditions, the emittances of both coals followed the same trends as those seen under oxidizing conditions. Again, the emittance of the bituminous coal was greater than that of the subbituminous coal. The emittance of

both coals under reducing conditions was greater than those for oxidizing conditions. Some questions were raised about the accuracy of the measurements made under reducing conditions. The lack of control maintained during the reducing experiments resulted in uncertainties that could not be accounted for.

8.4 Future Work

Further investigation is required to determine the accuracy of the spectral emittance measurements made under reducing conditions and to account for the discrepancies found in this work when making measurements under reducing conditions. Analysis of more coals would provide more information about how the type of coal affects the emittance of ash deposits. Only loosely-bound particulate ash deposits with a nominal thickness of 1 mm were analyzed in this work. The emittance depends highly on the morphology of the ash deposit. Accordingly, analysis and experimentation of deposits of different size, structure, and morphology (i.e. sintered, particulate, and slag layers) would provide important information about the influence of deposit structure on emittance.

9 References

1. Smith, D. J., "IGCC Technology continues to Develop," *Power Engineering,* 107 (11), pp. 102-104 (2003).

2. Medha, J. M., Lee, S., "Integrated Gasification Combined Cycle – A Review of IGCC Technology," *Energy Sources,* 18 (5), pp. 537-568 (1996).

3. Kindred, B., "Coal: The Good and the Bad," *State Legislatures,* 33 (3), p. 14 (2007).

4. Turns, S. R., *An Introduction to Combustion*, 2nd ed. 2000, McGraw-Hill.

5. "EPA Finds Greenhouse Gases Pose Threat to Public Health, Welfare / Proposes Finding Comes in Response to 2007 Supreme Court Ruling," <http://yosemite.epa.gov/opa/admpress.nsf/0/0EF7DF675805295D8525759B00566924> (2009)

6. Hotchkiss, R., "Coal Gasification Technologies," *Proceedings of the Institution of Mechanical Engineers. Part A, Journal of Power and Energy,* 217 (A1), pp. 27-33 (2003).

7. Andrascek, R., Burns and McDonnell, "Comparing Emissions: PC, CFB, and IGCC," *Power Engineering,* 111 (3), pp. 60-65 (2007).

8. www.fossil.energy.gov, "How Coal Gasification Power Plants Work," (2007).

9. Smith, D. J., "IGCC: The 21st Century's Answer for the Clean Burning of Coal," *Power Engineering,* 104 (11), pp. 53-58 (2000).

10. Blankinship, S., "Gasification Technology Advancements Could Help Protect Western Coal Value," *Power Engineering,* 111 (6), pp. 3-4 (2007).

11. Moore, T. J. and Jones, M. R., "A Method of Measuring the Properties of Ash Deposits in a Coal Fired Reactor," *Proceedings of HT2007*, 2007 ASME-JSME Thermal Engineering Summer Heat Transfer Conference, HT2007-321699, July 8-12, 2007, Vancouver, British Columbia (2007).

12. Anderson, D.W., *Heat Transfer Through Coal Ash Deposits*. 1985, Purdue: West.

13. Wall, T.F., Bhattacharya, S.P., Zhang, D.K., Gupta, R.P. and He, X., *The Properties and Thermal Effects of Ash Deposits in Coal-Fired Furnaces.* Progress in Energy and Combustion Science, 1993. 19: p. 487-504.

14. Bockelie, M.J., Denison, M.K., Chen, Z., Linjewile, T., Senior, C.L., and Sarofim, A.F., *CFD Modeling for Entrained Flow Gasifiers*, in *Gasification Technologies Conference*. 2002: San Francisco, CA.

15. Robinson, A.L., Buckley, S.G., Yang, N., and Baxter, L.L., *Experimental Measurements of the Thermal Conductivity of Ash Deposits: Part 1. Measurement Technique*. 2000, Sandia National Laboratories: Albuquerque, NM. p. 1-26.

16. Rezaei, H.R., Gupta, R.P., Bryant, G.W., Hart, J.T., Liu, G.S., Bailey, C.W., Wall, T.F., Miyamae, S., Makino, K., and Endo, Y., *Thermal Conductivity of Coal Ash and Slags and Models Used.* Fuel, 2000. 79: p. 1697-1710.

17. Modest, M.F., *Radiative Heat Transfer*, 2nd ed., Academic Press, (2003).

18. Markham, J. R., Solomon, P. R., and Best, P. E., "An FT-IR Based Instrument for Measuring Spectral Emittance of Material at High Temperature," *Review of Scientific Instruments*, 61 (12), pp. 3700-8 (1990).

19. Shaw, D. W. and Smouse, S. M., "An Instrument for *In Situ* Temperature and Emissivity Measurements (INSITE) on Boiler Ash Deposits," The Impact of Ash on Coal Fired Plants, Proceedings of the Engineering Foundation Conference, Williamson, J. and Wigley, F., eds., pp 539 – 551, Solihull, England, June 20 – 25, Taylor & Francis (1993).

20. Incropera, F. P. and DeWitt, D. P., *Fundamentals of Heat and Mass Transfer*, 5th ed, John Wiley and Sons, Inc. (2002).

21. Moghaddam, S., Lawler, J., McCaffrey, C., and Kim, J., "Heat Flux-Based Emissivity Measurement," *AIP Conference Proceedings*, 764 (1), pp. 32-37 (2005).

22. Woskov, P. P., and Sundaram, S. K., "Thermal Return Reflection Method for Resolving Emissivity and Temperature in Radiometric Measurements," *Journal of Applied Physics*, 92 (10), pp. 6302-10 (2002).

23. DeWitt, D. P. and Nutter, G. D., *Theory and Practice of Radiation Thermometry*, John Wiley and Sons, Inc. (1988).

24. Watson, K., "Two-Temperature Method for Measuring Emissivity," *Remote Sensing of Environment*, 42, pp. 117-121 (1992).

25. Svet, D. Y., "Determination of the Emissivity in the Course of Cooling and Heating Processes," *Doklady Physics*, 45 (6), pp. 281-283 (2000).

26. Wall, T. F., and Becker, H. B., "Total Absorptivities and Emissivities of Particulate Coal Ash from Spectral Band Emissivity Measurements," *Journal of Engineering for Gas Turbines and Power*, 106, pp. 771-776 (1984).

27. Baxter, L. L., Richards, G. H., Ottesen, D. K., and Harb, J. N., "*In Situ*, Real-Time Characterization of Coal Ash Deposits Using Fourier Transform Infrared Emission Spectroscopy," *Energy and Fuels*, **7**, pp. 755-760 (1993).

28. Cundick, D. P., *Characterization of the Thermal Transport through a Temporally Varying Ash Layer*, Brigham Young University (2008).

29. Giffiths, P. R., de Haseth, J. A., Fourier Transform Infrared Spectrometry, 2nd ed., John Wiley and Sons, Inc., (2007).

30. Wiebelt, J. A., *Engineering Radiation Heat Transfer*, Holt, Rinehart, and Winston, Inc. (1966).

31. Energy Information Administration. <http://www.eia.doe.gov/glossary/glossary_b.htm> (2009).

Appendix A. Supplementary Tables

Table A-1. Fuel Analysis for the WY Corederro Coal: Proximate Analysis (% Mass Fraction), as Received

Fuel (maf)	Corederro
	Untreated
C	71.45
H	6.02
N	1.1
S	0.17
O	21.26
Total	100
Ash % (mf)	7.12
Moist. % (ar)	13.64
HV, MJ/kg (maf)	29.89
SiO_2	28.7
Al_2O_3	15.5
Fe_2O_3	10.2
CaO	15.1
MgO	3.6
Na_2O	1.5
K_2O	0.8
TiO_2	1.2
MnO_2	NA
P_2O_5	1.2
SrO	NA
BaO	NA
SO_3	22
Total	100

Table A-2. Analysis for the IL #6 Crown III Coal (% Mass Fraction): Standard Laboratories
8451 River King Drive, Freeburg, IL 62243
Date Sampled: 6/27/2007
Lab # 2007-01454-001

Proximate (As Received)	Moisture	16	Mineral Analysis	SiO2	51.17
	Ash	8.52		Al203	17.33
	Volatile	35.16		Fe2O3	17.73
	Fixed Carbon	40.32		CaO	4.26
	BTU	10655		MgO	0.99
	Total Sulfur	3.33		Na2O	1.7
Proximate (Dry)	Ash	10.14		K2O	2.21
	Volatile	41.86		TiO2	0.83
	Fixed Carbon	48		MnO2	0.07
	BTU	12684		P2O5	0.25
	Total Sulfur	3.97		SrO	0.04
	MAF BTU	14115		BaO	0.04
				SO3	4.4
Ultimate (As Received)	Moisture	16		Undetermined	-1.38
	Carbon	57.95		Type of Ash	Bituminous
	Hydrogen	4.27		Silica Value	68.68
	Nitrogen	1.08		T250	2421
	Chlorine			Base/Acid	0.39
	Sulfur	3.33		lb Ash /mm BTU	
	Ash	8.52		lb SO2/mm BTU	6.25
	Oxygen (Diff.)	8.85		Fouling Index	0.66
Ultimate (Dry)	Carbon	68.99		Slagging Index	1.55
	Hydrogen	5.08			
	Nitrogen	1.29			
	Chlorine		Reducing Fusion Temp.	I.D.	1954
	Sulfur	3.97		H=W	2042
	Ash	10.14		H=1/2W	2143
	Oxygen (Diff.)	10.53		Fluid	2221
			Oxidizing Fusion Temp.	I.D.	2256
				H=W	2379
				H=1/2W	2433
				Fluid	2579
				Browning T250	2337
				B&W T250	2421